國立中山大學材料科學研究所

博士論文

多元鎂基非晶質金屬玻璃熱機性質與熱可塑功能性之研究

Study on the thermomechanical properties and workability of Mg-based bulk metallic glasses

研究生：張育誠 撰

指導教授：黃志青 博士

中華民國 九十七 年 七 月

Study on the thermomechanical properties and workability of Mg-based bulk metallic glasses

A dissertation presented in partial fulfillment of the requirements
for the degree of Doctor of Philosophy

by

Yu-Chen Chang

This work was conducted under the supervision of

Prof. **Chih-Ching Huang**

Institute of Materials Science and Engineering
National Sun Yat-Sen University

July, 2008

國立中山大學研究生學位論文審定書

本校材料科學研究所博士班

研究生張育誠（學號：D923060009）所提論文

多元鎂基金屬玻璃熱機性質與熱可塑功能性之研究

經本委員會審查並舉行口試，符合博士學位論文標準。

學位考試委員簽章：

高伯威　　潘正堂

陳明　　謝克昌

鄭憲清

指導教授　黃志青

系主任/所長　謝克昌

作者簡介及謝誌

本人張育誠生於民國67年9月14日，高雄市人，民國92年進入國立中山大學材料科學與工程研究所就讀，於96學年完成博士學位。求學期間品學兼優，個性樂觀開朗，為人圓滑處事合宜，和朋友同儕相敬如賓，與師長成為忘年之交，亦師亦友互增所長，對於未來更充滿信心與幹勁，期待更多元挑戰。

本論文之研究及撰寫，特蒙恩師黃教授志青循循善誘、誨人不倦及去惑解疑，學生誠摯感恩，對於恩師之研究精神與為人風範，深表敬佩景仰，令我如沐春風、芝蘭之化，望與恩師日浹往來，增益學生所不能。承蒙義守大學鄭教授憲清古道熱腸、鼎力相助，令本研究更添色彩。且蒙跨海相助之杜博士興蒿，令我研究更加繽紛多元、精益求精。

感謝所上諸位師長們指點提攜，更衷心地感謝所上高伯威教授、謝克昌教授、陳明教授、機械與機電工程學系潘正堂教授與義守大學材料科學與工程學系鄭憲清教授不辭辛勞擔任口試委員，惠予指導，並對於本論文提出卓越見解與指正。

此外，感謝國科會經費支持，並蒙中山大學電子顯微鏡技術員陳貴香與王良珠小姐、中山大學奈米中心技術員顏采蓉小姐及顏仲崑先生辛勞協助樣品測試；義守大學材料科學與工程學系鄭憲清教授與其學生們與博精儀器股份有限公司之原料及測試儀器資料方面提供，除深表感謝外，誠心祝福順心如意。深受黃谷正教官照顧與幫忙，令本人可專心論文研究，特此感謝。所辦朱惠敏、顏秀芳和陳秀玉小姐於行政公事與日常生活上之挺立拔刀相助，深表恩謝。華應麒大哥的社會大學與處事態度更令小弟我受益豐碩，一日大哥終身大哥，大哥之名永銘於心。

研究期間，承蒙學長高立衡教授教誨良殷、樂育英才，令我學以致用志向得展，感恩言謝之心沒齒難忘。鄭舜宇博士耿直率性之個性與精益求精之求學精神令人佩服，小弟求學期間深受呵護照顧，真是感激不盡。博士班學長姐胡義群教授、鄭國光博士、洪英博博士、吳玉娟博士、楊凱琳博士和蔣偉仁博士之熱心教導指教，令我事半功倍百尺竿頭。

同時感謝張量然博士、丁仕旋博士、黃惠君博士和呂旻憲博士等研究所博士班同儕好友們的支持、鼓勵及協助，令我不顯孤單寂寞。尤其無話不談的同儕知己曾婉如博士是我精神心靈的良師、休憩娛樂的伙伴，令我抒解求學時的壓力與心靈上的困境，更加讓我易於融入中山材料所的群體裡；互通心靈的同儕知己謝心心博士，妳的深切關懷、恩情鼓舞，令本人通過考驗、克服難關，完成學業，沒有妳的伴陪，更沒有此時此刻的我；好友李敬仁博士則令我瞭解當研究工作者該具備的能力與責任，並鼓勵我面對挑戰與困難，突破瓶頸與阻礙，其專注研究工作之態度更可作為研究生典範，值得好好效法；好友洪子翔博士賦予我新的研究生命，令我研究之心死灰復燃，其懇切耐心之指導、謹慎嚴謹之態度，令我獲益良多，並帶領著我朝向成功的彼端；好友羅友杰博士直言不諱、擇善固執的個性，令本人敬佩不已，並將其視為一面明鏡，來檢討改正自身缺失；好友張志溢博士的刻苦耐勞與堅毅不覺也令在下稱服，作為學習效法之範。此外，研究室陳海明、賴炎暉、鄭宇庭、周鴻昇、裴浩然、劉名哲及郭哲男等博士班學弟們勤勉不倦、不眠不休用心向學，還常抽空幫忙在下，令人銘感於心。對於湯振緯、宋大豪及孫碩陽學弟們努力不懈、實事求是之學習態度與熱誠幫助之行為，也令我感動不已，在此致以深情感謝，並祝各位盡其所長、鴻圖大展。除研究所同儕好友外，吳善業(Gohan)、劉郡怡、程心慧(Mor)、林瑾瑜、王學樑、王肇霖、陳里芳、郭逢祥、沈銘原及張依寰等知己莫逆相伴鼓舞，使我於研究時不感孤苦無依，更讓我的研究所生涯多采多姿，比他人更增添色彩，謹呈萬分謝意。

我將最崇高之感謝之意呈獻給家父母－張習遠先生與謝小燕女士賢伉儷，感謝多年來栽培及支持，與關心愛護之恩情，無以為報，僅能將此論文獻於您們，這是屬於您們的榮耀。蒙乾爹娘－周正義先生與季惠琴女士賢伉儷，您們的鼓勵與關懷，給予我莫大前進的力量，讓我於成長階段勇於挑戰及創造，開創美好將來，感謝之意溢於言表。此外，大舅謝達華教授的恂恂善誘、諄諄教誨，於百忙之中還不忘提攜照顧，令外甥我於枷鎖中逃脫、低潮中走出，感激之心銘心鏤骨。再者，感謝張、謝氏歷代祖先、外公婆、姊張藝馨、乾哥(嫂)－周徹夫婦、哥張

志豪、妹楊佳蓉、弟謝明勳，以及乾妹周黛珊(Vivian)等親戚之伴陪，讓我於求學過程不顯枯燥乏味，你們的讚許鼓舞也增強了我的信心與求學研究之興趣。

最後，感謝一路走來始終伴陪於身的戴元君小姐，妳在我身後支持我的那雙手，協助著我邁向彼此共創的美妙未來，妳的疼惜關愛令我哀傷時得到安慰、生氣時獲得抒解、挫折時賦予我再度站起奮發向前的勇氣，甚至於痛苦時，妳那無人比擬的笑顏，更有著令我心曠神怡忘卻痛苦的魔力，妳永恆不變的支持與鼓勵，才令本論文可順利撰寫完成，妳可謂此論文之親生母親。

在此以最感恩的心感謝所有關心我、關懷我、給予我幫助的人，相逢即是有緣，結識各位也令在下於人生路上不虛此行，感謝各位於我求學研究階段之勉勵激勵，令本人可以順利完成這本研究論文，在此以「天下無不散之宴席」及「結束即是開始」來與各位長輩、師長、學長姐、同學、學弟妹及所有知己好友道聲珍重再見，期待重逢！

張育誠 謹誌

歲次戊子年暑　于中山西灣

Table of Content

List of Tables

List of Figures

中文摘要

近年來，非晶質合金之未來潛力與實質工業應用開始被多加關注，尤其微機電系統(MEMS)零組件與光電壓印材料方面，更是投注大量的人才來研發。本論文主要以具低玻璃轉位溫度(T_g)之輕量型鎂基非質晶合金，作為新一代的壓印材料之研究。且利用熱機性分析儀(Thermomechanical analyzer)來獲得鎂基非晶質合金之粘度行為與熱機性參數，並進而探討其二次加工性，提出加工溫度區間、耐熱程度等實用之數據，作為日後工業應用之有利資訊。

輕量型鎂基非晶質合金具良好之玻璃形成能力(Glass forming ability)，根據鎂基非晶質合金之發展歷程，與熱分析所得之結果，顯示鎂-銅-釔(Mg-Cu-Y)與鎂-銅-釓(Mg-Cu-Gd)之金屬成分是易於製成塊狀鎂基非晶質金屬玻璃(Bulk metallic glass)。本文先以鎂-銅-釔作主軸，藉由熱分析與硬度結果作為依據，獲取最適合之塊狀非晶質合金成分($Mg_{58}Cu_{31}Y_{11}$)作為熱壓印材料樣本。樣本經由熱壓印機施予適當應力與時間之下，以幾近完美地形成六角鏡模具，且成功轉印於聚甲基丙烯酸甲酯(Polymethylmethacrylate)之上。有限元素分析法(Finite element simulation)之結果，也與熱機性分析、壓印試片相互印證。

此外，鎂-銅-釓之金屬成分更較鎂-銅-釔具良好玻璃形成能力，據相關文獻所言，若以少量銀(Silver)或硼(Boron)元素取代成分鎂-銅-釓(釔)中的銅(Copper)元素原子成分比，將可提升熱穩定性或機械性質，更增加金屬玻璃塊材形成大小，以便加強材料使用性。本論文也探討鎂-銅-(銀，硼)-釓多元鎂基合金之熱機械性質、粘滯流動行為和形變能力等加工性，並利用形變模型來深入探討其內部結構與能量關係之影響。由研究發現，添加銀或硼元素，雖增加塊狀大小、機械性質或熱穩定性，但卻提高粘滯流動困難性、增加活化所需能量、降低形變能力等負面加工性因子，侷限二次形變能力。但銀、硼取代銅元素之玻璃金屬材料確實顯示出較佳之機械性質和室溫下之硬度。由此可知，材料應用性不應只單探討材料之形變能力、熱性質或機械性質，而是需全方面考量其應用所需。

最後，本論文提出數個指數如粘滯性(Viscosity)、VFT 溫度(Vogel-Fulcher-Tammann temperature)、應力下之熱穩定性、形變性(Deformability)等，以量化數據方式，來得知材料之加工性質，作為塊狀玻璃金屬加工性之參考，以便用於未來應用發展之依據。

Abstract

In the near couple years, the applications of amorphous alloys have attracted great attention due to their characteristics and future potential. This research is intended to synthesis a lighter Mg-based amorphous alloy as the imprinting materials for micro-electromechanical system (MEMS) with a high glass forming ability (GFA) and lower glass transition temperature (T_g). Also, the workability of the Mg-based metallic glasses is examined in terms of several viscous flow behaviors and parameters obtained from the thermomechanical analysis (TMA).

The lighter Mg-based metallic glasses exhibit their superior glass forming ability, and can be cast into bulk metallic glasses (BMGs). Based on the thermal analysis of the Mg-Cu-Y glassy materials, the evaluation of the glass forming ability and thermal stability for searching the optimum alloy composition is conducted. By using $Mg_{58}Cu_{31}Y_{11}$ amorphous alloy with the best composition as the micro-forming specimens, imprinting was made by hot pressing at 150^{o}C with several applied compressive stresses to form the hexagonal micro-lens arrays. Finite element simulation using 3D Deform software is also applied to trace the microforming evolution, and to compare with the experimental observations. The results demonstrate that the imprinting is feasible and promising.

On the other hand, the Mg-Cu-Gd BMGs with even better GFA than Mg-Cu-Y are explored in terms of their thermomechanical properties. Extension of this study is performed partially by Cu replacing by Ag or B for the improvement of maximum diameter and thermal stability. And the workability of these Mg-Cu-(Ag, B)-Gd metallic glasses, namely, $Mg_{65}Cu_{25-x}Ag_xGd_{10}$ (x = 0, 3, 10 at %) and $Mg_{65}Cu_{22}B_3Gd_{10}$ is evaluated in terming of the thermomechanical parameters, viscous flow behavior, deformability, and the deformation model. It is found the fragility for viscous

deformation would increase with the replacement of Ag or B, leading to the negative factors for the micro-forming and nano-imprinting practices. This conclusion is supported by the many extracted parameters.

Thus, even the B-additive Mg based BMG has much higher hardness and Ag-additive Mg based BMG has the larger maximum rod diameter, they are more difficult to be formed, appearing as a negative factor in the micro-forming or nano-imprinting industry. The base $Mg_{65}Cu_{25}Gd_{10}$ alloy stilly appears to be more promising than the Ag or B-containing alloys when the viscous forming is under consideration.

Chapter 1 Introduction

1.1 Glass

Glass, in the traditionally correct conception, is a liquid that has lost its capability of flow. In some cases, the glassy structure is hardly identifiably from the fluid substance before it becomes the glass [1].

Why do these special materials or solutions abruptly occur the dramatic “slowing down” in the diffusive motions of its particles?

At some exactly freezing temperatures, these substances do not form precisely ordered crystalline materials like so many other normal matters, why?

These questions are brought forward by physicists as well as materials scientists. In 1995, Angell’s paper [1] was published to give an overview of many approbatory views and to highlight some of the efforts to answer these questions. The answers of these questions affect on a wide range of studies.

It is known that glass occurs naturally as the volcanic glass, and a recent idea is also shown that most of the universe water exists in the glassy state like water in comets (formed by condensation from the gaseous state at very low temperatures). And the most polymers in common uses are non- or semi-crystalline solids, but these rubbers become splintered like dropped goblet when impacted at the liquid nitrogen temperature.

The instance of the naturally occurring glassy water in comets demonstrates that glasses are not necessarily formed by the cooling of a liquid state. In face, the glassy state can be obtained by many different methods and behave as the same materials fundamentally. Vitreous silica, the typical glass material, can also be obtained by many ways, for instance, the cooling of liquid silica, vapor condensation, heavy particle bombardment of a crystalline form, chemical reaction of organosilicon compounds followed drying, and vapor-phase reaction of gaseous molecules followed by condensation. In fact, only the latter route with the purified reactants produces the high purity glass sufficient for the requirements of the fiber optics communications technology. While the densities of the products prepared by the different processes may not be identical without an annealing process, they can still be differentiated by the characteristics of their X-ray diffraction patterns. The various methods for preparing glasses are summarized in Figure 1.1 [2].

For many matters and mixtures, there are non-crystalline (amorphous) structures for the atoms and molecules with constitutionally low energy, and these particles can easily congregate. These may not be the lowest energy packing modes, because the exothermic reaction occurs during crystallization.

During the cooling state at normal rate, for the good glassy formers, the probability to nucleate a crystal rather than to form of the glassy solid is low. In the case of liquid B_2O_3 (ingredient of Pyrex glass) at an ambient pressure, the crystals will not grow even when the B_2O_3 melt is seeded with a crystallite of the stable phase, because of the small driving force and the slow kinetics. Crystallization in this case is only induced by raising the pressure [3]. In some binary solutions at low temperatures, the glassy state can be as thermodynamically stable as crystals or crystal plus solution (coagel) [4].

The most thoroughly studied method to form a glassy state is still the cooling of a liquid with diffusion slowdown. This method has been applied to many glass-forming systems, including proteins, biopolymers and metallic glasses [1, 5, 6].

1.2 Metallic glasses

Metallic glasses, in the substantial definition, are the metallic materials without the periodicity of crystal, and with a disordered atomic-scale structure. In contrast with other crystalline metals, with a highly ordered arrangement of atoms and long range order, these metallic glass alloys are non-crystalline. However, the atomic dispersion in metallic glasses may be incompletely random, and retains a greater degree of short range order than that in the liquid, and both lack of the long-range order arrangement, as shown in Figure 1.2. As a result, the metallic glasses have been called as liquid metals due to this kind of liquid-like atomic arrangement, and these liquid metals have also been called as non-crystalline metals, amorphous metals, and glassy metals. Metallic glasses are usually less brittle than oxide glasses, however, these amorphous metals are glasses without the transparency, and look like opaque shiny and smooth metals, as shown in Figure 1.3 [7].

The amorphous alloys show several special properties as compared with the corresponding crystalline alloys, including (a) lower Young's modulus and higher tensile strength, (b) larger elastic elongation about 2%, (c) larger elastic energy up to yielding, (d) indistinct plastic elongation due to inhomogeneous deformation mode, (e) relatively greater impact fracture energy, (f) better anti-oxidation/corrosion behaviors, (g) excellent electromagnetic properties, and (h) easy shaping or forming ability [8]. The unique properties and application fields of amorphous alloys are summarized in Table 1.1 [9].

1.2.1 Evolution of metallic glasses

In 1960, Klement et al. first discovered the amorphous or metallic glassy phase [6]. The splat quenching method (Figure 1.4) was used to solidify an $Au_{75}Si_{25}$ liquid into a supercooled state with cooling rates between 10^6 to 10^{10} K/s. Then, the first major breakthrough in metallic glass formation came in 1960 when Duwez and co-workers discovered that liquid $Au_{80}Si_{20}$ [6] could be turned into an amorphous solid by direct quenching from the melt with a cooling rate of 10^6 K/sec. In these trailblazers' literature, they have made a metallic glass ribbon with a thickness of 1~10 μm. After couple years, the ternary metallic glasses of Au-Si-Ge and Pd-Si-M (M=Ag, Cu or Au) were produced by Chen and Turnbull [10, 11].

In 1970, Chen and Miller [12] used two rollers quenching process (Figure 1.5) to synthesize a 2 mm wide and 50 μm thick metallic glass ribbon with several meters long. This was the first time to produce the longer length scales of metallic glasses, so the continuous liquid quenching process became the primary way to make the metallic glass ribbons. During 1970s, amorphous alloys were regarded as the new classes of soft magnetic alloys [13, 14]. Hence, using the metallic glass core in transformers became the ground rule. Regrettably, the commerciality of metallic glasses also terminated here. In the late 1980s, many new "engineering" properties of metallic glasses were discovered, leading to a revival of interest in the amorphous alloys. In Inoue's group, the precursors have found the new multi-component systems metallic glasses consisting mainly of common metallic elements with lower critical cooling rates [9], and they have also made many valuable works on fracture characteristics, crystallization behavior and stabilization phenomena of metallic glasses.

The first bulk metallic glass (BMG) was reported by Drehman and Greer [15]; and Kui et al. [16] by quenching ternary Pd-Ni-P alloy in 1984. Heterogeneous nucleation sites on the surface were dissolved, by repeated melting in a boron oxide flux. As a result, glass formation at cooling rates below 10 K/s and glassy ingots with sizes up to 10 mm in diameter were synthesized. Today, the bulk metallic glass (BMG) is defined in the community as a metallic glass sample with its smallest dimension at least 1 mm thick. Hence, the size of metallic glasses is also mentioned initiatorily on the following literatures. In 1991, Inoue et al. cast the $La_{55}Al_{25}Ni_{10}Cu_{10}$ fully glassy alloy with a 9 mm thick by using cooling Cu molds [17]. Next year, the Mg-Cu-Y BMGs with a diameter of 7 mm were also progressed [18]. After these BMGs are discovered, the same group reported a family of Zr-Al-Ni-Cu based metallic glassy alloys with a high glass forming ability (GFA), and the $Zr_{65}Al_{7.5}Ni_{10}Cu_{17.5}$ amorphous alloy is seized of the largest thickness (~ 15 mm) among this family [19]. On the same year, Peker and Johnson discovered an exceptionally good glass forming system; Zr-Ti-Cu-Ni-Be. In particular $Zr_{41.2}Ti_{13.8}Cu_{12.5}Ni_{10}Be_{22.5}$, which is commercially known as Vitreloy1^{TM} (Vit 1), exhibits a critical cooling rate of 1 K/s and can be cast up to several centimeters in diameter [20]. However, the presence of toxic beryllium in this alloy limits its use. Johnson and co-workers further have developed another group of easily processible BMGs Zr-Ti(Nb)-Cu-Ni-Al alloy in 1997, namely, $Zr_{52.5}Ti_5Cu_{17.9}Ni_{14.6}Al_{10}$ and $Zr_{57}Cu_{15.4}Ni_{12.6}Al_{10}Nb_5$ [21]. Even though their critical cooling rate is higher than Vitreloy1^{TM}, they still have good mechanical properties and do not contain beryllium.

Other important credits include that Inoue et al. have re-investigated the first discovery of $Pd_{40}Ni_{40}P_{20}$ BMG, and they discovered the Pd-Ni-P BMG can increase the critical thickness from 5 mm to 72 mm when 30% of nickel replaced by copper [22]. Also, Ma et al. [23] developed the Mg-based BMG with inch-diameter successfully in 2005, bringing on a momentous progress on Mg-based BMG application. Table 1.2 [24] is the list of the familiar amorphous alloys and BMG systems, and Figure 1.6 shows the relationship of critical thickness with the date of discovery [25].

1.2.2 Manufacture methods of metallic glasses

Although metallic glasses are thermodynamically metastable, there are many processing routes, in which they can be processed. We can use gases (vapor deposition), liquids, or even crystals (solid state amorphization) as the starting material.

From different cooling rates, these methods can be classified into the following three types: (1) cooling the gaseous state to the solid state, (2) cooling the liquid state to the solid state, and (3) transforming the solid state to another solid state.

Cooling the gaseous state to the solid state

The amorphous alloys can be produced by depositing the gaseous alloys or metal elements onto a cool substrate with a higher cooling rate of 10^{10} - 10^{12} K/s. The sputtering [26] and vacuum evaporation [26], shown in the Figure 1.7 [27], are two kinds of processes that belong to this method.

For the sputtering process, a high voltage is applied on two electrodes to create an electronic filed under a gas (nitrogen or argon) environment. Then the electrons are emitted from the cathode and accelerated in the electronic filed. These electrons will excite the gas molecules into positive gas ions and electrons. Once the gas ions impact an alloy or metal target, the alloy or metal atoms will deposit on the substrate and form an amorphous film. On the other hand, the vacuum evaporation process is necessary to use a heating and vacuum system. The alloy or element vapors which are emitted from the heating target are also deposited on the substrate to form the amorphous film.

Although this method has the fastest cooling rate, there are still some disadvantages. The high vacuum equipments are expensive, and the size of amorphous samples is too small to make useful applications in bulk form. Recent studies [28] suggest that the thick film amorphous layer (around 100 μm to 1 mm) on the substrate can improve the substrate material hardness and toughness. This will promote the casting applications of sputtering for making amorphous surface films.

Cooling the liquid state to the solid state

Quenching liquid with a cooling rate of 10^3 - 10^8 K/s is used extensively in fabricating the amorphous alloys, and the amorphous alloys can be made into all kinds of forms by using this method, including the splat quenching, twin roll quenching, melt spinning, planar flow casting, metallic mold casting, high-pressure die casting and spray forming, etc [29-31]. The first step in this method is to melt or to atomize the alloys, and then quench them onto a low temperature mold or substrate with high thermal conductivity.

The first amorphous metal Au-Si was prepared by this method (gun quenching) [32]. In this process, the molten sample is held in a non-reactive crucible with a small hole at the bottom, and small droplets are driven out of the hole by a shock wave. The droplets then impinge onto a highly conductive metal substrate such as copper, spread out and form a film. Although this method provides the highest cooling rate of about 10^6 - 10^8 K/sec, the irregularity of the foil thickness makes the sample to be a mixture of amorphous and crystalline structure. The average thickness of the film formed by this method ranges from 5 to 25 μm.

Another method to obtain foils of thickness ranging from 20 to 50 μm is the hammer-anvil method [33]. In this process, two metallic pistons are propelled towards each other at high speeds, and a molten drop of alloy is quenched into a foil between the two metallic pistons. This process also provides high cooling rates.

A major advancement in processing came with the development of twin roll technique. This technique was potentially the first continuous process to produce metallic glasses. The thin ribbons of metallic glasses are obtained when a molten metal is fed into the nip of two rapidly rotating wheels. However, in this process, it is difficult to keep the liquid from either solidifying too early (before the minimum separation between the wheels occurs) resulting in cold worked strips, or solidifying too late (i.e. leaving the nip partially liquid).

To date, the most accepted continuous processing technique of making metallic glass ribbons is melt spinning. In this technique a stream of molten metal is directed at a rapidly rotating copper wheel. This process provides high cooling rates, and the ribbons with the thickness ranging between 20 and 100 μm can be produced [34].

The most widely used technique to process (the novel) bulk metallic glasses both in industry and research is casting. This is a relatively simple technique, in which the molten material is poured into the mold with a desired pattern. It is only used for processing bulk metallic glasses due to the limited cooling rates. This technique has been widely employed at the many university laboratories and in the industry such as Liquid Metal Technologies for the mass production of parts.

Transforming the solid state into another solid state

When using this method, the cooling rate is not necessarily critical, and the processes include severe plastic deformation, the solid-state reaction, particle bombardment, and solid-state inter diffusion, etc.

The principle of severe plastic deformation is to refine the grain size of the alloy by creating a large amount of plastic deformation. When the grain size is small enough, the structure of the crystalline alloy is transformed into the amorphous state. There are many ways to achive a large amount of plastic deformation , such as cyclic extrusion or cyclic compression, torsion straining under high pressure, equal channel angular pressing (ECAP), mechanical alloying (MA), and accumulative roll bonding (ARB) [35-40].

When high-energy electrons or heavy ions such as N^+ impact an alloy surface, the atoms of alloy surface might rearrange to form the amorphous state. This is the basic concept of the particle bombardment method. Various processes used for this method include neutron and ion particle bombardment irradiation, electron beam radiation, ion implantation, and ion beam mixing.

Finally, the solid-state interdiffusion reaction method is different from the two methods mentioned above. As two different metal layers or thin films are treated with an appropriate heat treatment process, the atoms between two metal layers will diffuse to each other and make an amorphous layer, provided that the temperature is not high enough to induce any intermetallic compound.

1.2.3 Factors of the glass forming ability (GFA)

The high GFA of cast amorphous alloys means a larger size of an amorphous alloy can be fabricated easily under a lower cooling rate. Meanwhile, many researches have noticed that the GFA is affiliated with the thermal properties [41-45], atomic sizes [46-51], compositions [52-56] and electronic configurations [57-62] of the amorphous alloy. Hence, some parameters are proposed to estimate the GFA and to design the metallic glass systems.

Among these parameters, the thermal properties are applied extensively due to two advantages. One is that the thermal information of amorphous alloy is unique and can be obtained easily and quickly. Another advantage is that these data can be transformed to an index by simple calculation.

Supercooled liquid region (ΔT_x)

For estimating GFA of metallic glasses, the first famous index is the supercooled liquid temperature region (ΔT_x). In accordance with the DSC trace of a metallic glass in a heating process, there are two reactions before the metal is molten, as shown in Figure 1.8 [63]. One reaction is the glass transition reaction with an endothermic phenomenon, and the other is the crystallization reaction with an exothermic phenomenon. Accordingly, the supercooled liquid region is defined by the difference between glass transition temperature, T_g, and crystallization temperature, T_x. And it can be described as

$$\Delta T_x = T_x - T_g \ . \tag{1-1}$$

This temperature region not only shows the thermal stability of amorphous alloy, but also exhibits the GFA of metallic glasses. The relationship of critical cooling rate (R_c) and supercooled liquid region (ΔT_x) is shown in Figure 1.9 [64].

Reduced glass transition temperature (T_{rg})

Another factor predicted by Turnbull [45] in improving the glass-forming ability is the reduced glass transition temperature, $T_{rg}' = T_g/T_m$ or $T_{rg} = T_g/T_l$, and it is an important factor to determine the critical cooling rate in the supercooled liquid among these factors.

A larger T_{rg} value would lead to a lower critical cooling rate, and a better GFA. This correspondence is shown in Figure 1.10 [64]. However, Lu et al. [65] had reported that the $T_{rg} = T_g/T_l$ is better than $T_{rg}' = T_g/T_m$ for estimating the GFA of amorphous alloys. For most alloys, the glass transition temperature is influenced slightly by the change of alloy compositions; however, the liquidus temperature changes distinctly with the change of alloy compositions. So the T_{rg} exhibits a strong dependence in alloy compositions.

Gama value, γ

T_{rg} and ΔT_x both are usually employed to evaluate the GFA, but unfortunately some metallic glass systems cannot be satisfactorily predicted the degree of vitrifaction synchronously by using these two indexes. In some situations, the ΔT_x index is better than the T_{rg} index to judge the GFA [66-68]. Whereas, the T_{rg} index is more suitable than the ΔT_x index in some other amorphous alloys [65, 69, 70]. Thus, a new index γ was proposed by Lu and Liu [71], and the definition of γ value is shown in Fig. 1.11 [72].

There are two targets for achieving a better GFA amorphous alloy. One is the stabilization of liquid phase, and the other is the resistance of crystallization. If an alloy reveals a lower T_l, the melting liquid phase of this alloy will be maintained to a low temperature under a cooling step. Then, if an alloy shows a lower T_g, it means that the metastable glass phase is more stable at low temperatures. The both cases suggest that the liquid phase is more stable. On the other hand, while the alloy has a higher T_x, it indicates that the starting crystallization of the glass phase proceeds at a higher temperature upon heating. Accordingly, the three kinds of phase transformation temperatures are combinatorial on the γ value which can be expressed as

$$\gamma = \frac{T_x}{T_g + T_l}. \qquad (1\text{-}2)$$

The critical cooling rate (R_c) and the critical thickness (Z_c) of amorphous alloys can be plotted against the γ value as shown in Figure 1.12 [71], and can be expressed by the following two equations,

$$R_c = 5.1 \times 10^{21} \exp(-117.19\gamma), \tag{1-3}$$

and

$$Z_c = 2.8 \times 10^{-7} \exp(41.7\gamma). \tag{1-4}$$

In addition, the comparison of ΔT_x, T_{rg}, γ, R_c and Z_c is summarized in Table 1.3 [71].

Gama-m value, γ_m

The above mentioned Gama value is based on two major circumstances: the resistance of crystallization and stabilization of liquid phase [71-73]. According to this idea, in our group Du et al. [74] brought forward a new GFA index, γ_m.

In the stabilization for the liquid phase of an amorphous alloy, the concept of lower T_l is similar to the γ value. Thus, the GFA should be inversely proportional to the liquidus temperature. In other words, GFA is proportional to $1/T_l$. Other than the γ value index considering the transition temperature, the γ_m value index deliberates the supercooled liquid region.

The amorphous alloy with a larger ΔT_x usually reflects a greater stability and a better glass-forming ability (GFA). As a result, the GFA should be proportional to (T_x-T_g). The factor for rhe stabilization of a liquid phase is summarized as

$$\mathrm{GFA} \propto \frac{\Delta T_x}{T_l} = \frac{T_x - T_g}{T_l}. \tag{1-5}$$

Now deliberating the resistance of crystallization, the higher crystallization temperature suggests a higher crystallization resistance. By normalizing this T_x by T_l in order to make for a dimensionless parameter, it suggests that GFA is directly recited to T_x/T_l. Coupled the above two considerations, the GFA index of γ_m is established as [74]

$$\gamma_m = \frac{T_x - T_g}{T_l} + \frac{T_x}{T_l} = \frac{2T_x - T_g}{T_l}\,. \qquad (1\text{-}6)$$

The critical cooling rate of amorphous alloy shows the linear dependence with the γ_m value, as shown in Figure 1.13, and the R_c is calculated as [74]

$$\log R_c = 14.99 - 19.441\gamma_m\,. \qquad (1\text{-}7)$$

1.2.4 Bulk metallic glasses

Since late twentieth century, the great deals of bulk metallic glass systems have been reported. Commonly, these systems of bulk metallic glasses could be divided into two main types: ferrous and nonferrous group metals, as shown in Table 1.4 [24]. The ferrous systems include the Fe-(Al, Ga)-metalloid (P, C, B, Si, Ge), (Fe, Co, Ni)-(Zr, Hf, Nb)-B, Fe-Co-Ln-B, and Ni-Nb-(Cr, Mo)-(P,B) alloys, and the nonferrous alloy systems include the Mg-Ln-M (Ln is the lanthanide atoms, and M is Ni, Cu or Zn metallic atoms), Ln-Al-TM (TM is the VI~VIII group transition metal atoms), Ln-Ga-TM, Zr-Al-TM, Zr-Ti-Al-TM, Ti-Zr-TM, Zr-Ti-TM-Be, Zr-(Nb,Pd)-Al-TM, Pd-Cu-Ni-P, Pd-Ni-Fe-P, Pd-Cu-B-Si, and Ti-Ni-Cu-Sn systems.

The ferrous alloy systems are researched after the synthesis of the nonferrous alloy systems. The alloy components are sorted out into five species, as summarized in

Table 1.4 [24]. The first group is consisted of ETM (or Ln), Al and LTM as exemplified by the for Zr-Al-Ni and Ln-Al-Ni systems, where ETM is IVB~VIB group transition metals and LTM is VIIB~VIIIB group transition metals. The second group is composed of LTM, ETM and metalloid such as the Fe-Zr-B and Co-Nb-B systems. The third group is the LTM Fe-(Al,Ga)-metalloid systems, and the fourth group is indicated by Mg-Ln-LTM and ETM (Zr,Ti)-Be-LTM systems. The fifth system, such as the Pd-Cu-Ni-P and Pd-Ni-P systems, are composed of only two kinds of group element (LTM and metalloid) different from the combination of the three types of group elements for the four previous groups. Note that the bulk metallic glasses are developed from many important engineering alloys, such as the Fe, Co, Ni, Ti, Cu, Zr and Mg based amorphous alloys. Over the years, the bulk metallic glasses are researched by the investigators worldwide to increase the maximum diameter in the order of Pd-Cu > Zr > Mg (Ln) > Fe > Ni > Co (Ti) systems.

1.2.5 Characterizations of bulk metallic glasses

The bulk metallic glasses possess some various properties due to their unique structure, relative to the traditional crystalline alloys. The primary properties and application fields of these amorphous bulk metals are summarized in Table 1.1. Some more important properties are described below.

Mechanical properties

The superior mechanical properties of bulk metallic glasses are the most favorable characteristics for many applications. Since the atomic random arrangement configuration and dense packing structure, when the applied stress is on the amorphous alloys, the amorphous alloys only allow limited atomic displacements to resist deformation. Due to the absence of dislocation mechanisms for plastic deformation, the amorphous alloys are always high strength materials.

The bulk metallic glasses have unique mechanical properties which are different from those of the crystalline alloys, i.e., the bulk metallic glasses have higher tensile strength and lower Young's modulus. The difference can reach about three times [75]. The relation between tensile fracture strength (σ_f), Vickers hardness (H_v) and Young's modulus (E) for the various bulk metallic glasses is shown in Figure 1.14 [64], together with the data on the conventional crystalline alloys. The bulk metallic glasses have high σ_f of 840 - 2100 MPa combined with E of 47 - 102 GPa, depending on alloy compositions [64]. Thus, the bulk metallic glasses tend to exhibit higher σ_f, higher H_v and lower E than the corresponding crystalline alloys.

The three-point bending flexural stress and deflection curves of the Zr-Al-Ni-Cu and Zr-Ti-Al-Ni-Cu bulk amorphous alloys have been measured [76]. These bulk amorphous alloys have high bending flexural strength values of 3000 - 3900 MPa which are 2.0-2.5 times higher than those for crystalline Zr- and Ti-based alloys. Figure 1.15 summarizes the bending and rotating beam fatigue strength as a function of fatigue cycle up to failure for the bulk amorphous $Zr_{65}Al_{10}Ni_{10}Cu_{15}$ [77] and $Pd_{40}Cu_{30}Ni_{10}P_{20}$ [78] alloys, respectively, together with the data under tensile stress conditions for various melt spun amorphous ribbons. It is confirmed that these Zr- and Pd-Cu-based bulk metallic glasses have good combination of various mechanical properties, which could not be obtained from conventional crystalline alloys.

Magnetic properties

Applications of magnetic ferrous glasses are mainly based on their superior soft magnetic properties. Sensors for electronic article surveillance have become a large application of amorphous materials. Thin sheets of glassy materials were first produced by melt spinning and subsequent annealing, resulting in the formation of nanocrystals in a glassy matrix. These nanocomposites still sustain their soft magnetic properties, but have a higher saturation magnetization and lower magnetostriction than the purely amorphous base materials. The most famous example is the alloy with the tradename FINEMET [79], which is a Fe-rich Fe-Si-B alloy with a small addition of Cu and Nb. The use of thin sheets in high frequency applications is of advantage, since the eddy currents can be reduced.

Thin ribbons of magnetic nanocomposites and purely metallic glasses are currently used in transformer cores, in magnetic sensors, and for magnetic shielding. Although some magnetic bulk glasses have recently been discovered, so far none of these materials show promising applications. The difficulty in the development of magnetic bulk glasses results from the fact that ferromagnetic elements like Fe, Co, Ni, and Gd are prone to oxidation, which increases the probability for heterogeneous nucleation. It was shown that the nucleation rate in Fe–Ni–P–B (Metglass) alloys can be reduced by four orders of magnitude when heterogeneous nucleation is minimized by the use of fluxing techniques [80]. Commonly, the types of magnetic amorphous alloy systems could be divided into the two categories of TM-TM and TM-M (TM = Fe, Co, Ni, Zr, Hf, etc; M = B, C, Si, P, Ge, etc) systems.

Chemical properties

When bulk metallic glasses for their good static and dynamic mechanical properties are used as structural materials, it is essential for the bulk amorphous alloys to have good corrosion resistance in various kinds of corrosive solutions. Due to the homogeneous single phase structure, which is lack of grain boundaries and dislocations in crystals, the amorphous alloys have superior corrosion resistance. In addition, the corrosion resistance of amorphous alloy could be improved by adding some kinds of corrosive solute.

The corrosion resistance is remarkably improved by the dissolution of Nb or Ta. Asami and Inoue [81] have examined that the corrosion resistance of the melt-spun Zr-TM-Al-Ni-Cu (TM=Ti, Cr, Nb, Ta) alloys in HCl and NaCl solutions, and found that the Nb- and Ta-containing amorphous alloys exhibit good corrosion resistance in their solutions at room temperature. The corrosion resistance is largest for the Nb-containing alloy, followed by the Ti-containing alloy and then the Zr-Al-Ni-Cu alloy. The corrosion resistance of the Nb-containing alloy is also superior to that of the pure Zr metal, indicating the remarkable effectiveness of Nb addition on the improvement of corrosion resistance even in the NaCl solution.

Other properties of amorphous alloys

Recently, the Zr–Al–Ni–Cu bulk metallic glasses with a wide supercooled liquid region before crystallization were found to exhibit a distinct plateau stage in the hydrogen pressure–concentration–isotherm relation, though the desorption ratio of hydrogen gas is very low (15%) [82]. It has subsequently been found that the desorption ratio increases remarkably in the Mg-based amorphous alloys and the desorption ratio reaches approximately 100% [83]. It is therefore said that the Mg-based bulk amorphous alloys are good candidate for hydrogen storage materials.

On the other hand, the Pd-based bulk metallic exhibits very high efficient ratios for the generation of chlorine gas as an electrode material [77]. The high efficiency above 90% remains unchanged even after 500 cycles, though the efficiency of the commercial pure Pt crystal decreases significantly after 20 cycles. The remarkable improvement of the generation efficiency of chlorine gas has already enabled us to use the Pd-based bulk amorphous alloy as a practical electrode material for the generation of chlorine gas.

1.2.6 Application of bulk metallic glasses

For the past years, bulk metallic glasses have been developed in many alloy systems. As a result, the largest diameter of metallic glass exceeding 10 mm in many alloy systems, and the research and development research of metallic glass has advanced to a new era. So far, the principal areas of BMG products are sports, luxury goods, electronics, medical, defense, etc.

Liquidmetal Technologies [7], which was founded in 1987 as Amorphous Technologies International, was the first company to produce amorphous metal alloys in viable bulk form. The first application was as golf club heads. Twice as hard and four times as elastic as Ti drivers, 99% of the impact energy from a BMG head is transferred to the ball (compared to 70% for Ti). Higher strength-to-weight ratio allows mass to be distributed differently, enabling various shapes and sizes of head. However, high production costs led to Liquidmetal Technologies to terminate manufacture in favor of licensing the technology to established club makers. Vitreloy can also yield stronger, lighter, and more easily molded casings for personal electronic products. In 2002, Liquidmetal began making components for liquid crystal display casings on cell phones, but the costs became a problem again. However, now a few BMGs casings have been still chosen by some technological companies for their personal computer screens, digital cameras, or laptops.

Since the cast produces interest other valuable customers, the new manufactures started produce the baseball bats featuring and the four areas of the tennis-racket frame (Figure 1.16). The increased stiffness enhances energy return with 29% more power [84]. Other applications in sporting goods include skis, fishing equipments, bicycle frames, and marine tools, etc.

Most of BMGs provide the anti-scratch, dent-resistant and high-gloss properties. Thus, jewelry division and luxury watchmaker also use these BMGs for their valuable goods.

Some BMGs also have a highly biocompatible, nonallergenic form, wear-resistant, anticorrosion and other special medical properties. For example, DePuy Orthopaedics is using these materials in knee-replacement devices. And Surgical Specialties begin producing ophthalmic scalpel blades using these BMGs. The scalpel blades are higher quality but less expensive than diamond, sharper and longer lasting than steel, and more consistently manufacturable, since they are produced from a single mold ready for use. Other applications include pacemaker casings, knives and razor blades.

Some lightweight and inexpensive bulk metallic glasses [84] (e.g. Al-based alloys to replace Ti) are being developed for applications by multi-institution US Department of Defense (DoD) programs, including: the Defense Advanced Research Projects Agency (Fe, Al, Ti, and Mg based BMGs); the Caltech Center for Structural Amorphous Metals (Mg and Al based BMGs); the University of Virginia, University of Connecticut, and US Air Force (Al-based BMGs); the Texas A&M University (Zr-based BMGs and composite with crystalline phase powder); the Center for Science and Engineering of Materials at Caltech (Zr-based BMGs and other two-phase glassy alloys); the National Aeronautics and Space Administration (Zr-based BMGs and secret amorphous metals), and Liquidmetal Technologies (Zr and W based BMGs and composites), etc.

The DoD wants to develop military materials that are stronger, lighter, and more effective at high temperatures and stresses. For instance, in-situ W-reinforced BMG-composites can replace depleted uranium penetrators in antitank armor-piercing projectiles, because of their similar density and self-sharpening behavior. It is unlike most crystalline metal projectiles which flatten on impact, the sides of BMG-composites sheer away under dynamic loading. Other martial applications include lightweight fragmentation bombs, Lockheed Martin missiles and ceramic-BMG composite armor tiles.

There are lots of good prospects for BMG materials whose properties favor easier and cheaper processing for more common-place applications. For example, a micro/nano forming or imprint technology [85-88] for micro electromechanical systems (MEMS) and microstructure fabrication is introduced where the bulk metallic glass (BMG) is formed at a temperature where the BMG exist as a viscous liquid under an applied pressure into a mold. This thermoplastic forming is carried out under comparable forming pressure and temperatures that are used for plastics. It also allows to net-shape three-dimensional parts on the micron scale. The technology can be implemented into conventional MEMS fabrication processes. The properties of BMG as well as the thermoplastic formability enable new applications and performance improvements of existing MEMS devices and nanostructures.

These promising works, together with developments in America, Japan, European Union, Taiwan, and other countries greatly improves the prospects for the discovery of new BMGs with properties that will enable practical manufacturing. In turn, this is likely to open up a new space of potential applications.

1.2.7 Workability of bulk metallic glasses

The deformation mode of metallic glasses is divided into two modes, namely, inhomogeneous and homogeneous modes [89-93]. Metallic glasses usually exhibit inhomogeneous deformation at temperatures about 100 K below the glass-transition temperature. This inhomogeneous deformation is localized in discrete and thin shear bands, resulting from its non-hardenable nature. In contrast, higher temperatures lead to a homogeneous deformation at lower strain rates below 10^{-3} s^{-1}. In this homogeneous deformation region, each volume element of the material contributes to the strain, resulting in a uniform deformation for a uniformly stressed specimen. However, the elongation on tensile testing is limited to below about 100% and the minimum strength is more than one-third of the room temperature strength which is much higher than that of ordinary crystalline alloys. Moreover, the metallic glasses usually crystallize at a lower temperature of one-half of the melting temperature. It is therefore, difficult to hot work the metallic glasses using a conventional method.

Recently, a number of glassy alloys with a wide supercooled liquid region (above 50 K) and high glass-forming ability have been discovered [15, 16, 94, 20, 91, 95]. These glassy alloys allow the production of large-scale bulk glassy materials by consolidation of the glassy powders and casting at low cooling rates. Also, availability of the bulk glassy alloys enables unique approaches for forming complex-shaped components through significant viscous flow inherent to the supercooled liquid.

The workability of the supercooled liquid in metallic glasses needs to be examined after preliminary investigations of its thermal and mechanical properties. Based on the many literatures, it is demonstrated that the determination of the workability of a BMG within the supercooled liquid regime is not straightforward. Several parameters, including the viscosity level, the supercooled temperature range, the workability index, and the thermal stability, must be sought simultaneously. These factors must be considered when the BMGs are applied for industrial applications.

1.3 Mg-based bulk metallic glasses

Among a large number of alloys, the Mg-based alloys have attracted attention especially due to a high strength to weight ratio and a low glass transition temperature. From the industrial needs of developing high strength materials with light weight, the Mg-based alloys have attracted more and more interest due to the lowest specific weight among all structural metallic materials. The Mg-based BMGs are regarded as a new family of promising materials with excellent specific strength and good corrosion resistance [96].

New Mg-based ternary amorphous alloys with a wide supercooled liquid region and a high glass formation ability have been developed in a number of alloy systems, such as Mg-TM-Y (TM = transition metal such as Cu, Ni, Zn). The formation of the Mg-based BMGs was firstly reported in 1991. Then, Inoue et al. [97] found that the Mg-Cu-Y alloys exhibited a high glass formation ability (GFA), which made it possible to produce bulk amorphous samples with a diameter of 4 mm by the copper mold casting method. Furthermore, the Mg-based BMGs exhibited high compressive fracture strength of 800-900 MPa [98] which is more than twice as high as the highest strength of conventional Mg-based crystalline alloys. Next year, Inoue’s group [18] succeeded in fabricating bulk $Mg_{65}Cu_{25}Y_{10}$ metallic glasses with increased diameter up to 7 mm by using high-pressure die casting method. Since them, a new family of light amorphous alloy systems became available.

Chapter 2 Background and literature review

2.1 The forming conditions of amorphous alloys

A rapidly solidified amorphous phase is essential to suppress the nucleation and growth reactions of a crystalline phase in the supercooled liquid region between the melting temperature (T_m) and the glass transition temperature (T_g). In other words, the critical cooling rate (R_c) plays an important role in fabricating amorphous alloys. Furthermore, the critical cooling rate is also related with the alloy compositions.

2.1.1 The empirical rules for forming amorphous alloys

Take a binary system as an example. Most amorphous alloys have the compositions lying near the deep eutectic points. The reason for this is easy to understand. A schematic binary phase diagram in Figure 2.1 [99] compares the freezing of the two compositions. Composition 1 passes through the liquidus line at a high temperature (point a); thus the melt has to be cooled over a very larger temperature range over which it is possible for crystalline phases to form and grow. On the other hand, the liquidus line of composition 2 lies at a much lower temperature (point b) so that the thermal energy available for crystal growth is smaller, and at the same time the temperature interval between the T_m and the T_g is small. Frankly, the amorphous structure can be obtained with this latter composition using a slower rate of cooling.

The Inoue's group had developed a series of amorphous alloy systems with high GFA in the past decade, and they summarized and proposed three simple empirical rules for the alloy design of BMGs with high GFA [64, 77, 95, 100]. The three empirical rules are presented as below:

(1) Multi-component system consisting of more than three main elements:

For the alloy system with more than three main elements, the difference of atomic sizes causes a retardation of atoms moving when quenching this melt into a solid state. Consequently, the atoms of the solid phase exhibit a short-range order arrangement, which leads to denser random packing. For this reason, the GFA of amorphous alloys will be improved with increasing categories of main elements that consist of the multi-component system.

(2) Above 12% difference in atomic size ratios among the main elements:

In the Hume-Rothery criterion [99], the forming condition of the solid solution is that the difference of atomic sizes should less than 15% between the solute and solvent. If the difference of atomic sizes is lager than 15%, the moving atoms will be retarded accordingly. Thus the viscosity of the melting alloy also increases, and the atoms cannot rearrange easily in the solidified process. With the increase of atomic sizes difference, the GFA of amorphous alloys can be largely improved.

(3) Negative heats of mixing among the main elements:

According to the thermodynamic theory, the heat of mixing is regarded as the ability of atomic bonding between two atoms in an alloy system. Larger negative heat of mixing refers to the fact that the bonding ability of the same atoms is very weak, but the bonding ability for distinct atoms is strong. When the liquid alloy is solidified with a larger negative heat of mixing, the distinct atoms tend to attract together and arrange in a random way. Accordingly, the amorphous alloys form easily when the distinct main atoms have the larger negative heat of mixing (around -20 ~ -30 kJ/mol). Table 2.1 [101] lists the summary of ternary amorphous systems and mixing enthalpy values of three binary subsystems calculated based on Miedema's macroscopic model.

2.1.2 The correlative theories of empirical rules

The three important empirical rules can be explained from a great deal of experimental data as well as many theories. Therefore, various models describing the GFA of amorphous alloys have been proposed up to now, and these models can also be classified into three groups, i.e. the thermodynamics, kinetics, and structure [77].

(1) A view of the thermodynamics:

For an amorphous alloy with a high GFA, the free energy (ΔG) of amorphous state must be lower than the crystalline state of the same alloy. Thus the liquid alloy will cool down to form an amorphous phase rather than the crystalline phase. In the thermodynamic relationships of the Gibbs free energy $\Delta G = \Delta H_f - T\Delta S_f$ where ΔH_f is the enthalpy of fusion and ΔS_f is the entropy of fusion, a low ΔG value is acquired in cases of low ΔH_f and large ΔS_f. The ΔS_f is proportional to a number of elemental categories, so larger ΔS_f is obtained in the multi-component alloy system. Under a constant temperature situation, the free energy also decreases in cases of low chemical potential that is caused by low the ΔH_f and the high liquid/solid interfacial energy.

(2) A view of the kinetics:

In 1969, Turnbull [45] discussed the GFA of amorphous alloys by using the point of view of nucleation. He pointed out that the crystalline reaction of melting alloys is going to get fast and fast after the first nucleus appears in the liquid. So the nucleation rate must slow down a lot, resulting that stable nucleus cannot be formed in the system.

If the homogeneous nucleation rate is I under a cooling process, the numbers of forming nuclei (N) are

$$N = V\int_0^t I dt\,, \tag{2-1}$$

where V is the system volume. The forming condition of amorphous alloys is

$$V\int_0^t I dt < 1\,. \tag{2-2}$$

Consequently, the homogeneous nucleation rate (I) can be rewritten as

$$I = \frac{nD}{a_0^2}\exp\left[\frac{-16\pi\gamma_i^3}{3kT(\Delta g_v)^2}\right], \tag{2-3}$$

where n is the total number of atoms in a unit volume, D is the atomic diffusion coefficient at the liquid/solid interface, a_0 is the spacing between two atoms, γ_i is the liquid/solid interfacial energy, k is the Boltzmann's constant, Δg_v is the difference of activity between liquid and solid phases in the unit volume, V is the unit volume of the system and t is the cooling time that cools the liquid from T_m down to low temperature T. According to equation 2-2, the VIt must be less than 1 in order to form the amorphous phase while the nucleation rate does not change with time. Thus the forming condition of the amorphous phase depends on not only the stable nucleation reaction, but also the volume of liquid and the cooling time (cooling rate).

In the Fulcher equation [102], there is a connection with the flowability (ϕ), the viscosity (η) and temperature (T) in the liquid system, namely,

$$\phi = \frac{1}{\eta} = \phi_0 \exp\left[\frac{-A}{T - T_0}\right]. \tag{2-4}$$

The η value equals to $10^{-3.3}\exp(3.34/T_r - T_{rg}')$ in the general situation where $T_r = T/T_m$ and $T_{rg}' = T_g/T_m$, and therefore the interval of supercooled liquid can be judged by the dimensionless index. Here, ϕ_0, A and T_0 are constants. As to amorphous materials, the relationship between ϕ and D is

$$D = BT\phi, \tag{2-5}$$

where $B = k/3\pi a_0$ = constant. By putting equations 2-4 and 2-5 into equation 2-3, one can conclude that the homogeneous nucleation rate of a small supercooled liquid region is

$$I = \frac{nkT}{3\pi a_0^3 \eta} \exp\left[\frac{-16\pi\gamma_i^3\beta}{3T_r(\Delta T_r)^2}\right], \tag{2-6}$$

where $\Delta T_r = 1 - T_r$, $\alpha = (N_0V^2)^{1/3}\sigma/\Delta H^g{}_m$, $\beta = \Delta S^g{}_m/R$, and R is the gas constant. On the other hand, the homogeneous nucleation rate of a large supercooled liquid region [102] is

$$I = \frac{nkT}{3\pi a_0^3 \eta} \exp\left[\frac{-16\pi\gamma_i^3\beta}{3T_r^3(\Delta T_r)^2}\right]. \tag{2-7}$$

Here, the α and β are two important parameters in the crystalline process. According to equations 2-4 and 2-7, the nucleation rate will decrease when the liquid alloy has larger

T_r value.

The homogeneous nucleation rate (I) and growth rate (U) of a spherical crystalline phase can be calculated by equation 2-7 and expressed as

$$I = \frac{10^{27}}{\eta} \exp\left[\frac{-b\alpha^3\beta}{T_r^3(\Delta T_r)^2}\right], \tag{2-8}$$

$$U = \frac{10^3 f}{\eta}\left[1 - \exp\left(\frac{-\beta\Delta T_r}{T_r}\right)\right]. \tag{2-9}$$

Here, the b, a shape factor, is $16\pi/3$ for a spherical nucleus, and f is the fraction of nucleus at the growth interface. The α and β are dimensionless parameters and related to the liquid/solid interfacial energy. They can be presented as $\alpha = (N_A V)^{1/3}\gamma_i/\Delta H_f$ and $\beta = \Delta S_f/R$ where N_A is the Avogadro constant. Therefore, α, β and η are the important factors for GFA because the values of U and I decrease with the increasing three factors. The increasing α and β values refer to the increase in γ_i and ΔS_f and a decrease in ΔH_f. These results are consistent with the concepts of the thermodynamics. Furthermore, the $\alpha^3\beta$ parameter, related to the thermal stability of the supercooled liquid, is another important factor of GFA. For instance, when the value of $\alpha^3\beta$ exceeds 0.9, the unseeded liquid cannot crystallize at any cooling rate. Also when the value of $\alpha^3\beta$ is smaller than 0.9, the crystalline behavior cannot be stopped in the liquid.

(3) A view of the structures:

From the combinative concepts of the significant difference in the atomic sizes and negative heat of mixing, the fraction of denser random packing and high liquid/solid interfacial energy are two distinct factors needed to take into account for the supercooled liquid. Furthermore, the difficult atomic rearrangements lead to low atomic diffusivity and viscosity.

To sum up the three options mentioned above, the high GFA is attributable to form a new kind of supercooled liquid with the denser random packing. As shown in Figure 2.2 [64], there are three characteristics for a particular liquid structure. One with a higher liquid/solid interfacial energy leads to the suppression of nucleation of a crystalline phase; another with higher viscosity causes an increase in T_{rg}; the other with a lower atomic diffusivity induces the suppression of crystalline phase growth.

2.2 Viscous flow behavior

The first study of viscous flow behavior on a BMG above the liquidus temperature was conducted by Johnson and co-workers on $Zr_{41.2}Ti_{13.8}Cu_{12}Be_{22.5}$ (Vit1) in 1993 [20]. Contrary to the monatomic and binary simple metallic liquids which exhibit low viscosities of about 10^{-3} Pa·s [103] at the melting point, the viscosity of Vit1 was found to be about 3 orders of magnitude higher than that of a simple liquid. The Masuhr et al.'s study [103] assumed a Maxwell kinetic model that predicts extremely small relaxation times on the order of 10^{-10} s at the liquidus temperature (T_{liq}). Due to this high mobility and small relaxation time, it was assumed that the system would reach equilibrium rapidly and that there would be no shear rate dependence of the viscosity above T_{liq}. Later in 2004, the viscosity of Vit1 was revisited by Busch and co-workers, and surprisingly a pronounced shear rate dependence of the viscosity for temperatures above the T_{liq} [104] was observed. The results of this study suggested that there is an order of magnitude drop in viscosity for a two order of magnitude increase in shear rate indicating a non-Newtonian shear thinning behavior.

The above research supports that the viscosity behavior of BMGs needs further exploration. It will be shown in this thesis that the viscous flow kinetics in the Mg-based BMGs is even far more complex than previously anticipated.

2.2.1 Thermodynamics and kinetics of metallic glasses

BMGs have a unique combination of superior mechanical properties in the domain of high-strength metals and processability like plastics, making them interesting engineering materials. The kinetics and thermodynamics of metallic glasses have been subject to studies for a long time. However, due to the low thermal stability of metallic glass forming liquids, only data close to the glass transition or in the equilibrium melt could be obtained. The development of BMGs allows us to study the thermophysical properties such as heat capacity, viscosity, surface tension, and emissivity of metallic melts in the supercooled liquid region. This is because of their high thermal stability to crystallization and a large supercooled liquid region above the glass transition temperature than the conventional metallic glasses [105].

There are several theoretical approaches to describe the thermodynamics and kinetics of supercooled liquids. The thermodynamics are represented by the change of specific heat capacity, entropy, enthalpy and Gibbs free energy upon undercooling, and the kinetics can be investigated by measuring the viscosity above the liquidus temperature and in the supercooled liquid region.

Bulk metallic glass formers allow us to investigate the thermodynamic functions of supercooled metallic liquids on a broader time and temperature scale. The thermodynamic functions of the supercooled liquid with respect to the crystal can be determined in a Differential Scanning Calorimeter (DSC) and in a Differential Thermal Analyzer (DTA). This is done by measuring the heat of fusion, heat of crystallization and specific heat capacity data on the supercooled liquid and crystal [105-108].

The phase transformations occurred upon heating the material lead to the absorption or release of energy. This energy can be recorded as a heat flow as a function of temperature in DSC and DTA. Figure 2.3 depicts the phase transitions that occurred during the heating of material in a DTA. The initial endothermic peak corresponding to the glass transition, T_g, provides a qualitative proof for amorphous state of the sample. Upon further heating, crystallization occurs exothermally at the crystallization temperature, T_x .The amount of heat released during crystallization is known as the heat of crystallization, H_x. When the sample is heated further an endothermic peak showing the melting of the sample can be seen in this figure. The onset of melting is shown by eutectic temperature, T_{eut} (sometimes termed as T_m) and the end is depicted by T_{liq} (sometimes termed as T_l). By integrating the area under these endothermic events, the enthalpy of fusion, H_f, can be calculated [107]. The entropy of fusion, S_f, can be calculated from H_f by using [109]:

$$\Delta S_f = \frac{\Delta H_f}{T_m}, \qquad (2\text{-}10)$$

where H_f is the enthalpy of fusion, Tm is the melting temperature.

The specific heat capacities at constant pressure, C_p, of the glassy, crystalline and supercooled liquid state are also measured in DSC with changing temperatures. Specific heat at constant pressure, C_p, is the amount of heat required to raise the temperature of the substance by one degree Kelvin at constant pressure and is given by [110],

$$C_p = \left(\frac{\delta Q}{\delta T}\right)_p = T\left(\frac{\delta S}{\delta T}\right)_p, \qquad (2\text{-}11)$$

where, δQ is the heat absorbed by a unit mass of material to raise the temperature by δT and δS is the entropy change. Figure 2.4 depicts the heat capacity curves for a glass, the corresponding liquid and the crystalline solid as a function of temperature for Vit1 [107]. The sudden increase in the heat capacity of the glass upon heating is the thermal manifestation of the glass transition. Thermodynamically, the glass transition, Tg, is defined as the point of inflection of the rising heat capacity. The specific heat of the crystal and liquid, $C_{p,xtl}$ and $C_{p,liq}$ can be represented by the following equations:

$$C_{p,xtl} = 3R+aT+bT^2, \tag{2-12}$$

and

$$C_{p,liq} = 3R+cT+dT^{-2}, \tag{2-13}$$

where R is the universal gas constant, a, b, c and d are the fitting parameters. For Vit1 the fitting parameters are reported as; $a = -9.653 \times 10^{-3}$, $b = 2.321 \times 10^{-5}$, $c = 7.560 \times 10^{-3}$ and $d = 8.167 \times 10^{6}$ in the appropriate units [107].

The entropy difference, S^{l-x}, between the liquid and crystal as a function of temperature can be calculated by integrating the specific heat using [111]

$$\Delta S^{l-x}(T) = \Delta S_f(T_m) - \int_T^{T_{liq}} \frac{\Delta C_p(T')}{T} dT', \tag{2-14}$$

where S_f is the entropy of fusion, T is the temperature, and $C_p = C_{p,liq} - C_{p,xtl}$. Similar to entropy, variation of enthalpy, H^{l-x}, with temperature is calculated with the knowledge of specific heat,

$$\Delta H^{l-x}(T) = \Delta H_f(T_m) - \int_T^{T_{liq}} \Delta C_p(T')\, dT'. \tag{2-15}$$

By knowing the enthalpy, entropy of fusion and the specific heat capacity difference between supercooled liquid and crystalline mixture, C_p, the thermodynamic functions are calculated by integrating C_p as discussed above. This results in the Gibbs free energy difference between supercooled liquid and crystal,

$$\Delta G^{l-x}(T) = \Delta H_f - \Delta S_f \cdot T - \int_T^{T_f} \Delta C_p^{l-x}(T')dT' + T\int_T^{T_f} \frac{\Delta C_p^{l-x}(T')}{T'} dT' , \qquad (2\text{-}16)$$

where H_f and S_f are the enthalpy and entropy of fusion, respectively, at the temperature T_f. This gives us an approximation of the thermodynamic driving force for crystallization. Figure 2.5 shows a plot of the Gibbs free energy difference for some of the metallic glass forming systems as a function of undercooling [112]. The temperatures are normalized by the melting temperature of the respective alloy. The alloys plotted have the different critical cooling rates.

It can be seen in the plot that the best glass former with the lowest critical cooling rate of 1 K/s (Vit1) has smaller Gibbs free energy differences than the other glass formers, whereas the binary $Zr_{62}Ni_{38}$ with the critical cooling rate of about 10^4 K/s has the highest Gibbs free energy difference. This is consistent in all the glass formers shown in the Figure 2.5 and the glass former with smaller critical cooling rate has a smaller driving force for crystallization. Therefore in order to understand the glass forming ability of the alloys, it is a prerequisite to understand the thermodynamic conditions for good glass formation as well as its relation to the kinetics in the supercooled liquids.

2.2.2 Kinetics and viscosity of metallic glasses

Along with thermodynamics it is also essential to study kinetics in the proximity of glass transition region and above the liquidus temperature in order to understand the glass forming ability of BMGs. In terms of kinetics, the glass transition temperature can be understood as the temperature at which the viscosity (η) of the undercooled liquid reaches about 10^{12} Pa·s [1]. At such high viscosities, atomic motions are retarded and the relaxation time for atomic rearrangement becomes comparable to or greater than the experimental time scale.

The viscosity, η, is calculated by the Stefan equation [113] with the geometrical correction of viscous flow,

$$\eta = \left(\sigma \big/ 3\dot{\varepsilon} \right) \bullet \left[1 + d_0^2 \big/ 8 l_0^2 (1 + \varepsilon_n)^2 \right]^{-1}, \tag{2-17}$$

where σ, $\dot{\varepsilon}$, d_0 and ε_n are the true stress, strain rate, initial sample diameter, and nominal strain, respectively. In the equation, the true compressive stress σ is calculated using, $\sigma = (F/A_0)(l/l_0)$, where F, A_0, l and l_0 are the applied load, initial cross-sectional area, the specimen final length, and initial length, respectively. The viscosity values vary from 10^6 to 10^{10} Pa·s. They are noted to decrease initially with increasing temperature and reach a minimum when the temperature is close to the supercooled liquid region. Above T_g, crystallization begins to occur and viscosity increases.

Kato et al. [114] have studied the temperature dependence of η as a function of the relaxation time (λ) and heating rate (ϕ). They pointed out that in the temperature range where the relaxation time is comparable to or smaller than the inverse of the heating rate, i.e. $T \geq T_g + 20$ K ($\eta \leq 10^8$ Pa·s), η can be directly measured from the creep experiment under an isochronal heating test. However, in the temperature range over which λ is larger than α^{-1}, i.e., $T < T_g + 20$ K ($\eta > 10^8$ Pa·s), isothermal creep measurements should be employed in determining η.

Viscosity reflects the kinetic slowdown, when a liquid is supercooled below its melting point. Contrary to the monatomic and binary simple metallic liquids which exhibit low viscosities of about 10^{-3} Pa·s [115] at the melting point, BMGs are expected to possess much higher viscosities. For example, the viscosity of Vit1 is more than 3 orders of magnitude higher than that of a simple liquid. If we assume that the diffusivity is given by the Stokes Einstein equation as Diffusivity $\propto T/\eta$ [115], it is apparent that the crystallization kinetics is substantially retarded in an alloy with high viscosity. Therefore it has been argued that in Vit1, high viscosity is a major contributing factor to the high glass forming ability, because high viscosity implies a slow nucleation and growth kinetics in the supercooled liquid region.

2.2.3 Angell plot and Vogel-Fulcher-Tammann (VFT) formula

Glass formation has been studied in a large variety of materials. An empirical concept to describe the sensitivity of the viscosity to temperature changes for different materials in the supercooled liquid state was developed by Angell [1]. Figure 2.6 shows an Angell plot which describes the temperature dependence of viscosity for various materials.

The temperature dependence of viscosity can differ substantially among different materials. For example, the viscosity of strong ceramic glass SiO_2, which is an open random network glass, can be described well with an Arrhenius law [110]. Other substances such as materials with van der Waals bonds are best described by a Vogel-Fulcher-Tammann (VFT) relation with a VFT-temperature very close to the glass transition. The VFT-equation is given as,

$$\eta = \eta_0 \exp[\frac{D^* T_0}{(T - T_0)}], \tag{2-18}$$

where η_0 is a constant of about 4×10^{-5} Pa·s, D^* is the fragility parameter and T_0 is the

VFT temperature, where the barriers with respect to flow would go to infinity. “Strong” liquids, like SiO_2, have a low T_0 temperature and high melt viscosities and a D^* of about 100, whereas the other extreme are "fragile" liquids that show a VFT temperature, T_0 close to the glass transition temperature, as well as low melt viscosities and a D^* of less than 10. Conventional metallic glasses were considered to be fragile liquids with D^* less than 10 and it was not possible to perform viscosity measurements in the vicinity of glass transition due to their poor stability against crystallization. The development of BMG forming liquids made it possible to measure the viscosity by three point beam bending [116], parallel plate rheometry [106, 117, 118] as well as rotating cup viscosimetry [103, 104].

Early viscosity measurements on the Zr-based metallic glasses showed that the BMGs exhibits a “strong” as opposed to “fragile” liquid behavior, in contrast to what was previously assumed for the Mg-, Al-, Pd-, and other metallic liquids [103]. It was proposed that this high viscosity has an important influence on the crystallization kinetics and glass forming ability of multi-component glass forming alloys, because it implies smaller diffusivities than in very fluid liquids. The viscosity data obtained in this work are also analyzed in terms of the Angel plot, and the fragility parameters for various alloys are obtained by fitting viscosity as a function of temperature using the VFT relation.

2.3 Crystallization of supercooled metallic liquids and glasses

In order to study crystallization kinetics, the time-temperature-transformation (TTT) diagrams from the supercooled liquid into the crystalline state are studied. In a TTT diagram, the temperature is plotted on the vertical axis and the time on the horizontal axis on a logarithmic scale. A TTT diagram is obtained through isothermal experiments at various temperatures, and the time required by the material to crystallize at each isothermal temperature is plotted. Various curves, such as the onset (1%), intermediate (~ 50%) and end (99%) time of crystallization, are represented by such TTT diagrams.

A glass is formed by avoiding crystallization of the material below its melting point. Although the driving force for crystallization increases as the material is cooled more and more below its melting point, the diffusivity of the components in the alloy decreases with decreasing temperature. The decreasing kinetics (reduced diffusivity) below the liquidus temperature and the increasing driving force for crystallization are antagonistic and result in the characteristic "C" shape in the TTT diagram. As the material is cooled below its liquidus temperature, the time which is taken for initiation of crystallization decreases. The increase in the driving force for crystallization controls the crystallization process. This trend continues till the nose of the TTT diagram is reached. The nose corresponds to the minimum amount of time required to begin crystallization at any undercooling. Below the nose sluggish kinetics of the system takes over and governs the crystallization onset. The crystallization proceeds in different manners in various alloys. Figure 2.7 shows a TTT diagram of Zr-based amorphous alloy, where the isothermal onset of crystallization has been determined in the entire supercooled liquid for a metallic liquid.

The TTT diagram is analyzed by applying classical nucleation and growth models and taking the measured thermodynamic and kinetic quantities into account. The results can then be compared with the experimentally determined number of nucleation and growth events provided by the microstructure analyses.

According to the classical nucleation theory [119], the time for the crystallization, t_x, is given by

$$t_x = \left(\frac{3x}{\pi \cdot I_{ss} \cdot u^3} \right)^{1/4}, \tag{2-19}$$

where x is a small volume fraction to crystallize, I_{ss} is the steady state nucleation rate and u is the growth velocity. The steady state nucleation rate, I_{ss}, can be described by

$$I_{ss} = A \cdot D_{\text{eff}} \cdot \exp\left(\frac{-\Delta G^*}{k_B \cdot T} \right), \tag{2-20}$$

where A is a fitting parameter, D_{eff} is the effective diffusivity, k_B is a Boltzmann's constant, T is the temperature, and ΔG^* is the activation energy barrier for nucleation. D_{eff} can be calculated from the Stokes-Einstein equation given by

$$D = \frac{k_B \cdot T}{3 \cdot \pi \cdot \eta \cdot a}, \tag{2-21}$$

where η is the viscosity and a is average atomic distance. The viscosity η as a function of temperature is taken from the experimental data. The nucleation barrier ΔG^* is given as

$$\Delta G^* = \frac{16 \cdot \pi \cdot \gamma_i^3}{3 \cdot \Delta G^2}, \tag{2-22}$$

where γ_i is the interfacial energy and ΔG is the driving force for crystallization and is approximated as the Gibbs free energy difference, $\Delta G^{l\text{-}x}$, of the supercooled liquid with respect to the crystalline mixture. ΔG is experimentally calculated from enthalpy, entropy and specific heat data**.** γ_i is used as a fitting parameter to model the experimental data. Similarly, the growth velocity, u, can be calculated by

$$u = \frac{f \cdot D_{\mathrm{eff}}}{l}\left(1 - \exp\left(-\frac{v_m \cdot \Delta G}{k_B \cdot T}\right)\right), \qquad (2\text{-}23)$$

where f is the fraction of sites at the liquid-crystal interface, l is the average atomic diameter, v_m is the atomic volume.

2.4 New viscosity measurement of bulk metallic glasses

Volkert and Spaepen in 1989 [120] reported the changes in the shear viscosity during relaxation in amorphous Pd-based bulk metallic glasses (BMGs). From 1995 to 1997, several studies [121, 122] examined the flow behavior of different BMGs and established their temperature and strain rate dependence. In 2001, Myung et al. [123, 124] also studied the non-isothermal viscous flow of the Co, Pd and Zr-based glassy alloys in the glass transition range and found the optimum temperature range for secondary working of these alloys by examining the relationships between the observed relative displacement, the applied stress and temperature. Most of these studies were carried out by measuring the stress–strain curves at selected strain rates and temperatures using an Instron universal testing machine.

2.4.1 Three point beam bending method

The viscosity of some "strong" BMGs near the glass transition temperature has been reported by investigating the deformation of amorphous beams by the three point beam bending method. The three point beam bending consists of a beam that is supported at the ends by sharp edges. The beam is deflected with a constant force (F) applied in the center of the beam. From the deflection rate (v) the viscosity is determined by the equation

$$\eta = -\frac{gL^3}{2.4I_c v}\left(F + \frac{\rho AL}{1.6}\right), \tag{2-24}$$

where g is the gravitational constant, I_c is the cross-section moment of inertia, ρ is the density of glass, A is the cross-sectional area, and L is the support span. In case of bulk metallic glasses, viscosities between 10^7 and 10^{14} Pa·s have been previously obtained by this method. For instance, Waniuk et al. [125] obtained the viscosity of Zr-based metallic glasses in the supercooled region by using three point beam bending method. They reported a decrease from 10^{13} Pa·s at 600 K to 10^7 Pa·s at 700 K and upon primary crystallization the viscosity increased by 1.5 orders of magnitude indicating a decrease in the atomic mobility. Similar studies have also been conducted on some other kinds of BMGs [106, 116].

Russew and Sbojanova [126] have reported the relationship between the viscous flow behavior and crystallization features of metallic amorphous alloys when continuously heated at a constant rate. Also, Russew et al. [121] established a relationship between the non-isothermal viscous flow and thermal expansion of a $Pd_{82}Si_{18}$ glassy alloy considered as free volume related phenomena. As for bulk metallic glasses, Bakke et al. [116] reported the viscosity of the Zr-Ti-Cu-Ni-Be alloy in the supercooled liquid state between the glass transition temperature, T_g and the crystallization temperature, T_x, where it displays the Vogel-Fulcher-Tammann (VFT) behavior.

2.4.2 Dimensional changes method

The other technique for viscosity measurement is the thermomechanical analysis

(TMA), in which the dimensional changes in a sample are the primary measurement, while the sample is heated, cooled, or fixed at a temperature. A simple schematic figure of a typical TMA instrument is shown in Figure 2.8 [127].

The sample is placed on a support within the furnace. Resting upon it is a probe to sense the changes in length, which are measured by a sensitive position transducer, normally a Linear Variable Displacement Transducer (LVDT). The probe and support are made from a material such as ceramics or quartz glass (vitreous silica), which has a low, reproducible and accurately known thermal expansion coefficient, and also has low thermal conductivity helping to isolate the sensitive transducer from the changing temperatures in the furnace.

A thermocouple near the sample measures its temperature. There is usually provision for establishing a flowing gas (nitrogen, helium, or other noble gases) atmosphere through the instrument, to prevent from oxidation and also to assist heat transfer to the sample. The load may be applied by static weights or by a force motor. This latter method gives the advantage that the applied load can be programmed to allow a greater range of experiments. The instrument is calibrated for position measurements by heating a sample such as aluminum metal whose expansion coefficient is accurately known. Sample sizes are commonly around 4 - 10 mm in height and width. It is important to prepare samples with clean, flat and parallel faces to avoid artefacts in the recorded curves.

There are a number of approaches for the temperature calibration. One method uses small flat pieces of pure metals, e.g. indium, sandwiched between thin discs of quartz glass. Melting the metal sandwich under the probe with a moderate load results in a sharp displacement of the probe. With care, a multi-layer sandwich can be built up using "fillings" of different metals, so that a multi-point calibration can be obtained in one experiment. The TMA curve for such an experiment is shown in Figure 2.9 [127].

The viscosity, η, can be calculated by the Stefan equation [113] with the geometrical. The viscosity values vary from 10^6 to 10^{10} Pa·s. For their measurements in BMGs, they are noted to decrease initially with increasing temperature and reach a minimum when the temperature is close to the supercooled liquid region. Above T_g, crystallization begins to occur and viscosity increases again.

There have been only a few attempts to study the viscous flow behavior in BMGs, including Co, Pd, and Zr based systems, using the thermomechanical analyzer (TMA) under continuous heating conditions [121, 124]. However, very limited data are available on the effective viscosity and stress related viscous-flow behavior in the Mg-based BMGs under a TMA compressive pressure. Only Busch [106], Scholorke [128] and Kim et al. [129] have reported the thermodynamics analysis and viscous flow in the Mg-based amorphous alloys.

Hence, this thesis is intended to search the optimum superplastic forming condition of the amorphous Mg based alloys, and to clarify the thermal stability and viscous flow behavior in the supercooled liquid and amorphous states considered in the frame of free volume theory.

2.5 Deformability of supercooled liquids

2.5.1 Deformation behavior

The T_g and ΔT_x values of bulk amorphous La-, Zr-, and Pd-based alloys measured at a heating rate of 0.67 K/s are 480 and 70 K for the La-based alloy, 650 and 85 K for the Zr-based alloy, and 575 and 95 K for the Pd-based alloy. There is a relationship between the maximum flow stress (σ_{man}) and the strain rate ($\dot{\varepsilon}$) in the supercooled liquid for La and Zr based amorphous alloys [130-132]. The linear relationship holds at all deformation temperatures, and the slope corresponds to the strain-rate sensitivity exponent (*m*-value). The *m*-value is measured to be approximately 1.0, indicating that the supercooled liquid has an ideal Newtonian flow, i.e., ideal superplasticity. Also, the deformation in the supercooled liquid takes place in a homogenous mode over the whole strain rate range from 1.5 x 10^{-4} to 7 x 10^{-1} s^{-1} [132]. This result also indicates that high strain-rate superplasticity is obtained in the supercooled liquid. The amorphous alloy exhibits an inhomogeneous deformation mode in the temperature range below T_g, and the flow stress decreases with increasing strain rate. Thus, deformation behavior differs significantly between the amorphous rigid solid and supercooled liquid.

Figure 2.10 [64] shows the change in the viscosity of the supercooled liquid for the $Pd_{40}Cu_{30}Ni_{10}P_{20}$ amorphous alloy during isothermal heating. The heating up to each deformation temperature is set at a heating rate of 0.33 K/s. Considering that the flow deformation becomes extremely easy in the viscosity range below 10^8 Pa·s, viscous flow deformation can proceed during long time period of 10^2 to 10^4 s in the temperature range between 600 and 650 K. The times are long enough to transform the viscous flow deformation into various kinds of complicated shapes because these amorphous alloys have high strain-rate superplasticity.

2.5.2 Microforming

By utilizing such as ideal superplasticity which can be achieved over a wide strain rate range in the supercooled liquid region, various kinds of micro-forming treatments have been developed for La, Zr-, and Pd-based amorphous alloys. Figure 2.11 shows the outer shapes of the La-based amorphous wire produced by tensile deformation at an initial strain rate of about 1 x 10^{-2} s^{-1} and 500 K [133] and metallic glass gear with an outer diameter of 1 mm prepared by die forging into gear-shaped silicon die for 103 s at 500 K [134].

Inoue et al. [134] have also obtained small amorphous gears by a die extrusion process in the supercooled liquid region of an amorphous $Zr_{65}Al_{10}Ni_{10}Cu_{15}$ alloy with much higher T_g compared with that of the La-based amorphous alloys. They examined the relationship between the extrusion pressure (P_e) and extrusion velocity (V_e) at 711 K in the supercooled liquid region for the Zr-Al-Ni-Cu amorphous alloy. There is a good linear relationship and the *m*-value is determined to be 1.0, indicating that the supercooled liquid also exhibits ideal superplastic behavior even in die extrusion. Amorphous Zr-based alloy gears are also produced by the die extrusion method. The extruded sample does not contain any crystallinity and has the same T_g and T_x values as those for the as-cast bulk amorphous alloys.

Figure 2.12 shows an outer morphology of a precision optical mirror prepared by press forging of the $Zr_{60}Al_{10}Ni_{10}Cu_{20}$ amorphous alloy for 600 s at 673 K [69]. In the as-forged state, the forged sample exhibits a smooth outer surface and good metallic luster. The outer surface retains good smoothness on a nanometer scale based on the date obtained with a surface roughness indicator. The three-stage amorphous gear with outer diameters of 5 - 7 mm is also prepared by press die-forging the $Pd_{40}Cu_{30}Ni_{10}P_{20}$ amorphous alloy for 600 sec at 630 K [135].

All micro-formed amorphous alloys retain the amorphous nature, and no distinct differences in thermal stability and mechanical properties are seen between the as-cast and micro-formed samples. The combination of high GFA, good microformability and good mechanical properties has already enabled some practical uses for these bulk amorphous alloys as microforged materials, such as fine machinery and fine precision optical parts.

2.5.3 Deformability parameter

It is generally recognized that, at a given heating rate (α), a BMG with lower $\eta_{\min}$ has a better and easier near-net shape capability with finer surface-printability [114]. To express the degree of workability of a supercooled liquid of metallic glasses, the deformability d^* has been defined as [114]

$$d^*(\alpha) = \log\left[\eta\left(T_g^*\right)/\eta\left(T_{\text{finish}}(\alpha)\right)\right], \tag{2-25}$$

where $\eta(T_{\text{finish}}(\alpha)) = \eta_{\min}(\alpha)$, and T_{finish} is the devitrification or crystallization temperature. With α = 0.167 K/s in the present study, $d^*(\alpha)$ can be calculated from Eq. 2-25. Another parameter $\Delta T^*_x = (T_{\text{finish}} - T^*_g)/T^*_g$ represents the normalized supercooled temperature range of the BMGs under loading (or deformation).

2.5.4 Deformation model

The homogeneous deformation of BMG can be described by a free-volume model developed by Spaepen [136] and Argon [137]. The stress-strain-temperature relationship follows:

$$\dot{\gamma} = 2\exp\left(-\frac{\beta v^*}{v_f}\right)\left(\frac{\gamma_0 v_0}{\Omega}\right) J \exp\left(-\frac{\Delta G^m}{kT}\right)\sinh\left(\frac{\gamma_0 v_0 \tau}{2kT}\right), \tag{2-26}$$

where $\dot{\gamma}$ is the shear strain rate, β is a geometrical factor between 1 and 0.5, v^* is the effective hard-sphere size of the atom, v_f is the average free volume of an atom, γ_0 is the shear strain of a basic flow unit or shear transition zone (STZ), v_0 is the volume of a flow unit, Ω is the atomic volume, J is the atomic vibration frequency, ΔG^m is the thermal activation energy, k is the Boltzmann constant, T is the absolute temperature, and τ is the applied shear stress. Yang et al. [138] pointed out that Eq. (2-26) at low stresses and a fixed temperature Eq. (2-26) can be simplified to

$$\ln(\dot{\gamma}) = \frac{\gamma_0 v_0}{2kT}\tau + A, \quad (2\text{-}27)$$

where $A = \ln((\gamma_0 v_0/\Omega)J)-(\beta v^*/v_f)-(\Delta G_m/kT)$ is a temperature dependent constant. It needs to be noted that the current TMA was conducted under the compressive mode. However, during the heating period, thermal expansion will produce a tensile displacement, which must be corrected before the actual material response to the compressive stress can be evaluated. At a low stresses and a fixed strain rate, Eq. (2-26) can also be simplified to

$$\tau = BT + \frac{2\Delta G^m}{\gamma_0 v_0}, \quad (2\text{-}28)$$

where $B = (2k/\gamma_0 v_0)[\ln\dot{\gamma}-\ln((\gamma_0 v_0/\Omega)J)+(\beta v^*/v_f)]$ is a strain rate dependent constant. The thermal activation energy of a single STZ, ΔG^m, can be determined from the intercept of Eq. (2-28).

2.6 Partial element replacement in Mg-Cu-Y(Gd) based bulk metallic glasses

According the empirical BMG formation criteria, the bulk glass formation should satisfy: (1) the multi-component alloy systems consisting of more than three elements, (2) large differences in atomic size between the constituent elements, (3) negative heat of mixing among the major elements, and (4) alloy compositions close to the deep eutectic point. In accordance with these rules for achieving high GFA, one of the important factors for the formation of the amorphous phase is related to a large difference in atomic size among the main constituents.

2.6.1 The effect of the boron element

The interstitial atom boron appears to be a suitable candidate can tighten the alloy structure and then stabilize the amorphous alloy against crystallization. On the other hand, due to the lightweight of the Mg-based alloys, it is widely used on the industry. Cheng [63] reported that by the addition of B, it will not degrade the density advantage of the $Mg_{65}Cu_{25}Y_{10}$ amorphous alloy (Table 2.2) and will show no harm on the GFA. It can also be rationalized the different crystallization behavior by the effect of atomic size, heat mixing, and the bond parameter.

From the DSC experimental results (Table 2.3) that the B substitution for Cu really provides better GFA. But an opposite trend is observed for the B substitution for Y; $Mg_{65}Cu_{25}Y_{10-x}B_x$ is accompanied by a lower GFA in DSC results. Therefore, the difference of crystalline phase and the mixing enthalpy value among the elements need to be considered in Mg-Cu-Y-B systems. The zero value of mixing enthalpy between Cu and B might be related to GFA for the alloys with x = 10 would again drop, since the abundant B content would promote B-containing (e.g. MgB_4) crystallization. It seems that there is an optimum B content to result in the highest GFA.

On the other hand, the addition of boron increases the hardness from 220 to 327 H_v for the $Mg_{65}Cu_{25-x}Y_{10}B_x$ (x = 0 - 5), and $Mg_{65}Cu_{25}Y_{10-x}B_x$ (x = 0 - 10) amorphous alloys. The activation energy of the $Mg_{65}Cu_{25}Y_{10}$ amorphous alloy for crystallization determined by the non-isothermal Kissinger method is 138 kJ/mol. With increasing boron content, it can be promoted to a high energy barrier against crystallization, and $Mg_{65}Cu_{22}Y_{10}B_3$ has a higher value of 156 kJ/mol. Because that the addition of boron can restrain the growth of Mg_2Cu and increase the activation energy.

2.6.2 The effect of the silver element

The effect of silver substitution for copper on the GFA and mechanical properties of the $Mg_{65}Cu_{25-x}Ag_xY(Gd)_{10}$ alloys are investigated by Park et al. [139, 140] to promote the GFA of Mg-based metallic glasses. With increasing Ag content in the Mg-Cu-Y(Gd) alloys, GFA increases when $x = 10$ (Mg-Cu-Y) and $x = 5$ (Mg-Cu-Gd) and then decrease with further replacement of Cu by Ag, as shown in Table 2.3. The increase of GFA by the partial replacement of Cu by Ag can be explained by the large difference in atomic size between Ag and other constituent elements [141], and the large negative heat of mixing for binary Ag-Mg and Ag-Y(Gd) pairs [142]. The high GFA of the alloy system satisfying the empirical rules has been interpreted to be as a result of the formation of dense liquid with smaller free volume and higher viscosity [64].

The thermal analysis and D_{max} in Mg-Cu-(Ag)-Y(Gd) alloys are summarized in Table 2.4. The parameters for GFA, i.e., ΔT_x and the γ value are also included in Table 2.4. Since the data are limited to consider the relationship between D_{max} and GFA parameters due to the absence of T_g in some alloys, it is difficult to evaluate the correlation of the GFA parameters. However, the data suggest that the GFA parameters given so far are not appropriate for fully representing the improved GFA in the Mg-Cu-(Ag)-Y(Gd) alloy systems.

The compressive fracture strength, fracture strain, and specific strength of the $Mg_{65}Cu_{20}Ag_5Gd_{10}$ BMG are 909 MPa, 2.21%, and 2.34×10^5 N m/kg, respectively. In contrast to most previously reported Mg-based BMGs, the $Mg_{65}Cu_{20}Ag_5Gd_{10}$ BMG exhibits minor yielding and plastic deformation, demonstrating that small changes in composition of amorphous alloys can have a effect on the enhancement of plasticity. It is considered that addition of an alloying element with a positive heat (Ag-Cu) of mixing with the other constituting elements may provide atomic-scale local inhomogeneity, enhancing the plasticity of BMGs.

2.7 Purpose of this work

Metallic glassy alloys exhibit some unique physical properties such as excellent elasticity and strength as compared to their corresponding crystalline alloys. Meanwhile, significant plasticity occurs in the supercooled liquid region, due to a drastic drop in viscosity at temperatures above T_g upon heating. Accordingly, it is possible to form products by means of the superplastic deformation capability over this temperature region. And such excellent workability and surface printability in the supercooled liquid state has been considered to be one of the most attractive properties of bulk metallic glasses. The homogeneous flow nature of amorphous metals with a low viscosity allows us to form easily into complicated shapes and surface patterns. In general, the low viscosity and high thermal stability (against crystallization) of the supercooled liquid are the two main prerequisites of BMGs required for superplastic applications.

Magnesium amorphous alloys are the lightest structural materials with a lower glass transition temperature, and have great potential applications in future. In addition, the Mg based BMGs exhibit sufficiently high glass forming ability, a sufficiently wide supercooled liquid region before crystallization, and high specific strength. Thus it is necessary for applications to study the flow behavior around and above T_g in metallic glasses.

The temperature dependence of viscosity of the Zr, Mg, La, and Pd based BMGs has been measured using various techniques, and is assessed on the basis of the fragility concept proposed by Angell in some papers [1, 2, 4]. Compared with the Zr, La and Pd based BMGs, the Mg amorphous glasses possess much lower T_g temperatures in the range of 140 - 160°C, enabling favorably low working temperatures for deformation applications. However, very few data are measured on the effective viscosity and stress related viscous flow behavior in the Mg-based BMGs under applied compressive stress.

Moreover, not only the thermomechanical properties and micro-forming are researched in this work, but also the effects of an addition of other element for viscous flow behavior and workability are explored. In addition, the relationships of viscosity, deformability, and workability are examined and recognized by using a deformation model.

The research works in this thesis are summarized below:

(1) Developing the Mg-Cu-Y systems amorphous ribbons to choose the composition with the best GFA of Mg-Cu-Y glassy alloys.
(2) Preparing Mg-Cu-Y bulk metallic glass with the best GFA to research the viscous flow behavior and micro-forming for the three-dimensional micro-lens.
(3) Progressing Mg-Cu-Gd BMG with silver or boron atoms for better mechanical properties or better GFA, and comparing the difference between the Mg-Cu-Gd base alloy and the modified Mg-Cu-(Ag, B)-Gd BMGs.
(4) Evaluating the thermal and thermomechanical properties, deformability, and workability in these Mg-Cu-(Ag, B)-Gd BMGs.
(5) Searching a deformability model to explain the relationship between workability, temperature, shear stress, and strain rate.

Chapter 3 Materials and Experiments

In this study, four different system alloys namely Mg-Cu-Y, Mg-Cu-Gd, Mg-Cu-B-Gd, and Mg-Cu-Ag-Gd with a large supercooled temperature range have been investigated. In order to research the deformability and of amorphous alloys, the Mg-Cu-Y specimens are micro-imprinted by a micro-lens die in this study. Further, by measuring thermomechanical properties, the relationships between workability, temperature, stress, and strain rate are established. The flowchart of procedures is displayed in Figure 3.1.

3.1 The preparation of amorphous alloy specimens

3.1.1 Materials

The pure elements are selected to prepare the preliminary metallic glasses. The purity of magnesium, copper, silver, yttrium, gadolinium, and boron are 99.99%, 99.999%, 99.99%, 99.9%, 99.9%, and 99.5%, respectively. The contents of the metallic glasses in this study in terms of atomic percent are summarized in Table 3.1, including the Mg-Cu-Y series, $Mg_{65}Cu_{25}Gd_{10}$ base alloy, B-containing $Mg_{65}Cu_{22}B_3Gd_{10}$ and Ag-containing $Mg_{65}Cu_{22}Ag_3Gd_{10}$ and $Mg_{65}Cu_{15}Ag_{10}Gd_{10}$.

3.1.2 Arc melting process

In this study a vacuum arc melting furnace [143] (Figure 3.2) designed by the Van-Long Company, is the first apparatus used in this study. Lincoln DC-400 power supply provides the main power with an operating current between 200 and 300 A. To prevent the ingot from oxidation, the high purity argon gas has to be purged into the furnace several times to flush the oxygen away, and then the inner environment of furnace must be filled with pure argon gas of 200 torr.

The arc-melting process is useful to melt all elements together uniformly before the next process. The boiling point of magnesium (1363 K) is much lower than the melting point of the other five elements (Cu, Y, Gd, Ag, and B) used in this research. Accordingly, they arc melting is not suitable for the pure magnesium alloy.

Before beginning of this process, the first step is to pack the element with the highest melting point at the position close to the negative tungsten electrode. This step is able to prevent the un-molten elements from being covered in the ingot, so as to make a homogeneous mixing composition of the ingot.

When a high voltage is added between two electrodes, an arc is formed with extensive heat and bright light. By using the releasing heat, the elements are mixed together and formed the pre-alloyed ingots of Cu-Y, Cu-Gd, Ag-Gd, and Cu-B-Gd etc. under a Ti-getter. Finally, the melting process shall be repeated at least three times to confirm the mixed composition.

3.1.3 Melt spinning technique

The melt spinning technique with a more rapid cooling capability is recognized as a convenient way to prepare amorphous ribbons. The single-roller melt spinning induction furnace is also provided by the Van-Long Company. Figure 3.3 [143] displays the setup of a single-roller melt spinning technique.

The first step of this process is to put the Cu-Y, Cu-Gd, Ag-Gd, Cu-B-Gd, etc, ingots and the pure magnesium into a pure iron-crucible with a thin layer of boron nitride (BN) which is covered on the inner surface. The BN layer is able to prevent the interactions between alloys and the iron die at higher temperatures and to enhance the flowing rate of the melting alloys when pouring.

Same as the arc melting process, several times of the purged noble gas step are necessary before the melt spinning process carries out. Then, the iron-crucible is placed in an induction coil with the argon atmosphere of 1.5 atm. When these ingots and pure Mg metal are melted completely, the melt is poured onto the surface of copper wheel with a higher rotation speed of 15 m/s. Result in the melt is cooled momentarily to become a thin ribbon type measuring about 10 mm in width and about 200 μm in thickness. If the cooling rate is fast enough, this specimen would be fully amorphous.

3.1.4 Injection casting process

The injection casting technique is similar to the melt spinning process. The chart of an injection casting process is shown in Figure 3.4. The first step is also to put the binary or ternary ingots and the pure magnesium into a pure iron-crucible covered with BN. When the ingots and pure Mg metal are completely melted together under 1.5 atm argon, the melt is poured into a copper mold with a cooling system to from the rectangular ternary or quaternion alloy pre-specimen. The volume of the pre-specimen is usually 10 mm (thick) x 30 mm (wide) x 90 mm (length), and it is not amorphous state solid yet.

The pre-specimen are broken to pieces, and then put into quartz tube covered with BN in the inner surface. Due to lower the melting points of the ingots, the pre-specimen will be melted much more easily under the argon atmosphere. As a result, the melt is injected into a cold copper mold with a higher cooling rate system by 4 atm argon. The final dimensions of amorphous rod specimens are 3 mm or 4 mm in diameters and at least 100 mm in length.

3.2 Microstructure and phase identification

3.2.1 XRD analyses

The amorphous nature of the as-quenched rod samples can be confirmed using X-ray diffractometry (XRD, Siemens D5000) with a monochromatic Cu-Kα radiation, a working voltage of 40 kV and electron current of 30 mA. The diffraction angle (2θ) covers from 20^{o} to 80^{o}, and every 0.1^{o} steps for 5 seconds. In order to confirm the fully amorphous state of samples, the outer oxidative layers of specimen surfaces need to be ground away before being analyzed by XRD.

3.2.2 SEM observations

The JEOL JSM-6400 scanning electron microscopy (SEM) is selected to observe the microstructure and morphology of the metallic glasses, and is also used to check whether the compositions of the metallic glasses are mixed homogeneously. The energy dispersive spectrometry (EDS) is used for precise measurement of the elements in the metallic glasses to confirm our compositions. In addition, the mapping function of the EDS system can also confirm the uniform atomic distribution.

3.3 Thermal analyses

By using the differential scanning calorimeter (DSC), the TA Instruments DSC 2920 (heat flux) and Perkin Diamond DSC (power compensation, Figure 3.5) are both used to measure the thermal properties of the metallic glasses. The scheme of DSC is presented in Figure 3.6.

For the ribbon specimens, the samples are heated to 873 K with a heating rate of 20 K/min. The glass transition temperature (T_g), crystallization temperature (T_x), melting temperature (T_m) and liquidus temperature (T_l) can be obtained in the non-isothermal DSC heating course. In accordance with these temperature data, the GFA indexes such as the γ value, supercooled range, reduced glass transition temperature, etc, are able to be estimated. On the other hand, for the bulk metallic glasses, the specimens are heated to a temperature below T_m with a slower heating rate of 10 K/min to compare with the data obtained from the thermomechanical analysis.

3.4 Mechanical properties

3.4.1 Hardness

In this study, the two classes of hardness testing, nano and micro hardness are examined by microhardness and nanoindentation testing. A Shimadzu HMV-2000 Vicker's microhardness tester (Figure 3.7) is used in the micro-scale testing, and the amorphous samples are performed by a load of 1.96 N for 10 s. The nanoindentation testing is executed with a maximum load of 500 mN by the MTS Nano Indenter XP (Figure 3.8), using the Berkovich tip.

Before carrying out this testing, a grinding step has to be implemented drastically. Particularly, the nanoindenter is highly sensitive to the external environment, as well as the flat condition of specimen surface.

3.4.2 Dynamic mechanical analysis

The Perkin Elmer Diamond dynamic mechanical analyzer (DMA, Figure 3.9) is applied to test the relaxed and strained specimens. The specimen is heated at constant heating rate from room temperature to 573 K, while applying a sinusoidal dynamic force at a constant frequency. Therefore, the applying stress can be expressed as $\sigma(t) = \sigma_0 \sin(\omega t)$, and the deformation $\varepsilon(t) = \varepsilon_0 \sin(\omega t - \delta)$ with phase shift is obtained as shown in Fig. 3.8. The in-phase response of the specimen is related to the frequency dependent Young's storage modulus $E'(\omega)$, which describes the cycled elastic energy, while the out-of-phase response is related to the Young's loss modulus $E''(\omega)$, which describes the energy loss in the cycle.

3.4.3 Thermomechanical analysis

It is necessary to grind a specimen with flat surface before subject to thermomechanical analysis (TMA). The metallic glass samples are held by chucks attached to the sample tube and the probe, as shown in Figure 2.8. The temperature dependences of the relative displacement, effective viscosity, and effective linear expansion coefficient measured using a thermomechanical analyzer (TMA 7, Perkin Elmer Diamond, Figure 3.10) under the isochronal (i.e., non-isothermal) condition at a heating rate of 10 K/min from 300 to 573 K and a fixed compression load of 50 mN. Temperature was calibrated by using pure In and Zn samples as standards. Displacement data under various pressures and temperatures were collected simultaneously upon heating. Applied stresses were generated by a 3.0 mm diameter TMA ceramic probe giving a probe to sample area ratio of 1. The as-cast amorphous samples used for TMA measurement are of a cylindrical shape with a diameter of 3 mm and a length of 6 mm.

The thermal stability during loading or forming was evaluated using TMA under an isothermal condition at a constant temperature of $T_g + 0.5\Delta T_x$ (where $\Delta T_x = T_x - T_g$) in the supercooled liquid region under a constant load of 10 mN to 5 N.

3.5 Imprinting (Micro forming)

The new process is used to fabricate a BMG mold to replicate micro-lens array on PMMA sheets by hot embossing using a conventional hot press operated in air, as show in Figure 3.11 The original convex mold is the Ni-Co die made by the electroplating and lithography processes, the mold morphology is shown in Figure 3.12. The patterns in the Ni-Co mold are the half-spherical and hexagonal micro-lens arrays, and each side of the hexagonal is around 185 μm. These patterns are formed into the secondary $Mg_{58}Cu_{31}Y_{11}$ BMG mold by hot pressing into the pattern shown in Figure 3.12(b). Finally, the concave pattern in the secondary $Mg_{58}Cu_{31}Y_{11}$ mold is further transformed to the PMMA sheets (Figure 3.13) [86, 87].

In this research, relationship between the load and strain during its initial imprinting stage is simulated by the commercial software DEFORM 3D for the load prediction. The simulation work was performed by the graduate students in Prof. Pan’s Lab in the Department of Mechanical and Electro-Mechanical Engineering of National Sun Yat-Sen University. The Ni-Co lens mold has a diameter of 330 μm and height of 14 μm, and the projected area of the hexagonal micro-lens array pattern is about 6.238×10^{-7} m^2. If the Ni-Co die is a male convex mole, then the direct imprinty for Ni-Co to PMMA transparent layer would produce the concave PMMA for the light focus purpose. In contrast, if the Ni-Co male coves die is used to imprint the Mg-based BMG, then the Mg BMG becomes the concave female die. A second imprint on the PMMA would produce the convex longer for the defecation purpose.

Chapter 4 Results and discussions

4.1 The Mg-based amorphous ribbons

General speaking, the thickness of amorphous alloys depends on the rotating speed of the cooling copper wheel in the single-roller melt spinning process. If the copper wheel rotates at fast speeds, the amorphous ribbons would show the thin and slight form; on the contrary, the thick and wide amorphous ribbons are obtained when the rotating speed of copper wheel is slow. In this study, the rotating speed is controlled at a constant level about 25 m/s (1200 rpm), and the Mg-based amorphous ribbons are measured about 10 mm in width and about 200 μm in thickness. These Mg-based amorphous ribbons all exhibit the metal-like shine, and there is still a slight difference between two surfaces of amorphous ribbons (Figure 4.1).

4.1.1 Microstructure

Figure 4.2 displays the X-ray diffraction patterns obtained from the $Mg_{67}Cu_{25}Y_8$, $Mg_{65}Cu_{25}Y_{10}$ and $Mg_{58}Cu_{31}Y_{11}$ melt spun ribbons. There is no detectable crystalline peak in the 2θ range of 20^o - 80^o, instead a broad diffused peak is observed in the range of 30^o - 50^o. This indicates that the three samples are all of the amorphous nature.

4.1.2 Thermal properties

The DSC thermograms of the three melt spun specimens are shown in Figure 4.3. All the specimens exhibit a clear glass transition temperature followed by a supercooled region and then exothermic reactions owing to crystallization.

The crystallization exothermic reactions for these three alloys in their DSC curves all appear as one single peak. The glass transition temperature (T_g), crystallization temperature (T_x), melting solidus temperature (T_m) and liquidus temperature (T_l) of the $Mg_{65}Cu_{25}Y_{10}$ amorphous specimen at a heating rate of 20 K/min are 417 K, 465 K, 709 K and 748 K, respectively. When the Y-element in the $Mg_{65}Cu_{25}Y_{10}$ ribbon is replaced by Mg, forming the $Mg_{67}Cu_{25}Y_8$ ribbon, the T_g, T_x, and T_m decrease to 407 K, 440 K, and 708 K, but the T_l increases to 770 K.

However, when some Mg atoms is replaced by Cu and Y, forming $Mg_{58}Cu_{31}Y_{11}$ amorphous ribbon, the T_g, T_x, T_m and T_l become even higher than the Mg-Cu-Y based alloy ($Mg_{65}Cu_{25}Y_{10}$). The thermal properties at the heating rate of 20 K/min are characterized in Table 4.1.

Based on the results from the DSC scans, it is suggested that the $Mg_{58}Cu_{31}Y_{11}$ specimen possesses a higher glass forming index (γ = 0.403 and γ_m = 0.697), and a larger supercooled region (ΔT_x) of 53 K than the other Mg-Cu-Y system alloys. This composition of $Mg_{58}Cu_{31}Y_{11}$ appears to be the most optimum composition with the best GFA are working temperature window for micro/nano forming practices.

4.1.3 Mechanical analyses

Hardness

Table 4.2 shows the hardness and modulus of the Mg-Cu-Y metallic glass ribbons, which were measured by micro/nano- indentation. The hardness data obtained from the nano-indenter in unit of GPa can be transferred into the equivalent H_v scale in conformity to the MTS manual. The nano-hardness data are always higher than the Vicker's microhardness data, due to the indented volume effect [144, 145].

The $Mg_{58}Cu_{31}Y_{11}$ specimen is obtained the highest hardness of 252 H_v from microindentation test, and the $Mg_{67}Cu_{25}Y_8$ and $Mg_{65}Cu_{25}Y_{10}$ displays lower values of 216 and 220, respectively. For the nano-indentation hardness data, $Mg_{58}Cu_{31}Y_{11}$ also exhibits the highest value of 3.34 GPa.

Dynamic mechanical analysis

The changes of rheological behavior of Mg-Cu-Y system metallic glass ribbons under dynamic conditions such as the storage modulus, E’, loss modulus, E’’, loss tangent, tanδ (= E’’ / E’) and glass transition temperature (T_g) are measured by DMA. As shown in Figure 4.4, before reaching the T_g temperature, the elastic modulus is almost constant due to the applied load is too low for the BMGs (maximum load is about 8 N). The elastic modulus of an amorphous alloy will tend to decrease significantly while the glass structure changes to viscous matter during heating. Then, the starting crystallization will lead the viscous matter to change to the crystalline matter, this will make the elastic modulus suddenly increase. Thus, the E’ decreases at temperature near T_g due to the change into viscous matter and then increases due to the occurrence of crystallization.

The ability of losing energy for the specimen deformation while heating is shown by the value of tanδ. The viscous flow behavior is accelerative to be deformed easily, so the tanδ increases when the temperature reaches the T_g, i.e., the softer and weaker matter causes the loss of energy during deformation. From the curve in Figure 4.4, the value of tanδ increases when the glass state transfers to supercooled region, followed by gradual decrease as a result of crystallization.

4.2 Thermal and thermomechanical properties of $Mg_{58}Cu_{31}Y_{11}$ bulk amorphous alloy

It is well known that the Mg–Cu–Y and Mg–Cu–Gd amorphous systems exhibit a wide supercooled liquid region before crystallization. The high thermal stability of the supercooled liquid enables the production of bulk amorphous alloys with maximum thickness up to about 27 mm (the maximum thickness of Mg-Cu-Gd is about 12 mm, and Mg-Cu-Ag-Gd is about 25~27 mm) [146]. But little researches have been reported on the effective viscosity, stress related viscous-flow behavior and specific heat in bulk amorphous $Mg_{58}Cu_{31}Y_{11}$ alloys under indentation pressure. The aim of this investigation is to find fundamental physical properties and using this basis to find the optimum conditions for viscous flow forming. The BMG used for the purpose is $Mg_{58}Cu_{31}Y_{11}$ rod specimen with a diameter of 3 mm, as shown in Figure 4.5.

4.2.1 Microstructure and thermal properties

X-ray diffraction (Figure 4.6 (a)) has verified that the as-cast $Mg_{58}Cu_{31}Y_{11}$ rod sample with a diameter of 3 mm is amorphous and Figure 4.6 (b) shows the DSC thermogram of that at a heating rate of 10 K/min. In the DSC experiments, we observed distinct glass transition phenomena, one exothermic crystallization peak and one melting peak from the as-cast and annealed samples, and the as-cast sample exhibits a sequential phase transition from the amorphous solid, through the glass transition, to the supercooled liquid, and finally the crystallized region.

The T_g, T_x, T_m and T_l of the $Mg_{58}Cu_{31}Y_{11}$ amorphous rod specimen at a heating rate of 10 K/min are 416 K, 467 K, 709 K and 752 K, respectively. The supercooled liquid region extends over a temperature interval of about 51 K at a heating rate of 10 K/min. The crystallization heat of the as-cast sample was found to be 3.48 kJ/mol.

4.2.2 Thermomechanical properties

Figure 4.7 shows the temperature dependence of the relative displacement of the as-cast bulk amorphous $Mg_{58}Cu_{31}Y_{11}$ alloys obtained by TMA operated under the compression mode at various stress levels and a heating rate 10 K/min. All samples have the same trend with increasing temperature, but the maximum displacement lengths are increased with increasing applied stress. We assume that small variations in relative displacement below T_g are due to sample/probe alignment. The relative displacement contracts significantly above the glass-transition temperature, indicating the easy deformability of the glassy alloy in the supercooled liquid region.

The maximum displacement (ΔL_{max}) occurs in the supercooled liquid region with values of 60.9 μm at 0.79 kPa, 162.6 μm at 2.38 kPa, 265.3 μm at 7.12 kPa, 748.6 μm at 117.83 kPa, and 923.3 μm at 318.52 kPa, as shown in Table 4.3. We used the applied stress and $\Delta L/L$ to estimate the modulus of the as-cast alloys in Figure 4.8.

Such displacements correspond to engineering strains $\Delta L_{max}/L_0$ (where L_0 is the original specimen height 4 mm) of 1.52%, 4.07%, 6.63%, 18.72%, and 23.08%. The relative displacements become pronounced at temperatures greater than T_g, indicating the high deformability of the glassy alloy in the supercooled liquid region.

Figure 4.9 displays typical TMA and DTMA curves measured at a stress level of 7.12 kPa for bulk amorphous $Mg_{58}Cu_{31}Y_{11}$ alloys. The DTMA curve is obtained from the derivative of the $\Delta L/L_0$ with respect to time. We have defined T_{onset} for the onset temperature for the viscous flow, T_{vs} for the semi-steady-state viscous flow temperature, and T_{finish} for the finish temperature for the viscous flow. Under a higher loading stress, crystallization tends to start at a lower temperature, and brings viscous flow to the end sooner. The T_{onset}, T_{vs}, and T_{finish} are marked on the TMA and DTMA curve, also compiled in Table 4.3.

4.2.3 Viscous flow behavior

The effective viscosity values at any temperature in the non-isothermal heating process can be obtained by means of the Stefan's equation with the geometrical correction (Eq. 2-17). Figure 4.10 shows the temperature dependence of the experimentally obtained effective viscosity for the quoted applied stresses at a heating rate of 10 K/min. This figure is plotted for temperatures higher than the T_{onset} of the effective viscosity curve at 7.12 kPa and the corresponding T_{vs} and T_{finish} temperatures are also labeled. Below T_{vs}, the effective viscosity of all samples decreases with temperature, with the highest applied compressive stress giving the greatest value of effective viscosity. The minimum effective viscosity occurs at T_{vs} with values of 8.02×10^6 Pa·s at 0.79 kPa, 8.75×10^6 Pa·s at 2.38 kPa, 1.05×10^7 Pa·s at 7.08 kPa, 6.74×10^7 Pa·s at 117.83 kPa, and 1.52×10^9 Pa·s at 318.52 kPa. However, the lowest applied stress gives the lowest rate of decrease in viscosity with increasing temperature.

In the annealed sample, the effective viscosity decreased with increasing test temperature. However, the value of effective viscosity of the sample annealed at a higher temperature for 5 min was larger than that of sample annealed at lower temperature for the same amount of time. Between T_{vs} and T_{finish}, the effective viscosity approached a constant value for each stress level.

4.2.4 Deformability

Figure 4.11 exhibits the change in ΔL/P (displacement/applied stress) at increasing temperature under the given applied stress levels, and suggests that T_{finish} is also lowered at higher stress. We also observed a large change in ΔL/P in the vicinity of T_{finish} (~ 20 μm/kPa for a applied stress of 0.79 kPa), and the magnitude of the ΔL/P values at T_{onset}, T_{vs}, and T_{finish} is greatest for the lowest applied stress (0.79 kPa). Myung et al. [147] reported the same result in the Pd-based amorphous alloy. However, it is difficult to determine the effects due to stress. To confirm the effect of applied stress on the viscous flow, we measured T_{onset} and T_{finish}, as shown in Figure 4.12. The T_{onset} decreases with increasing applied stress. It means the applied larger stress causes the metallic glass rod to flow deform more easily. However, the T_{finish} also decreases with increasing applied stress. Due to crystallization with a higher stress starts at lower temperature, and brings rapid viscous flow to end sooner.

Considering these results, the state of the bulk amorphous alloy changes easily at T_{vs} under all applied stresses. For secondary working with this alloy, the applied stress level and the values of the T_{vs} temperature at each stress level are very useful information.

4.2.5 Findings for $Mg_{58}Cu_{31}Y_{11}$ properties

In this section, the viscous-flow behavior and the relative displacement of $Mg_{58}Cu_{31}Y_{11}$ BMG are investigated using DSC and TMA. The crystallization heat of the as-cast sample is determined to be 3.48 kJ/mol at a heating rate of 10 K/min. Below T_{vs}, the effective viscosity of the $Mg_{58}Cu_{31}Y_{11}$ decreases with increasing temperature, with the highest applied compressive stress giving the greatest value of effective viscosity. By examining the relationship between the $\Delta L/P$ and temperature in TMA, important information under viscous-flow forming can be obtained. The optimum temperature for secondary working is T_{vs} at each stress level. The viscous flow properties of this sample open up possibilities for viscous-flow forming.

4.3 Micro-imprinting in Mg-Cu-Y metallic glasses

Compared with the Zr, La and Pd based BMGs, the Mg amorphous glasses possess much lower T_g temperatures in the range of 140 - 160°C, enabling favorably low working temperatures for micro-forming or micro-imprinting [148]. As presented in section 4.2, it is confirmed that the $Mg_{58}Cu_{31}Y_{11}$ amorphous alloy exhibited reasonably good GFA with a wide supercooled liquid region before crystallization. Also, the measured stress and strain curves from TMA data for this amorphous alloy at these three characteristic temperatures are shown in Figure 4.8. In this section, the comparison of the experimental observations and finite element simulations on the micro-imprinting behavior of this alloy is presented.

4.3.1 Finite element simulation

The finite element simulation, done in Prof. Pan's Lab and performed by Chen and Wu, was started from the beginning stage of the micro-imprinting stage. The glass transition temperature of $Mg_{58}Cu_{31}Y_{11}$ BMG is about 140°C. Therefore, temperature of 150°C is chosen for the hot embossing experiment and simulation. For simulation, the forming velocity of top die is first set to be low, i.e., 0.0005 mm/s, in order to explore the minimum applied load for the micro-imprinting. Based on the input stress and strain curves at various temperatures, the calculated pressure versus imprinting time is obtained, for example, at 150°C, as shown in Figure 4.13.

In the beginning stage within 120 s, the BMG can be formed at low pressures, in the neighborhood of 0.05 to 2 kPa. The residual material becomes thinner, resulting in sudden load increase over 180 - 360 s. The simulated results suggest that the $Mg_{58}Cu_{31}Y_{11}$ BMG can be formed from the first minute, with a low pressure less than

50 Pa. Nevertheless, the achieved strain is rather low, and the imprinted patterns are not well defined. With increasing time to over 360 s and pressure to about 2 kPa, the imprinting proceeds continuously. The current simulation is only for the initial stage of the micro-imprinting. To complete the imprinting into well defined hexagonal micro-lens arrays, much longer time and much higher load are necessary.

In reality, the forming speed of 0.0005 mm/s appears to be much lower than acceptable, thus a higher load is applied. The actual applied pressure needed for satisfactory forming is found to be above 100 kPa, for the practically acceptable forming time of a few minutes.

Experimentally, the deforming evolution of the micro-lens array on the BMG material with different forming time is shown in Figure 4.14, with parameters of embossing temperature at 150^{o}C, time duration of 4 min, and two different applied loads of 100 and 300 kPa. It was found that a higher applied pressure of 400 kPa is necessary. Figure 4.15 displays the forming extent of the BMG upon subject to an applied pressure of 400 kPa and forming time of 1 and 4 minutes by the spring plates. It will usually take about 4 minutes to complete the embossing process. When the embossing time is too long, the BMG material may be crystallized. Thus, the forming time of 4 minutes appears to be an optimum and acceptable time duration for the micro-imprinting.

4.3.2 Morphology of the micro-lens mold and imprinted specimens

Before the embossing process, it is obvious that there are some defects on the surface of a BMG raw material, which is created during its manufacturing process. Figure 4.16 exhibits the SEM micrograph of the typical surface morphology. To improve this, the surface was polished with abrasive papers.

The surface profiles of micro-lens in its original convex Ni/Co mold measured by α-step, imprinted concave Mg based BMG, and the final imprinted convex PMMA are shown in Figure 4.17. Note that the profile of the concave BMG has been reversed its sign for the sake of comparison. The original convex Ni/Co mold is 184.68 μm in width. This concave BMG mold is 183.56 μm in width and the roughness is less than 30 nm. Finally, the convex PMMA micro-lens is 183.44 μm in width and the roughness is also less than 30 nm. The shrinkage rate between the Ni/Co and BMG molds is 0.61 %, whereas the shrinkage rate between the BMG and PMMA molds is 0.06 %. Excellent replicated patterns can be obtained using the current processing parameters.

4.3.3 Comments for micro-imprinting

This study presents a new process to fabricate micro-lens array, utilizing the viscous flow behavior of the metallic glassed and polymer PMMA at temperatures slightly above their glass transition temperature. The working temperature for embossing is selected to be 150^{o}C, based on the DSC and TMA data. The Ni-Co mold with an inscribed circle 330 μm in diameter has been successfully fabricated out using the electroplating process. Excellent replicated patterns can be obtained using a larger applied pressure level. The result reveals that pressure level of 400 kPa and forming time of 4 minutes are good combinations to replicate a micro-lens array. The simulated results of the applied pressure and the resulting forming extent are in reasonable agreement with the experimental observation. The surface profiles of the original convex Ni/Co mold, imprinted concave Mg based BMG, and the final imprinted convex PMMA are closely matched, suggesting that the application of BMGs for micro-forming or micro-imprinting is feasible.

4.4 Workability and thermomechanical properties of Mg-Cu-(Ag, B)-Gd bulk metallic glasses

Based on our previous studies, it is shown that the $Mg_{65}Cu_{25}Gd_{10}$ specimen has a higher glass forming index (γ) of 0.43 and a larger supercooled region (ΔT_x) of 68 K than the $Mg_{58}Cu_{31}Y_{11}$ based system metallic glass specimens ($\gamma = 4.03$ and $\Delta T_x = 53$). The ΔT_l range represents the interval between T_m and T_l, and there is very minor difference between the ΔT_l in Mg-Cu-Y based systems. This suggests that the Mg-Cu-Gd is more valuable for glass forming ability and applications.

The previous studies [149, 150] also indicated that a suitable addition of 3 at% boron atoms into the Mg-Cu-Y(Gd) based BMGs could effective raise the GFA and thermal stability since the small boron atoms tend to occupy the free volume of the base BMG and tend to raise the difficulty of the diffusion of Mg and Cu atoms. Also, the hardness can be improved from 267 H_v for $Mg_{65}Cu_{25}Gd_{10}$ to 308 H_v for $Mg_{65}Cu_{22}Gd_{10}B_3$ alloy. The much higher hardness in the B-containg Mg-based alloys is a position greater of the micro-formed MEMS parts, enhancing the mini-part strength and wear-resistance. Then, Park et al. [140] reported that the replacement of Cu by 3-5 at% Ag atoms in the Mg-Cu-Gd BMG could increase the GFA because of the large difference in atomic sizes between Ag and other constituent elements and the large negative heat of mixing for Ag-Mg and Ag-Y.

Since we have demonstrate that both Mg-Cu-Y and Mg-Cu-Gd are promising caudiclates for micro-form and nano-impriaty, it is meaning ful to explore another the B or Ag additive Mg based BMGs also have the conyatible viscous flow capability for forming application. Thus, we examine the fragility and workability of the Mg-Cu-Gd based system with the addition of Ag or B, and correlates with the deformability behavior in the supercooled region.

4.4.1 Phase demonstration and thermal properties

Figure 4.18 indicates XRD patterns taken from the cross-sectional surfaces of the as-cast $Mg_{65}Cu_{25-x}Ag_xGd_{10}$ (x = 0, 3, 10 at%) and $Mg_{65}Cu_{22}B_3Gd_{10}$ amorphous alloy rods. Multiple crystallizations are observed in the $Mg_{65}Cu_{22}B_3Gd_{10}$ and Mg-Cu-Ag-Gd alloys. Differential scanning calorimetry (DSC) thermograms of these alloys measured at a heating rate of 10 K/min are shown in Figure 4.19. The samples exhibit a clear glass transition, followed by a broad supercooled liquid region, and the exothermic reactions due to crystallization. Each DSC trace shows two or three exothermic peaks, corresponding to the multiple crystallizations of the initial amorphous structure. The glass transition temperatures T_g are marked by downward arrows on each of the DSC traces.

With the addition of boron or silver, the glass transition temperatures shift slightly. The crystallization temperatures T_x of the alloys are assigned to be the onset temperature of the first exothermic peak (upward arrows). In this study, the supercooled liquid range ΔT_x is seen to decrease from 60 K of the base alloy to around 41-51 K in the Ag- or B-additive alloys (Table 4.4).

The melting solidus temperature of the base alloy $Mg_{65}Cu_{25}Gd_{10}$, T_m, and the liquid temperature, T_l, are 679 and 726 K, respectively. With Ag addition, both T_m and T_l are seen to seen to decrease (Table 4.4). The liquidus temperature range, ΔT_l, becomes narrower in the Ag-additive alloys, implying that the Ag-additive alloy melt could be quenched into glass more easily, or corresponding to a higher GFA. In comparison, T_m of the B-containing Mg-Cu-Gd BMG decreases from 679 to 662 K, but T_l remains virtually unchanged.

This trend is the same if we use the reduced glass temperature, T_{rg} (= T_g/T_l), as the GFA parameter, which are 0.565, 0.586, 0.580, and 0.563 for $Mg_{65}Cu_{25}Gd_{10}$,

$Mg_{65}Cu_{22}Ag_{3}Gd_{10}$, $Mg_{65}Cu_{15}Ag_{10}Gd_{10}$, and $Mg_{65}Cu_{22}B_{3}Gd_{10}$, respectively (Table 4.4). This is probably why the addition of Ag was claimed to impose slightly positive effect on GFA of the Mg based BMGs [151, 140, 148, 152].

However, in terms of the widely accepted γ or the new γ_m parameters, the γ values are 0.414, 0.406, 0.408, and 0.404, and the γ_m values are 0.730, 0.702, 0.708, and 0.703 for $Mg_{65}Cu_{25}Gd_{10}$, $Mg_{65}Cu_{22}Ag_{3}Gd_{10}$, $Mg_{65}Cu_{15}Ag_{10}Gd_{10}$ and, $Mg_{65}Cu_{22}B_{3}Gd_{10}$, respectively, also compiled in Table 4.4. These two parameters both indicate that the Ag-additive alloys possess slightly inferior GFA, opposite to previous findings.

But the DSC results are only for the thermal properties of these alloys, the behavior under loading or forming needs to be explored by TMA. Coupled with the TMA results presented below, it is demonstrated in this study that the Ag or B addition in Mg-Cu-Gd might not have the promising character as we have expected.

4.4.2 Thermomechanical analysis

The temperature dependence of the compressive strain curves of the $Mg_{65}Cu_{25}Gd_{10}$, $Mg_{65}Cu_{22}Ag_{3}Gd_{10}$, $Mg_{65}Cu_{15}Ag_{10}Gd_{10}$, and $Mg_{65}Cu_{22}B_{3}Gd_{10}$ BMGs under TMA isochronal heating scan are shown in Figure 4.20. These typical TMA temperatures for these three alloys are also listed in Table 4.4. Note that the viscous flow temperature region under the loading in TMA, ΔT_m^* (= T_{finish} - T_{onset}), is 41, 33, 27, and 39 K for $Mg_{65}Cu_{25}Gd_{10}$, $Mg_{65}Cu_{22}Ag_{3}Gd_{10}$ $Mg_{65}Cu_{15}Ag_{10}Gd_{10}$, and $Mg_{65}Cu_{22}B_{3}Gd_{10}$, suggesting that the working window becomes gradually narrower with increasing Ag content.

In Figure 4.20, the true compressive strain (ε) is calculated by $\varepsilon = \ln(l/l_0)$, where l and l_0 are the specimen final and initial length (~ 8 mm), respectively. Generally, samples do not deform notably in the rigid glassy state until the temperature is above T_g.

In this region, sample continuously deforms with increasing temperature until the primary crystallization occurs. It is evident that the base alloy $Mg_{65}Cu_{25}Gd_{10}$, has a larger deformability with a 6.5% plastic strain, as compared to $Mg_{65}Cu_{22}Ag_3Gd_{10}$, $Mg_{65}Cu_{15}Ag_{10}Gd_{10}$, and $Mg_{65}Cu_{25}Gd_{10}$ amorphous samples which exhibit lower strains of 2.5%, 0.9%, and 1.4%, after the entire temperature scan.

4.4.3 Viscous flow behavior

The viscosity, η, is calculated by the Stefan's equation with the geometrical correction (Eq. 2-17) [113] of viscous flow, and the initial cross-sectional area is 12.56 mm^2. The viscosities as a function of temperature for the two alloys above the T_g are shown in Figure 4.21.

Viscosity

The viscosity trend as a function of temperature of the current Mg-Cu-(Ag, B)-Gd BMGs is consistent with those for other Mg, Zr and Au BMGs [10, 153, 114, 154] and the η_{min} values are indeed $\leq 10^8$ Pa·s within the supercooled liquid region. In the case of Mg-Cu-(Ag, B)-Gd BMGs, the η_{min} values, obtained at the same isochronal heating rate of 10 K/min, are 1.5 x 10^6, 2.6 x 10^6, 1.4 x 10^7, and 1.6 x 10^7 Pa·s for $Mg_{65}Cu_{25}Gd_{10}$, $Mg_{65}Cu_{22}Ag_3Gd_{10}$, $Mg_{65}Cu_{15}Ag_{10}Gd_{10}$, and and $Mg_{65}Cu_{22}B_3Gd_{10}$ alloys, respectively (Table 4.5). Judging from the increase of η_{min} from 1.5 x 10^6 to 1.6 x 10^7 Pa·s with the addition of Ag or B- content, it is for sure that the Ag or B addition would cause a negative effect for viscous flow to form over this supercooled temperature region.

Vogel-Fulcher-Tammann fitting and Angell's plot

All viscosity data calculated in the supercooled liquid can be described well with the Vogel-Fulcher-Tammann (VFT) equation [155]. The variations of viscosity of the four amorphous alloys with a VFT fitting as a function of the inverse of temperature (η-T^{-1}) above the T_g are shown in Figure 4.22(a). The functional trend is noted to be consistent with those for Zr- and Au-BMGs. The temperature at the viscosity of 10^{12} Pa·s, T_g^*, is noted to decrease with the Ag or B addition, as seen in Table 4.5.

In general, the strong glass formers, such as SiO_2, are one extreme, exhibiting a high fragility parameter D* (~100) and very low VFT temperature T_0, but the fragile glass formers like o-terphenyl, show a low fragility parameter D* (~5) and VFT temperature close to T_g^*. The T_g^* of the $Mg_{65}Cu_{22}B_3Gd_{10}$ alloy with copper replaced by boron increases negligibly from 393 to 395 K, but Mg-Cu-Gd alloys with copper replaced by silver decrease clearly from 393 to 380 K. The fragility parameter D* is found to increase from ~15 for the base alloy $Mg_{65}Cu_{25}Gd_{10}$ to about 16-20 for the Ag or B containing alloys. Meanwhile, the VFT temperature, T_0, is found to decrease from 260 K for the base alloy $Mg_{65}Cu_{25}Gd_{10}$ to 232-241 K for the Ag or B containing alloys, also listed in Table 4.5. Both the trends of D* and T_0 indicate that the viscosities of the current Mg based BMGs are noted to fall in the range between the strong and fragile glasses. Also, the $Mg_{65}Cu_{22}B_3Gd_{10}$ and $Mg_{65}Cu_{15}Ag_{10}Gd_{10}$ are relatively closer to the stronger glass state.

The value of T_0/T_g^* is a useful index expressing the difference between T_0 and T_g^*. Generally speaking, for a very strong glass, such as SiO_2, T_0/T_g^* is close to ~ 0, in contrast, it is close to ~1 for a very fragile glass such as o-terphenyl. For fragile BMGs, such as $Au_{77}Ge_{13.6}Si_{9.4}$[156] and $Pd_{79.5}Au_4Si_{18.5}$[157], their T_0/T_g^* values were reported to be close to ~0.85, and the log η(T) function shows a large deviation from linearity. In comparison, the T_0/T_g^* value is about ~0.63 for the commercial Zr based BMG Vit1 [114]. These results suggest that the T_0/T_g^* value is probably 0.5~0.9 for BMGs. In the case of the current $Mg_{65}Cu_{25}Gd_{10}$, the T_0/T_g^* value is about to 0.66. However, with increasing amount of silver or boron in replacing the copper atoms, they gradually decrease to ~0.604 (Table 4.5), that is, $Mg_{65}Cu_{15}Ag_{10}Gd_{10}$ is less fragile and is closer to a stronger glass. This effect is more apparent in boron containing system, since 3 at% B addition (T_0/T_g^*=0.610) produces a similar effect as the 10 at% Ag addition (T_0/T_g^*=0.604).

For the present alloys, the curves for Mg-Cu(B)-Gd BMGs diverge in T_g^*/T = 0.8 - 1.0 and the viscosity varies within 10^7 - 10^9 Pa·s at $T_g^*/T = 0.9$, as shown in Figure 4.22(b), namely the Angell plot [1] of Mg-Cu-(Ag, B)-Gd BMGs and their VFT equation fitting results. The data of $Au_{77}Ge_{13.6}Si_{9.4}$ and $Zr_{46.5}Ti_{8.25}Cu_{7.5}Ni_{10}Be_{27.5}$ from the literature [153, 10] are also included in Figure 4.22(b) for comparison. In other words, the variation of log η(T) is expected to be linear in the entire temperature range for strong glass, but for a fragile glass the curve should be convex.

4.4.4 Mechanical formability

It is generally recognized that, at a given heating rate, a BMG with lower η_{min} has a better and easier near-net shape capability with finer surface-printability [114]. The formability of metallic glasses in the supercooled liquid state can be expressed by a simple deformability parameter, d^*, [114] and another facile parameter ΔT^*_x [23], represents the supercooled temperature range (forming temperature range) of the BMGs under forming loads.

In this study, with α = 0.167 K/s, $d^*(\alpha)$ can be calculated from Eq. (2-25) using data from Figure 4.21, and they are tabulated in Table 4.5. The d^* values are calculated to be 5.83, 5.59, 4.85, and 4.80 for $Mg_{65}Cu_{25}Gd_{10}$, $Mg_{65}Cu_{22}Ag_3Gd_{10}$, $Mg_{65}Cu_{15}Ag_{10}Gd_{10}$, and $Mg_{65}Cu_{22}B_3Gd_{10}$, respectively. And the forming temperature range ΔT^*_x is calculated to decrease with the Ag or B addition from 0.193 down to 0.170. The value of ΔT^*_x and d^* for the Mg based BMGs are listed in Table 4.5. The decreasing trends of the deformability parameter d* and forming temperature range ΔT^*_x in the Ag-/B- containing Mg based BMGs again indicate the degraded properties in terms of superplastic micro-forming or nano-imprinting within the supercooled region. For the actual application condition under applied loading, the base alloy, $Mg_{65}Cu_{25}Gd_{10}$, exhibits a larger ΔT^*_x of 0.193 and a larger d^* of 4.05 than the Mg-based BMGs with addition of boron and silver atoms, suggesting that the base alloy $Mg_{65}Cu_{25}Gd_{10}$ is still a better alloy in terms of micro-forming and nano-imprinting.

However, the boron or silver containing alloy are previously demonstrated to possess a better room temperature hardness, as revealed by a higher crystallization activation energy [149, 158].

4.4.5 Deformation model

The reason for the degraded deformability of the Ag or B additive Mg-Cu-Gd metallic glasses during the supercooled state is explored further here. Spaepen [136] and Argon [137] developed a free-volume model, and the homogeneous deformation for BMGs can be described as Eq. (2-26). Consequently, we measured the coefficient of thermal expansion (CTE) of the current Mg-based BMGs and obtained a value of about 6.7×10^{-6} m/m·K, and made corrections on both the displacement and strain rate ($\dot{\gamma}$). With the corrected strain rate and the measured stress, the material constant $\gamma_0 v_0$ can be determined from the slope in Eq. (2-27). The thermal activation energy of a single STZ, ΔG^m, can be determined from the intercept of Eq. (2-28).

Silver additives

The material constant $\gamma_0 v_0$ can be determined from the slope in Eq. (2-27), as shown in Figure 4.23. The base metallic glass $Mg_{65}Cu_{25}Gd_{10}$ has a slope of about 7.53×10^{-8} Pa^{-1}, and the silver-additive amorphous alloys $Mg_{65}Cu_{22}Ag_3Gd_{10}$ and $Mg_{65}Cu_{15}Ag_{10}Gd_{10}$ have a slightly lower value of 7.40×10^{-8} Pa^{-1} and 7.08×10^{-8} Pa^{-1}, respectively. With the value of γ_0 is 0.125 [159], the volume of a basic flow unit during shear, v_0, is calculated to be 6.90, 6.78 and 6.49 nm^3 for $Mg_{65}Cu_{25}Gd_{10}$, $Mg_{65}Cu_{22}Ag_3Gd_{10}$ and $Mg_{65}Cu_{15}Ag_{10}Gd_{10}$, respectively. Therefore, adding the silver atoms appears to decrease slightly the size of flow unit.

Figure 4.24 for a representative strain rate of 4×10^{-4} s^{-1}. The extracted thermal activation energy, ΔG^m for $Mg_{65}Cu_{25}Gd_{10}$, $Mg_{65}Cu_{22}Ag_3Gd_{10}$ and $Mg_{65}Cu_{15}Ag_{10}Gd_{10}$ are 1.17, 0.83 and 1.61 eV, respectively, or corresponded to 112.89, 80.08, and 155.34 kJ/mol (1 eV = 96.487 kJ/mol). It should be noted that the extraction of the activation energy needs to use the extrapolation method to cover a wider temperature range, which might lead to higher uncertainty. The wider scattering of the extracted activation energy data makes it difficult to reach conclusive judgment. But it is likely that, with abundant Ag addition to 10 at%, the thermal activation energy of a single STZ during the viscous flow of $Mg_{65}Cu_{25}Gd_{10}$ would increase.

The Mg based amorphous alloys with the addition of Ag, the supercooled viscous temperature window for micro-forming would become narrower, the minimum viscosity level would be higher, and the deformability parameter becomes lower. In other words, with the consideration of micro-forming or nano-imprinting, the Ag additive Mg based BMGs are not as promising as the Ag-free alloys.

Boron additives

The material constant $\gamma_0 v_0$ can be determined from the slope in Eq. (2-27), as shown in Figure 4.25. A slope of the boron-added alloy $Mg_{65}Cu_{22}B_3Gd_{10}$ has a slightly lower value of 6.75×10^{-8} Pa^{-1}. Using $\gamma_0 = 0.125$ [159], the volume of a basic flow unit during shear, v_0, is calculated to be 6.90 nm^3 and 6.19 nm^3 for $Mg_{65}Cu_{25}Gd_{10}$ and $Mg_{65}Cu_{22}B_3Gd_{10}$, respectively. Therefore, it appears that the addition of small boron atoms can occupy some free volume, and thus decrease the size of flow unit. On the other hand, the thermal activation energy of a single STZ, ΔG^m, can be determined from the intercept of Eq. (2-28), as shown in Figure 4.26 for a representative strain rate of 4×10^{-4} s^{-1}. The extracted thermal activation energy ΔG^m for $Mg_{65}Cu_{25}Gd_{10}$ and $Mg_{65}Cu_{22}B_3Gd_{10}$ are 1.17 eV (112.89 kJ/mol) and 3.27 eV (315.51 kJ/mol), respectively. These values are of the same order of magnitude as those values estimated for Au-based (3.20 eV) [138] and Pd-based (9.03 eV) [160] BMGs. Here, higher activation energy in $Mg_{65}Cu_{22}B_3Gd_{10}$ than that in $Mg_{65}Cu_{25}Gd_{10}$ suggests that the replacement of Cu by 3 at% B atoms not only reduces the free volume and STZ size, but also make the viscous flow more difficult.

Based on the above analyses, it is demonstrated that the determination of the workability of a BMG within the supercooled liquid regime is not straightforward. Several parameters, including the viscosity level, the supercooled temperature range under various applied loads, the workability index, and the thermal stability under loading or forming, must be sought simultaneously. Mg based alloys, such as $Mg_{65}Cu_{25}Gd_{10}$, are attractive along this line owing to their low price (compared with Au-, Pd-, Pt-, or Zr-based BMGs), low glass transition temperature (around 150°C, and thus the lower forming temperature), sufficiently low viscosity, and adequate workability. With the addition of minor boron, many of the properties are changed to a different extent. Overall, if the surface hardness and wear resistance of the MEMS piece is of more concern, $Mg_{65}Cu_{22}B_3Gd_{10}$ might be a better choice. If the forming or imprinting practice is of more concern, $Mg_{65}Cu_{25}Gd_{10}$ appears to be a more promising alloy.

4.4.6 Combined effects of B and Ag addition

The thermal and thermomechanical properties of the $Mg_{65}Cu_{25-x}Ag_xGd_{10}$ (x=0, 3, 10 at.%) and $Mg_{65}Cu_{22}B_3Gd_{10}$ bulk metallic glasses are examined in the supercooled liquid region using DSC and TMA. The following combined effects are reached based on the current experimental and analytical results: (1) The addition of Ag or B into Mg-Cu-Gd would degrade slightly the glass forming ability in terms of the γ and γ_m parameters. (2) The supercooled viscous temperature windows (ΔT_x measured from DSC and ΔT_x^* measured from TMA), all show to be narrower with the addition of Ag or B, leading to the negative factor for forming practices. (3) The minimum viscosity η_{min} and the fragility parameter D* would both increase with increasing Ag addition, suggesting the stronger glass nature. As a consequence, the deformability parameter d* would also decrease accordingly, leading to another negative factor for the forming purpose. (4) The current results suggest that the Mg based BMGs are promising candidates for micro-forming or nano-imprinting over the supercooled viscous regime. But under the loading condition during forming, the Ag-/B- containing Mg BMGs are less promising as compared with the base $Mg_{65}Cu_{25}Gd_{10}$ alloy. (5) The addition of silver or boron into $Mg_{65}Cu_{25}Gd_{10}$ would increase the room temperature hardness and resistance against crystallization, based on hardness and DSC measurements. If the surface hardness and wear resistance of the MEMS piece is of more concern, $Mg_{65}Cu_{25-x}Ag_xGd_{10}$ (x=3, 10 at.%) and $Mg_{65}Cu_{22}B_3Gd_{10}$ might be a better choice over

$Mg_{65}Cu_{25}Gd_{10}$. However, if the forming or imprinting practice is of more concern, $Mg_{65}Cu_{25}Gd_{10}$ appears to be a more promising alloy.

Chapter 5 Summary

In the initial attempts of this study, some problems encountered during the experiment scheduler in this thesis such as the improper compositions, the specimens with many pores or nano-crystals, the over loaded applied stresses in the imprinting process, and the approximate errors of analyzer. However, numerous efforts are made to develop an easier judging of the workability, and repeatable imprinting process. The proper parameters for the thermomechanical properties and workability of the Mg-based BMGs, were finally found. The gathered dat are helpful for MEMS applications.

According to the results and discussions in the previous chapters, this thesis can be concluded as follow:

1. The $Mg_{58}Cu_{31}Y_{11}$ appears to be the most optimum composition of the Mg-Cu-Y systems, with the best glass forming ability and working temperature window for micro/nano forming partitions.

2. Below the semi-steady-state viscous flow temperature, T_{vs}, all effective viscosities of the $Mg_{58}Cu_{31}Y_{11}$ amorphous alloy decreases with increasing temperature, with the highest applied compressive stress giving the greatest value of effective viscosity. In addition, the onset temperature for the viscous flow, T_{onset}, and the finish temperature for the viscous flow, T_{finish}, both decrease with increasing applied stress.

3. A largest change in $\Delta L/P$ (displacement/applied stress) of about 20 μm/kPa was obtained in the vicinity of T_{finish} at a applied stress of 0.79 kPa.

4. Utilizing the viscous flow behavior of the Mg-Cu-Y metallic glass at temperatures slightly above their glass transition temperature, T_g, a new process of forming a micro-lens array is presented in this study. The α-step surface profiles of the original convex Ni-Co mold, imprinted concave $Mg_{58}Cu_{31}Y_{11}$ BMG, and the final imprinted convex PMMA are closely matched. The finite element simulation conforms the experimental observation.

5. In the Mg-Cu-Gd amorphous alloy, the addition of silver or boron into Mg-Cu-Gd would degrade slightly the glass forming ability. Also, the thermal stability with applied stress (ΔT_m^*) appears to be narrower with the addition of Ag or B, leading to the negative factor for forming practices. However, the B- or Ag-additive enhance the room temperature hardness, and thus should be more wear-resistant.

6. The Ag- or B-addition causes a negative effect for viscous flow over this supercooled temperature region, and the fragility parameter D* is also found to increase from ~15 for the base alloy $Mg_{65}Cu_{25}Gd_{10}$ to about 16-20 for the Ag or B containing alloys, suggesting the stronger glass nature.

7. The thermal activation energy, ΔG^m, are 113, 80, 155, and 316 kJ/mol for $Mg_{65}Cu_{25-x}Ag_xGd_{10}$ (x = 0, 3, 10 at.%) and $Mg_{65}Cu_{22}B_3Gd_{10}$. The higher activation energy (ΔG^m) of the Mg-Cu-Ag(B)-Gd BMGs than that of $Mg_{65}Cu_{25}Gd_{10}$ suggests that the replacement of Cu by Ag or B atoms not only reduces the free volume and STZ size, but also make the viscous flow more difficult.

8. The workability of a BMG within the supercooled liquid regime is not straightforward. Several parameters, including the viscosity level, the supercooled temperature range under various applied loads, the workability index, and the thermal stability under loading or forming, must be sought simultaneously.

References

[1] Angell CA. Science 1995;267:1924-1935.

[2] Angell CA, Poole PH, Shao J. Nuovo Cimento 1994;16:993-1025.

[3] Uhlmann DR, Hayes JF, Turnbull D. Phys. Chem. Glasses 1967;8:1-10.

[4] Angell CA, Sare JM, Sare EJ. J. Phys. Chem. 1978;82:2622-2629.

[5] Iben IET, Draunstein D, Doster W, Frauenfelder H, Hong MK, Johnson JB, Luck S, Ormos P, Schulte A, Steinbach PJ, Xie AH, Young RD. Phys. Rev. Lett. 1989;62:1916-1919.

[6] Klement W, Willens RH, Duwez P. Nature 1960;187:869-870.

[7] http://www.liquidmetal.com.

[8] Pryds NH. Mater. Sci. Eng. A 2004 375-377:186-193.

[9] Inoue A. Acta Mater. 2000;48:279-306.

[10] Chen HS, Turnbull D. J. Chem. Phys. 1968;48:2560-2571.

[11] Chen HS, Turnbull D. Acta Metall. 1969;17:1021-1031.

[12] Chen HS, Miller CE. Rev. Sci. Instrum. 1970;41:1237-1238.

[13] Chen HS. Acta Metall. 1974;22:1505-1512.

[14] Chen HS, Krause JT, Coleman E. J. Non-Cryst. Solids 1975;18:157-171.

[15] Drehman AJ, Greer AL. Acta Metall 1984;32:323-332.

[16] Kui HW, Greer AL, Turnbull D. Appl. Phys. Lett. 1984;45 615-616.

[17] Inoue A, Zhang T, Masumoto T. Mater. Trans. JIM 1990;31:425-428.

[18] Inoue A, Nakamura T, Nishiyama N, Masumoto T. Mater. Trans. JIM 1992;33:937-945.

[19] Inoue A, Zhang T, Nishiyama N, Ohba K, Masumoto T. Mater. Trans. JIM 1993;34:1234-1237.

[20] Peker A, Johnson WL. Appl. Phys. Lett. 1993;63:2343-2344.

[21] Lin XH, Johnson WL, Rhim WK. Mater. Trans. JIM 1997;38:473-477.

[22] Inoue A, Nishiyama N, Kimura H. Mater. Trans. JIM 1997;38:179-204.

[23] Ma H, Shi LL, Xu J, Li Y, Ma E. Appl. Phys. Lett. 2005;87:181915.

[24] Wang WH, Dong C, Shek CH. Mater. Sci. Eng. R 2005;44:45-89.

[25] Loffler JF. Intermetallics 2003;11:529-540.

[26] Chopra KL, *Thin Film Phenomena*, McGraw-Hill, New York, 1985.

[27] Hsieh PJ, PhD Thesis, *Nanocrystallization and Amorphization of Zr Base Alloys during Accumulative Roll Bonding*, National Sun Yat-Sen University, Kaohsiung, Taiwan, 2004.

[28] Liu FX, Liaw PK, Wang GY, Chiang CL, Smith DA, Rack PD, Chu JP, Buchanan RA. Intermetallics 2006;14:1014-1018.

[29] Gramt PS. Prog. Mater. Sci. 1995;39:497-545.

[30] Li B, Nordstrom N, Lavernia EJ. Mater. Sci. Eng. R 1997;A237:207-215.

[31] Liu R, Li J, Dong K, Zheng C, Liu H. Mater. Sci. Eng. R 2002;B94:141-148.

[32] Clement W, Willens RH, Duwez P. Nature (London) 1960;187:869-870.

[33] Ohring M, Haldipur A. Rev. Sci. Instrum. 1971;42:530-531.

[34] Pond R, Maddin R. Trans. Met. Soc. AIME 1969;245:2475-2476.

[35] El-Eskandarany MS, Inoue A. Metall. Mater. Trans. A 2002;33:135-143.

[36] Koch CC, Kavin OB, Mckamey CG, Scarbrough JO. Appl. Phys. Lett. 1983;43:1017-1091.

[37] Lee J, Zhou F, Chung KH, Kim NJ, Lavernia EJ. Metall. Mater. Trans. A 2001;32:3109-3115.

[38] Sagel A, Sieber H, Fecht H-J, Perepezko JH. Acta Mater. 1998;46:4233-4241.

[39] Saito Y, Utsunomiya U, Tsuji N, Sakai T. Acta Mater. 1999;47:579-583.

[40] Xing ZP, Kang SB, Kim HW. Metall. Mater. Trans. A 2002;33:1521-1530.

[41] Donald IW, Davies HA. J. Non-Cryst. Solids 1978;30:77-85.

[42] Hruby A. Czech. J. Phys. 1972;22:1187-1193.

[43] Mondal K, Murty BS. J. Non-Cryst. Solids 2005;351:1366-1371.

[44] Saad M, Poulain M. Mater. Sci. Forum 1987;19-20:11-18.

[45] Turnbull D. Contemp. Phys. 1969;10:473-488.

[46] Hung TH, Huang JC, Jang JSC, Lu SC. Mater. Trans. 2007;48:239-243.

[47] Lu ZP, Liu CT, Dong Y. J. Non-Cryst. Solids 2004;341:93-100.

[48] Senkov ON, Miracle DB. Mater. Res. Bull. 2001;36:2183-2198.

[49] Xiao X, Fang S, Wang G, Hua Q, Dong Y. J. Alloys Compd. 2004;376:145-148.

[50] Xiao X, Fang S, Xia L, Li WH, Hua Q, Dong Y. J. Alloys Compd. 2003;351:324-328.

[51] Yan ZJ, Li JF, He SR, Zhou YH. Mater. Res. Bull. 2003;38:681-689.

[52] Egami T. J. Non-Cryst. Solids 1996;205-207:575-582.

[53] Egami T. Mater. Sci. Eng. 1997;A226-228:261-267.

[54] Egami T, Waseda Y. J. Non-Cryst. Solids 1984;64:113-134.

[55] Miracle DB, Senkov ON. J. Non-Cryst. Solids 2004;319:174-191.

[56] Senkov ON, Miracle DB, Mullens HM. J. Appl. Phys. 2005;97:103502.

[57] Azad S, Mandal A, Mandal RK. Mater. Sci. Eng. A, 2007;458:348-354.

[58] Chen W, Wang Y, Qiang J, Dong C. Acta Mater. 2003;51:1899-1907.

[59] Iqbal M, Sun WS, Zhang HF, Akhter JI, Hu ZQ. Mater. Sci. Eng. A, 2007;447:167-173.

[60] Wang Q, Wang YM, Qiang JB, Zhang XF, Shek CH, Dong C. Intermetallics 2004;12:1229-1232.

[61] Wang YM, Shek CH, Qiang JB, Wong CH, Chen WR, Dong C. Scripta Mater. 2003;48:1525-1529.

[62] Wang YM, Xu WP, Qiang JB, Wong CH, Shek CH, Dong C. Mater. Sci. Eng. A, 2004;375-377:411-416.

[63] Cheng YT, MS Thesis, *Amorphization and Nanocrystallization Behavior in Mg-Cu-Y Alloy by Adding Boron*, National Sun Yat-Sen University, Kaohsiung, Taiwan, 2005.

[64] Inoue A. Acta Mater. 2000;48:279-306.

[65] Lu ZP, Tan H, Li Y, Ng SC. Scripta Mater. 2000;42:667-673.

[66] Murty BS, Hono K. Mater. Trans. JIM 2000;41:1538-1544.

[67] Shen TD, Schwarz RB. Appl. Phys. Lett. 1999;75:49-51.

[68] Waniuk TA, Schroers J, Johnson WL. Appl. Phys. Lett. 2001;78:1213-1215.

[69] Inoue A, Zhang W, Zhang T, Kurosaka K. Acta Mater. 2001;49:2645-2652.

[70] Inoue A, Zhang W, Zhang T, Kurosaka K. J. Mater. Res. 2001;16:2836-2844.

[71] Lu ZP, Liu CT. Acta Mater. 2002;50:3501-3512.

[72] Lu ZP, Liu CT. Intermetallics 2004;12:1035-1043.

[73] Lu ZP, Liu CT. Phys. Rev. Lett. 2003;91:115505.

[74] Du XH, Huang JC, Liu CT, Lu ZP. J. Appl. Phys. 2007;101:086108.

[75] Inoue A. Mater. Sci. Eng. A 2001;304-306:1-10.

[76] Zhang T, Inoue A. Mater. Trans. JIM 1998;39:857-862.

[77] Inoue A, Hashimoto K, *Amorphous and Nanocrystalline Materials: Preparation, Properties, and Applications*, Springer-Verlag, Berlin and Heidelberg, 2001.

[78] Yokoyama Y, Nishiyama N, Fukaura K, Sunada H, Inoue A. Mater. Trans. JIM 1999;40:696-699.

[79] Yoshizawa Y, Oguma S, Yamauchi K. J. Appl. Phys. 1988;64:6044-6046.

[80] Shen TD, Schwarz RB. Acta Mater. 2001;49:837-847.

[81] Asami K, Inoue A. Mater. Sci. Eng. A 2004;375-377:235-239.

[82] Shoji T, Inoue A. J. Alloys Compd. 1999;292:275-280.

[83] Isogai K, Shoji T, Kimura HM, Inoue A. Mater. Trans. JIM 2000;41:1486-1486.

[84] Telford M. Mater. Today 2004;7:36-43.

[85] Chang YC, Wu TT, Chen MF, Lee CJ, Huang JC, Pan CT. Mater. Sci. Eng. A 2008;in press.

[86] Pan CT, Wu TT, Chang YC, Huang JC. J. Micromech. Microeng. 2008;18:025010-025021.

[87] Pan CT, Wu TT, Chen MF, Chang YC, Lee CJ, Huang JC. Sens. Actuat. A 2008;141:422-431.

[88] Schroers J, Pham Q, Desai A. J. Micro. Elec. Sys. 2007;16:240-247.

[89] Chen HS. J Non-Cryst Solids 1978;27:257-263.

[90] Maddin R, Masumoto T. Mater. Sci. Eng. 1972;9:153-161.

[91] Saitoh K, Tsuda K, Tanaka M, Tsai AP, Inoue A, Masumoto T. Mater. Sci. Eng. A 1994;181-182:805-810.

[92] Masumoto T, Maddin R. Acta Metall. 1971;19:725-741.

[93] Spaepen F, Taub AI, *Amorphous Metallic Alloys, ed.*, Butterworths, London, 1983.

[94] Inoue A, Zhang T, Masumoto T. Mater. Trans. JIM 1990;31:425-428.

[95] Inoue A. Mater. Trans. JIM 1995;36:866-875.

[96] Yuan G, Inoue A. J. Alloys Compd. 2005;387:134-138.

[97] Inoue A, Kato A, Zhang T, Kim SG, Masumoto T. Mater. Trans. JIM 1991;32:609-616.

[98] Chen HM, Chang YC, Hung TH, Du XH, Huang JC, Jang JSC, Liaw PK. Mater. Trans. JIM 2007;48:1802-1805.

[99] Reed-Hill RE, Abbaschian R, *Physical Metallurgy Principles*, PWS, Boston,

USA, 1994.

[100] Inoue A, Takeuchi A, Zhang T. Metall. Mater. Trans. A 1998;29:1779-1793.

[101] Takeuchi A, Inoue A. Mater. Trans. 2000;41:1372-1378.

[102] Fulcher GS. Bull. J. Amer. Cerm. Soc. 1925;8:339-355.

[103] Masuhr A, Waniuk TA, Busch R, Johnson WL. Phys. Rev. Lett. 1999;82:2290-2293.

[104] Shaw T, Way C, Busch R. Mater. Res. Soc. Symp. Proc. 2004;806:215-220.

[105] Wilde G, Görler GP, Willnecker R, Dietz G. Appl. Phys. Lett. 1994;65:397-399.

[106] Busch R, Liu W, Johnson WL. J. Appl. Phys. 1998;83:4134-4141.

[107] Busch R, Kim YJ, Johnson WL. J. Appl. Phys. 1995;77:4039-4043.

[108] Glade SC, Busch R, Lee DS, Johnson WL. J. Appl. Phys. 2000;87:7242-7248.

[109] Porter DA, Esterling KE, *Phase Transformations in Metals and Alloys*, Chapman and Hall, 1997.

[110] Ediger MD, Angell CA, Nagel SR. J. Phys. Chem. 1996;100:13200-13212.

[111] Xu D, Lohwongwatana B, Duan G, Johnson WL, Garland C. Acta Mater. 2004;52:2621-2624.

[112] Busch R. J. Metals. 2000;52:39-42.

[113] Stefan MJ. Math Nat. Klasse 1874;69:713-735.

[114] Kato H, Wade T, Hasegawa M, Saida J, Inoue A, Chen HS. Scripta Mater. 2006;54:2023-2027.

[115] Lida T, Guuthrie RIL, *The Physical Properties of Liquid Metals*, Clarendon, Oxford, 1998.

[116] Bakke E, Busch R, Johnson WL. Appl. Phys. Lett. 1995;67:3260-3262.

[117] Diennes GJ, Klemm HF. J. Appl. Phys. 1946;17:458-471.

[118] Masuhr A, Busch R, Johnson WL. Mater. Sci. Forum 1998;269-272:779-784.

[119] Kelton KF. Solid State Phys. 1991;45:75-90.

[120] Volkert CA, Spaepen F. Acta Metall. 1989;37:1355-1362.

[121] Russew K, Stojanova L, Sommer F. Int. J. Rapid Solidification 1995;8:267-279.

[122] Myung WN, Park KH, Jang DH, Battezzati L, Zhang T, Inoue A, Masumoto T. Mater. Sci. Eng. A 1997;226-228:406-409.

[123] Myung WN, Bae HY, Hwang IS, Kim HG, Nishiyama N, Inoue A. Mater. Sci. Eng. A 2001;304-306:687-690.

[124] Myung WN, Ryu SP, Hwang IS, Kim HG, Zhang T, Inoue A, Greer AL. Mater. Sci. Eng. A 2001;304-306:691-695.

[125] Wanuik TA, Busch R, Masuhr A, Johnson WL. Acta Mater. 1998;46:5229-5236.

[126] Russew K, Stojanova L. Mater. Lett. 1993;17:199-204.

[127] http://www.anasys.co.uk/library/tma1.htm.

[128] Scholorke N, Weiss B, Eckert J, Schutz L. Nanostruct. Mater. 1999;12:127-130.

[129] Myung WN, Hwang IS, Kim HG. J. Koran Phys. Soc. 2002;40:476-479.

[130] Inoue A, Kawamura Y, Shibata T, Sasamori K. Mater. Trans. JIM 1996;37:1337-1341.

[131] Jeong HW, Hata S, Shimokohbe A. Microelec. Mech. Sys. 2003;12:42-52.

[132] Kawamura Y, Shibata T, Inoue A, Masumoto T. Appl. Phys. Lett. 1996;69:1208-1210.

[133] Inoue A, Masumoto T. J. Non-Cryst. Solids 1993;156-158:473-480.

[134] Inoue A, Kawamura Y, Shibata T, Sasamori K. Mater. Trans. JIM 1996;37:1337-1341.

[135] Nishiyama N, Inoue A. Mater. Trans. JIM 1999;40:64-71.

[136] Spaepen F. Acta Metall. 1977;25:407-415.

[137] Argon AS. Acta Metall. 1979;27:47-58.

[138] Yang B, Wadsworth J, Nieh TG. Appl. Phys. Lett. 2007;90:061911.

[139] Park ES, Kang HG, Kim WT, Kim DH. J. Non-Cryst. Solids 2001;279:154-160.

[140] Park ES, Lee JY, Kim DH. J. Mater. Res. 2005;20:2379-2385.

[141] Brandes EA, Brook GB, *Smithells Metals Reference Book, 7th ed.*, Butterworth-Heinemann, Oxford, U.K., 1992.

[142] Miedema AR, de Boer FR, Boom R. Calphad 1977;1:341-359.

[143] Hung TH, MS Thesis, *Study of Thermal Properties in Zr-Al-Cu-Ni Amorphous Alloy by Adding Boron and Silicon*, National Sun Yat-Sen University, Kaohsiung, Taiwan, 2004.

[144] Nix WD, Gao H. J. Mech. Phys. Solids 1998;46:411-425.

[145] Swadener JG, George EP, Pharr GM. J. Mech. Phys. Solids 2002;50:681-694.

[146] Zheng Q, Xu J, Ma E. J. Appl. Phys. 2007;102:113519.

[147] Myung WN, Bae HY, Hwang IS, Kim HG, Nishiyama N, Inoue A. Mater. Sci. Eng. A 2001;304-306:687.

[148] Chang LJ, Jang JSC, Yang BC, Huang JC. J. Alloys Compd. 2007;434-435:221-224.

[149] Cheng YT, Hung TH, Huang JC, Hsieh PJ, Jang JSC. Mater. Sci. Eng. A 2007;A449-451:501-505.

[150] Cheng YT, Hung TH, Huang JC, Jang JSC, Tsao CYA, Lee PY. Intermetallic 2006;14:866-870.

[151] Inoue A, Nakamura T, Nishiyama N, Masumoto T. Mater. Trans. JIM 1992;33:937-945.

[152] Inoue A, Zhang T, Nishiyama N, Ohba K, Masumoto T. Mater. Trans. JIM

1993;34:1234-1237.

[153] Busch R, Bakke E, Johnson WL. Acta Mater. 1998;46:4725-4732.

[154] Chang YC, Huang JC, Cheng YT, Lee CJ, Du XH, Nieh TG. J. Appl. Phys. 2008;103:103521.

[155] Scherer GW. J. Am. Ceram. Soc. 1992;75:1060-1061.

[156] Chen HS, Turnbull D. J. Chem. Phys. 1968;48:2560-2571.

[157] Chen HS, Goldstein M. J. Appl. Phys. 1972;43:1642-1648.

[158] Mahadevan S, Giridhar A, Singh AK. J. Non-Cryst. Solids 1986;88:11-34.

[159] Argon AS, Shi LT. Acta Metall. 1983;31:499-507.

[160] Spaepen F. Scripta Mater. 2006;54:363-367.

Table 1.1 The features and applications of metallic glasses [9].

Fundamental Characteristics	Application Fields
High Strength	Machinery Structural Materials
High Hardness	Optical Precision Materials
High Fracture Toughness	Die Materials
High Impact Fracture Energy	Tool Materials
High Fatigue Strength	Cutting Materials
High Elastic Energy	Electrode Materials
High Corrosion Resistance	Corrosion Resistance Materials
High Wear Resistance	Hydrogen Storage Materials
High Viscous Flowability	Ornamental Materials
Good Soft Magnetism	Writing Appliance Materials
High Frequency Permeability	Sporting Good Materials
High Magnetostriction	Bonding Materials
Efficient Electrode (Chlorine Gas)	Soft Magnetic Materials
High Reflection Ratio	Composite Materials
High Hydrogen Storage	High Magnetostrictive Materials

Table 1.2 Bulk metallic glasses and their developed year [24].

Nonferrous metal BMG system	Years	Ferrous metal base BMG system	Years
Pd–Cu–Si	1974	Fe–(Nb,Mo)–(Al,Ga)–(P,C,B,Si,Ge)	1995
Pt–Ni–P	1975	Pd–(Cu,Fe)–Ni–P	1996
Au–Si–Ge	1975	Fe–(Zr,Hf,Nb)–B	1996
Pd–Ni–P	1982	Co–Fe–(Zr,Hf,Nb)–B	1996
Mg–Ln–Cu (Ln = lanthanide metal)	1988	Zr–Nb–Cu–Fe–Be	2000
Ln–Al–TM (TM = group transition	1989	Fe–Mn–Mo–Cr–C–B	2002
Zr–Ti–Al–TM	1990		
Ti–Zr–TM	1993		
Zr–Ti–Cu–Ni–Be	1993		
Nd(Pr)–Al–Fe–Co	1994		
Zr–(Nb,Pd)–Al–TM	1995		
Cu–Zr–Ni–Ti	1995		
Co–(Al,Ga)–(P,B,Si)	1996		
Ni–(Zr,Hf,Nb)–(Cr,Mo)–B	1996		
Ti–Ni–Cu–Sn	1998		
La–Al–Ni–Cu–Co	1998		
Ni–Nb	1999		
Ni–(Nb,Cr,Mo)–(P,B)	1999		
Zr-based glassy composites	1999		
Ni–Nb–(Sn,Ti)	2003		
Pr(Nd)–(Cu,Ni)–Al	2003		

Table 1.3 Summary of ΔT_x, T_{rg}, γ, R_c and Z_c for typical BMGs [71].

Metallic glass systems	T_x-T_g	T_g/T_l	$T_x/(T_g+T_l)$	R_c(K/s)	Z_c(mm)
$Mg_{80}Ni_{10}Nd_1$	16.3	0.517	0.353	1251.4	0.6
$Mg_{75}Ni_{15}Nd_{10}$	20.4	0.57	0.379	46.1	2.8
$Mg_{70}Ni_{15}Nd_{15}$	22.3	0.553	0.373	178.2	1.5
$Mg_{65}Ni_{20}Nd_{15}$	42.1	0.571	0.397	30	3.5
$Mg_{65}Ni_{25}Nd_{10}$	54.9	0.551	0.401	50	7
$Zr_{66}Al_8Ni_{26}$	35.6	0.537	0.368	66.6	
$Zr_{66}Al_8Cu_7Ni_{19}$	58.4	0.552	0.387	22.7	
$Zr_{66}Al_8Cu_{12}Ni_{14}$	77.4	0.559	0.401	9.8	
$Zr_{66}Al_9Cu_{16}Ni1_9$	79.5	0.561	0.403	4.1	
$Zr_{65}Al_{7.5}Cu_{17.5}Ni_{10}$	79.1	0.562	0.403	1.5	16
$Zr_{57}Ti_5Al_{10}Cu_{20}Ni_8$	43.3	0.591	0.395	10	10
$Zr_{38.5}Ti_{16.5}Ni_{9.75}Cu_{15.25}Be_{20}$	48	0.628	0.415	1.4	
$Zr_{39.88}Ti_{15.12}Ni_{9.98}Cu_{13.77}Be_{21.25}$	57	0.625	0.42	1.4	
$Zr_{41.2}Ti_{13.8}Cu_{12.5}Ni_{10}Be_{22.5}$	49	0.626	0.415	1.4	50
$Zr_{42.63}Ti_{12.37}Cu_{11.25}Ni_{10}Be_{23.75}$	89	0.589	0.424	5	
$Zr_{44}Ti_{11}Cu_{10}Ni_{10}Be_{25}$	114	0.518	0.404	12.5	
$Zr_{45.38}Ti_{9.62}Cu_{8.75}Ni_{10}Be_{26.25}$	117	0.503	0.397	17.5	
$Zr_{46.25}Ti_{8.25}Cu_{7.5}Ni_{10}Be_{27.5}$	105	0.525	0.402	28	
$La_{55}A_{l25}Ni_{20}$	64.3	0.521	0.388	67.5	3
$La_{55}Al_{25}Ni_{15}Cu_5$	67.6	0.526	0.394	34.5	
$La_{55}Al_{25}Ni_{10}Cu_{10}$	79.8	0.56	0.42	22.5	5
$La_{55}Al_{25}Ni_5Cu_{15}$	60.9	0.523	0.389	35.9	
$La_{55}Al_{25}Cu_{20}$	38.9	0.509	0.366	72.3	3
$La_{55}Al_{25}Ni_5Cu_{10}Co_5$	76.6	0.566	0.421	18.8	9
$La_{66}Al_{14}Cu_{20}$	54	0.54	0.399	37.5	2
$Pd_{40}Cu_{30}Ni_{10}P_{20}$	78.9	0.69	0.464	0.1	72
$Pd_{81.5}Cu_2Si_{16.5}$	37	0.577	0.387	2	
$Pd_{79.5}Cu_4Si_{16.5}$	40	0.585	0.392	500	0.75
$Pd_{77.5}Cu_6Si_{16.5}$	41	0.602	0.4	100	1.5
$Pd_{77}Cu_6Si_{17}$	44	0.569	0.388	125	2
$Pd_{73.5}Cu_{10}Si_{16.5}$	40	0.568	0.385	2	
$Pd_{71.5}Cu_{12}Si_{16.5}$	28	0.565	0.377	2	
$Pd_{40}Ni_{40}P_{20}$	63	0.585	0.409	0.167	25
$Nd_{60}Al_{15}Ni_{10}Cu_{10}Fe_5$	45	0.552	0.393	5	
$Nd_{61}Al_{11}Ni_8Co_5Cu_{15}$	24	0.598	0.394	6	
$Cu_{60}Zr_{30}Ti_{10}$	50	0.619	0.409	4	
$Cu_{54}Zr_{27}Ti_9Be_{10}$	42	0.637	0.412	5	
$Ti_{34}Zr_{11}Cu_{47}Ni_8$	28.8	0.597	0.389	100	4.5
$Ti_{50}Ni_{24}Cu_{20}B_1Si_2Sn_3$	74	0.554	0.393	1	

Table 1.4 The classification of amorphous alloy systems [24].

I	ETM(or Ln) + Al + LTM	Zr-Al-Ni、Zr-Al-Cu、Zr-Al-Ni-Cu、Zr-Ti-Al-Ni-Cu、Zr-Nb-Al-Ni-Ln、Zr-Ga-Ni
		Ln-Al-Ni、Ln-Al-Cu、Ln-Al-Ni-Cu、Ln-Ga-Ni、Ln-Ga-Cu
II	LTM + ETM + Metalloid	Fe-Zr-B、Fe-Hf-b、Fe-Zr-Hf-B、Fe-Co-Ln-B、Co-Zr-Nb-B
III	LTM(Fe) + Al or Ga + Metalloid	Fe-(Al, Ga)-Metalloid
IV	Mg + Ln +LTM	Mg-Ln-Ni、Mg-Ln-Cu
	TM(Zr or Ti) + Be + LTM	Zr-Ti-Be-Ni-Cu
V	LTM + Metalloid	Pd-Ni-P、Pd-Cu-Ni-P、Pt-Ni-p

ETM = IVB~VIB Group Transition Metal.

LTM = VIIB~VIIIB Group Transition Metal.

Table 2.1 Binary amorphous systems and mixing enthalpy values calculated based on Miedema's macroscopic model [101].

	Mg	**Cu**	**Y**	**Gd**	**Ag**	**B**
Mg		-3	-6		-10	
Cu	-3		-22	-22	2	0
Y	-6	-22			-29	-50
Gd		-22				-50
Ag	-10	2	-29			
B		0	-50	-50		

Table 2.2 The density for various Mg-Cu-Y-B system combinations [63].

Composition	**Theoretical density (Mg/m^3)**	**True density (Mg/m^3)**
$Mg_{65}Cu_{25}Y_{10}$	3.82	3.09
$Mg_{65}Cu_{24}Y_{10}B_1$	3.82	--
$Mg_{65}Cu_{22}Y_{10}B_3$	3.62	3.46
$Mg_{65}Cu_{20}Y_{10}B_5$	3.49	3.24
$Mg_{65}Cu_{15}Y_{10}B_{10}$	3.16	--
$Mg_{65}Cu_{25}Y_7B_3$	3.76	3.81
$Mg_{65}Cu_{25}Y_5B_5$	3.71	3.74
$Mg_{65}Cu_{25}B_{10}$	3.61	--

Pure elements: * Mg: 1.74 Mg/m^3; Cu: 8.96 Mg/m^3; Y: 4.48 Mg/m^3; B: 2.35 Mg/m^3

Table 2.3 Thermal properties and GFA index for the Mg-Cu-Y-B glassy alloys [63].

Compositions	T_g (K)	T_x (K)	ΔT_x (K)	T_m (K)	T_l (K)	γ
$Mg_{65}Cu_{25}Y_{10}$	410	468	58	728	760	0.40
$Mg_{65}Cu_{24}Y_{10}B_1$	410	476	66	715	738	0.42
$Mg_{65}Cu_{22}Y_{10}B_3$	420	470	50	712	736	0.41
$Mg_{65}Cu_{20}Y_{10}B_5$	420	465	45	---	---	---
$Mg_{65}Cu_{15}Y_{10}B_{10}$	420	457	37	---	---	---
$Mg_{65}Cu_{25}Y_7B_3$	408	430	22	---	---	---
$Mg_{65}Cu_{25}Y_5B_5$	Not amorphous alloy					

Table 2.4 Thermal analysis and maximum diameter for fully amorphous phase formation (D_{max}) for Mg-Cu-(Ag)-Y(Gd) alloys [139, 140].

Compositions	**T_g (K)**	**T_x (K)**	**ΔT_x (K)**	**T_m (K)**	**T_l (K)**	γ	**D_{max} (mm)**
$Mg_{65}Cu_{25}Y_{10}$	426	494	68	731	750		4
$Mg_{65}Cu_{15}Ag_{10}Y_{10}$	430	470	40	675	707		6
$Mg_{65}Ag_{25}Y_{10}$	436	460	24	750	725		--
$Mg_{65}Cu_{25}Gd_{10}$	423	484	61	679	740	0.416	8
$Mg_{65}Cu_{20}Ag_5Gd_{10}$	427	465	38	673	695	0.414	11
$Mg_{65}Cu_{15}Ag_{10}Gd_{10}$	416	459	43	675	691	0.415	7.5
$Mg_{65}Cu_{10}Ag_{15}Gd_{10}$	461	461	--	673	701	--	3
$Mg_{65}Cu_5Ag_{20}Gd_{10}$	467.5	467.5	--	690	709	--	0.5
$Mg_{65}Ag_{25}Gd_{10}$	475	475	--	716	738	--	0.1

Table 3.1 The compositions of the metallic glasses in this research.

Composition	**Mg**	**Cu**	**Y**	**Gd**	**B**	**Ag**
	at%	**at%**	**at%**	**at%**	**at%**	**at%**
$\mathbf{Mg_{67}Cu_{25}Y_8}$	67	25	8			
$\mathbf{Mg_{65}Cu_{25}Y_{10}}$	65	25	10			
$\mathbf{Mg_{58}Cu_{31}Y_{11}}$	58	31	11			
$\mathbf{Mg_{65}Cu_{25}Gd_{10}}$	65	25		10		
$\mathbf{Mg_{65}Cu_{22}B_3Gd_{10}}$	65	22		10	3	
$\mathbf{Mg_{65}Cu_{22}Ag_3Gd_{10}}$	65	22		10		3
$\mathbf{Mg_{65}Cu_{15}Ag_{10}Gd_{10}}$	65	15		10		10

Table 4.1 Summary of the thermal properties of the $Mg_{67}Cu_{25}Y_8$, $Mg_{65}Cu_{25}Y_{10}$ and $Mg_{58}Y_{31}Gd_{11}$ metallic glass ribbons, at a heating rate of 20 K/min

Compositions	**T_g (K)**	**T_x (K)**	**ΔT_x (K)**	**T_m (K)**	**T_l (K)**	**ΔT_l (K)**	γ	γ_m
$Mg_{67}Cu_{25}Y_8$	407	440	33	708	770	62	0.374	0.614
$Mg_{65}Cu_{25}Y_{10}$	417	465	48	709	748	39	0.400	0.686
$Mg_{58}Cu_{31}Y_{11}$	418	471	53	716	752	36	0.403	0.697

Table 4.2 The micro/nano- hardness of the $Mg_{67}Cu_{25}Y_8$, $Mg_{65}Cu_{25}Y_{10}$ and $Mg_{58}Y_{31}Gd_{11}$ metallic glass ribbons.

Compositions	**Micro-hardness**		**Nano-hardness**	
	GPa	**H_v**	**GPa**	**H_v**
$Mg_{67}Cu_{25}Y_8$	2.12 ± 0.03	216 ± 3	2.91 ± 0.52	270 ± 48
$Mg_{65}Cu_{25}Y_{10}$	2.16 ± 0.04	220 ± 4	2.93 ± 0.37	272 ± 34
$Mg_{58}Cu_{31}Y_{11}$	2.46 ± 0.03	252 ± 3	3.34 ± 0.41	310 ± 38

$$H_v = \frac{F}{A} \approx \frac{1.854F}{d^2}$$

1 Hv = 9.807 MPa

Table 4.3 Viscous flow behavior of the $Mg_{58}Cu_{31}Y_{11}$ BMGs obtained from TMA at a heating rate of 10 K/min.

Applied stress (kPa)	**ΔL_{max} (μm)**	**$\Delta L_{max}/\Delta L_0$ (%)**	**T_{onset} (K)**	**T_{vs} (K)**	**T_{finish} (K)**
0.79	60.9	1.52	438	465	477
2.38	162.6	4.07	432	463	474
7.08	265.3	6.63	427	461	472
117.83	748.6	18.72	423	460	471
318.52	923.3	23.08	418	460	469

Table 4.4 Summary of the thermal and thermomechanical properties of the Mg-Cu-(Ag, B)-Gd amorphous samples, measured by DSC and TMA, at a heating rate of 10 K/min.

Alloy	**DSC analysis**					
	T_g (K)	**T_x (K)**	**ΔT_x (K)**	**T_m (K)**	**T_l (K)**	**ΔT_l (K)**
$Mg_{65}Cu_{25}Gd_{10}$	410	470	60	679	726	47
$Mg_{65}Cu_{22}Ag_3Gd_{10}$	413	454	41	663	705	42
$Mg_{65}Cu_{15}Ag_{10}Gd_{10}$	407	452	45	664	702	38
$Mg_{65}Cu_{22}B_3Gd_{10}$	409	460	51	662	727	65

Alloy	**GFA parameters**			**TMA analysis**		
	T_{rg}	γ	γ_m	**T_{onset} (K)**	**T_{vs} (K)**	**T_{finish} (K)**
$Mg_{65}Cu_{25}Gd_{10}$	0.565	0.414	0.730	428	463	469
$Mg_{65}Cu_{22}Ag_3Gd_{10}$	0.586	0.406	0.702	419	449	452
$Mg_{65}Cu_{15}Ag_{10}Gd_{10}$	0.580	0.408	0.708	425	457	462
$Mg_{65}Cu_{22}B_3Gd_{10}$	0.563	0.405	0.703	423	450	462

Table 4.5 Summary of the fragility and viscous deformation related parameters of the Mg-Cu-(Ag, B)-Gd BMGs.

Alloy	**T_g^* (K)**	**η_{min} (Pa·s)**	**D^***	**T_0 (K)**	**T_0/T_g^***
$Mg_{65}Cu_{25}Gd_{10}$	393	1.5×10^6	~ 15	260	0.662
$Mg_{65}Cu_{22}Ag_3Gd_{10}$	380	2.6×10^6	~ 16	241	0.634
$Mg_{65}Cu_{15}Ag_{10}Gd_{10}$	384	1.4×10^7	~ 20	232	0.604
$Mg_{65}Cu_{22}B_3Gd_{10}$	395	1.6×10^7	~18	241	0.610

Alloy	**d^***	**ΔT^*_x**	**v_0 (nm^3)**	**ΔG^m (kJ/mol)**
$Mg_{65}Cu_{25}Gd_{10}$	5.83	0.193	6.90	112.89
$Mg_{65}Cu_{22}Ag_3Gd_{10}$	5.59	0.189	6.78	80.08
$Mg_{65}Cu_{15}Ag_{10}Gd_{10}$	4.85	0.177	6.49	155.34
$Mg_{65}Cu_{22}B_3Gd_{10}$	4.80	0.170	6.19	315.51

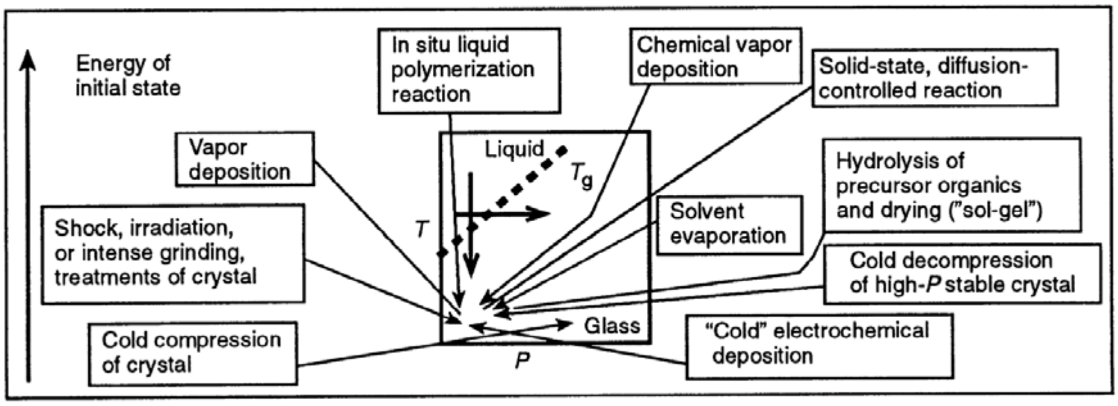

Figure 1.1 Illustrator of different parts to form the glassy state, roughly indicating the energies of the initial states relative to the final glassy states. The route of crystal compression below T_g may yield glasses that are thermodynamically distinct from those obtained by the other routes which may transform to them by way of non-equilibrium first-order transitions [1].

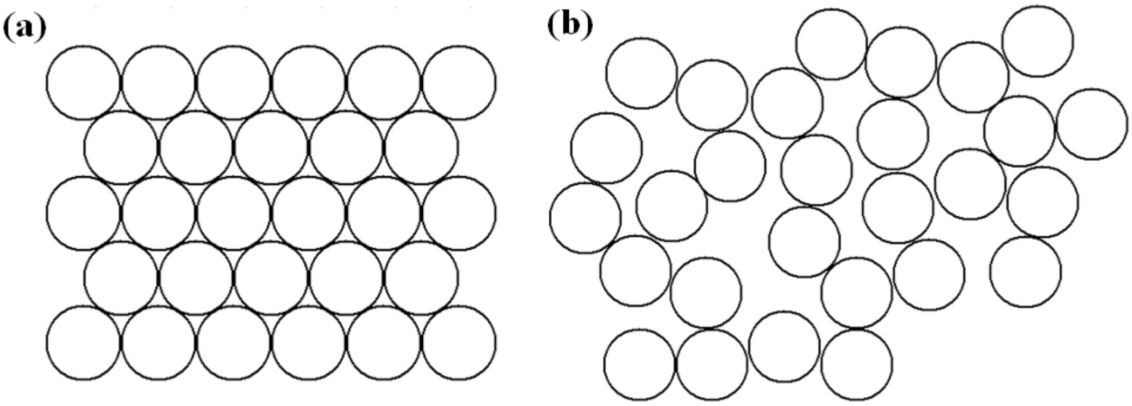

Figure 1.2 The arrangement of atoms in (a) crystalline and (b) amorphous states.

Figure 1.3 The surface of a metallic glass [84].

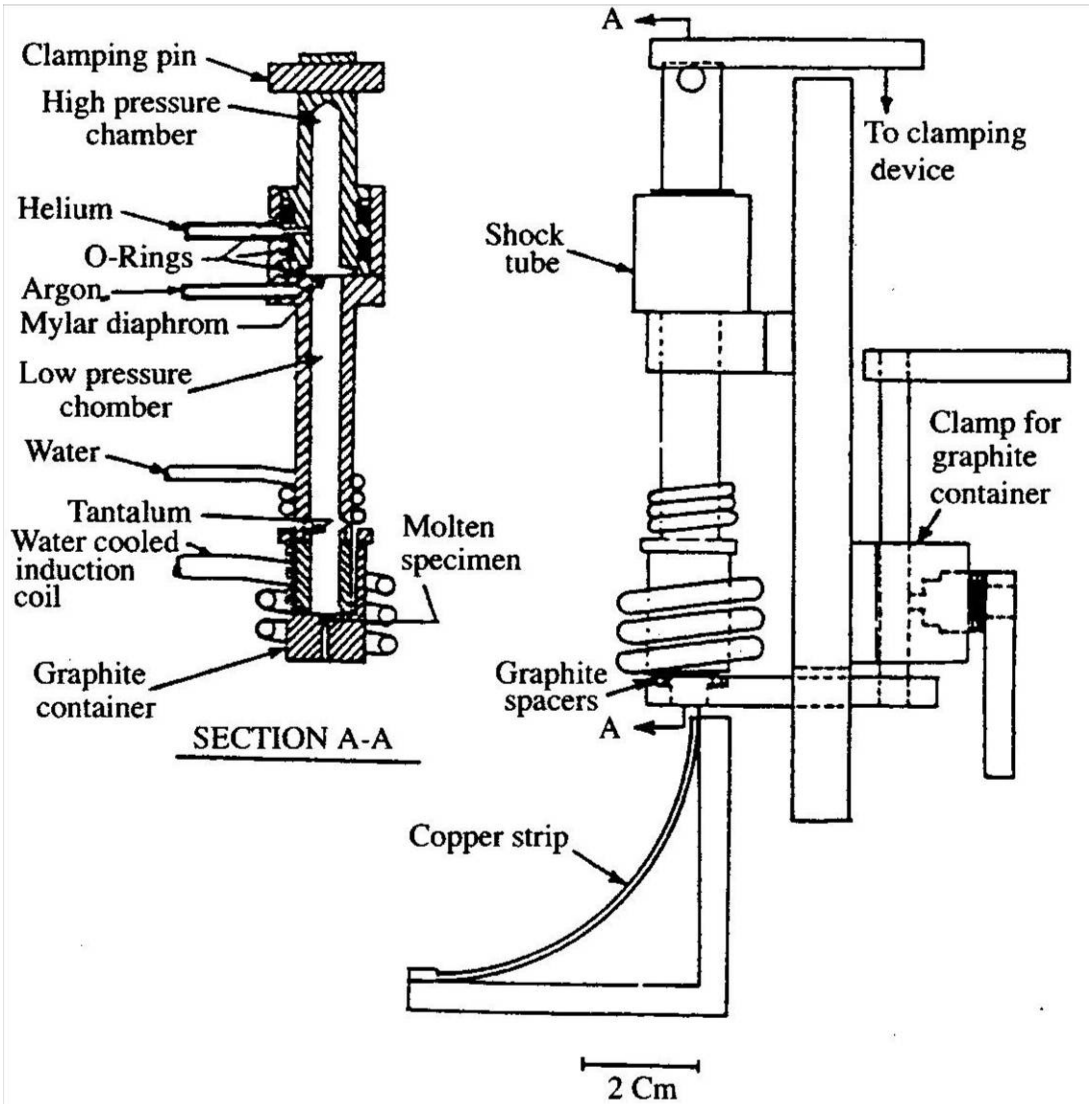

Figure 1.4 Schematic drawing of the splat quenching method [98].

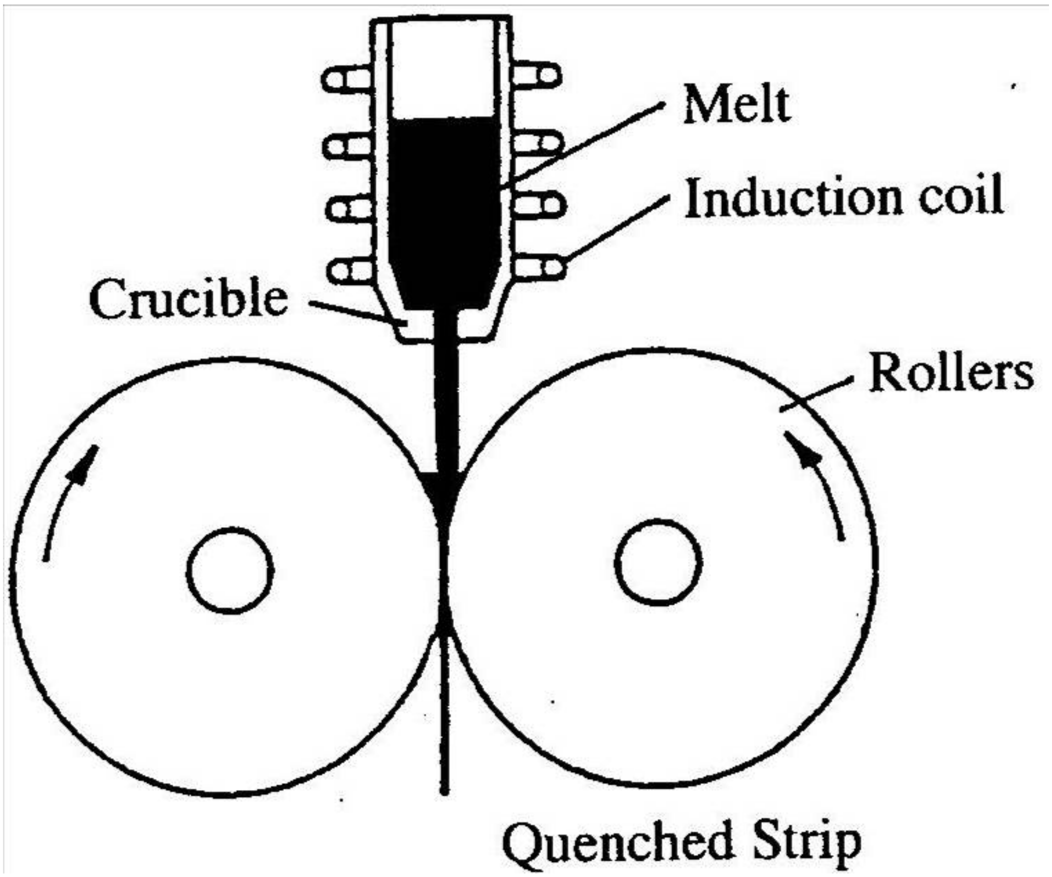

Figure 1.5 Schematic drawing of the two rollers quenching process [13].

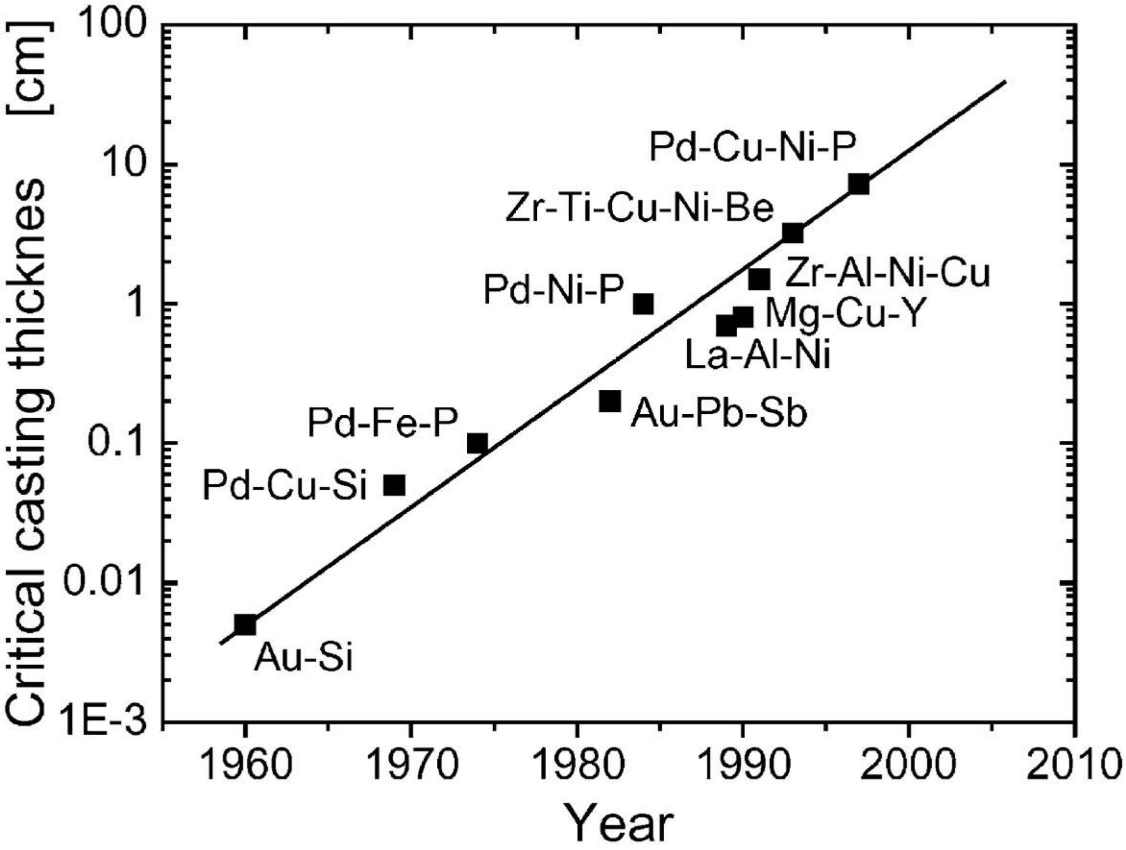

Figure 1.6 The relationship of critical thickness and the date of discovery [26].

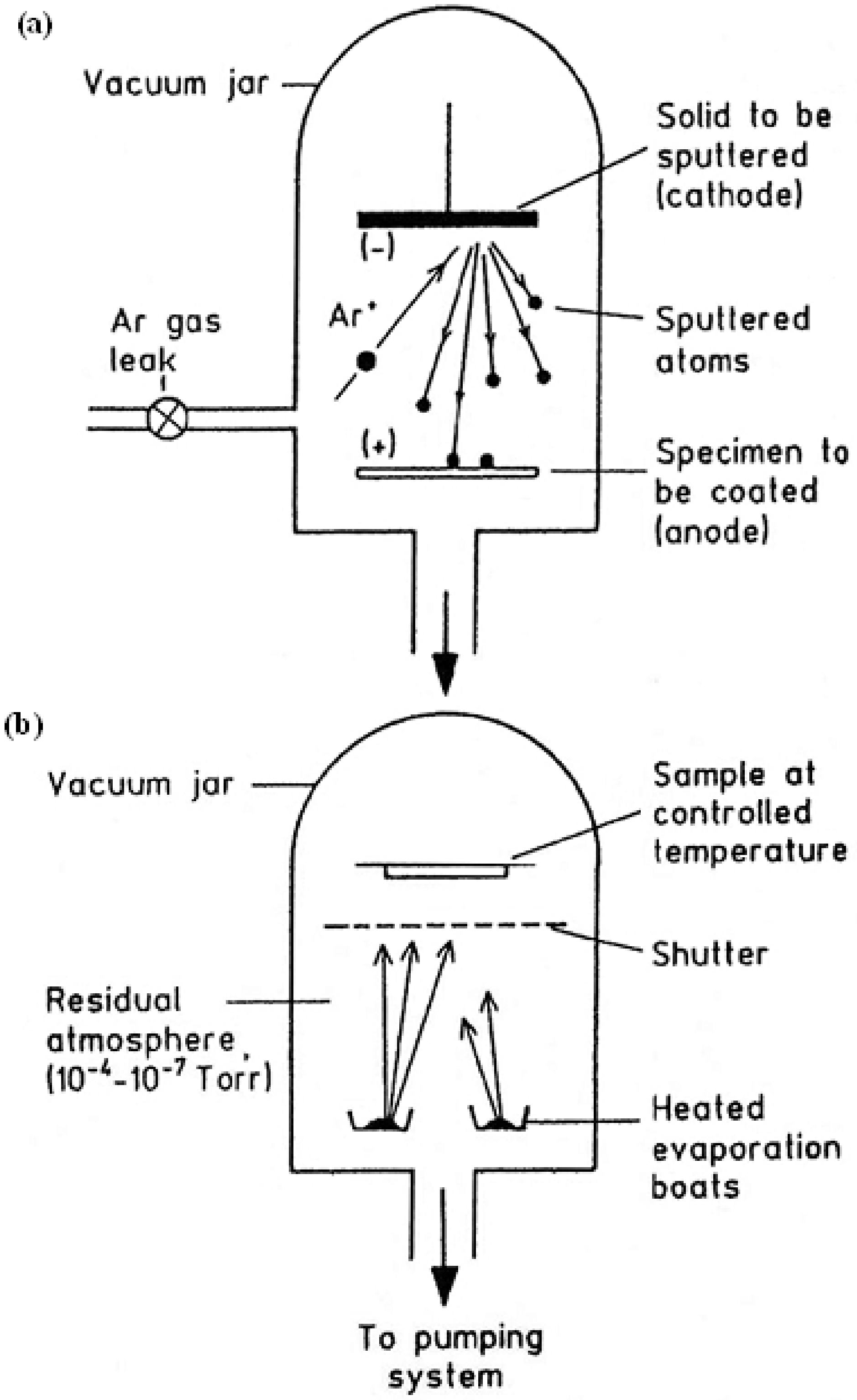

Figure 1.7 Schematic drawing of (a) sputtering and (b) vacuum evaporation [28].

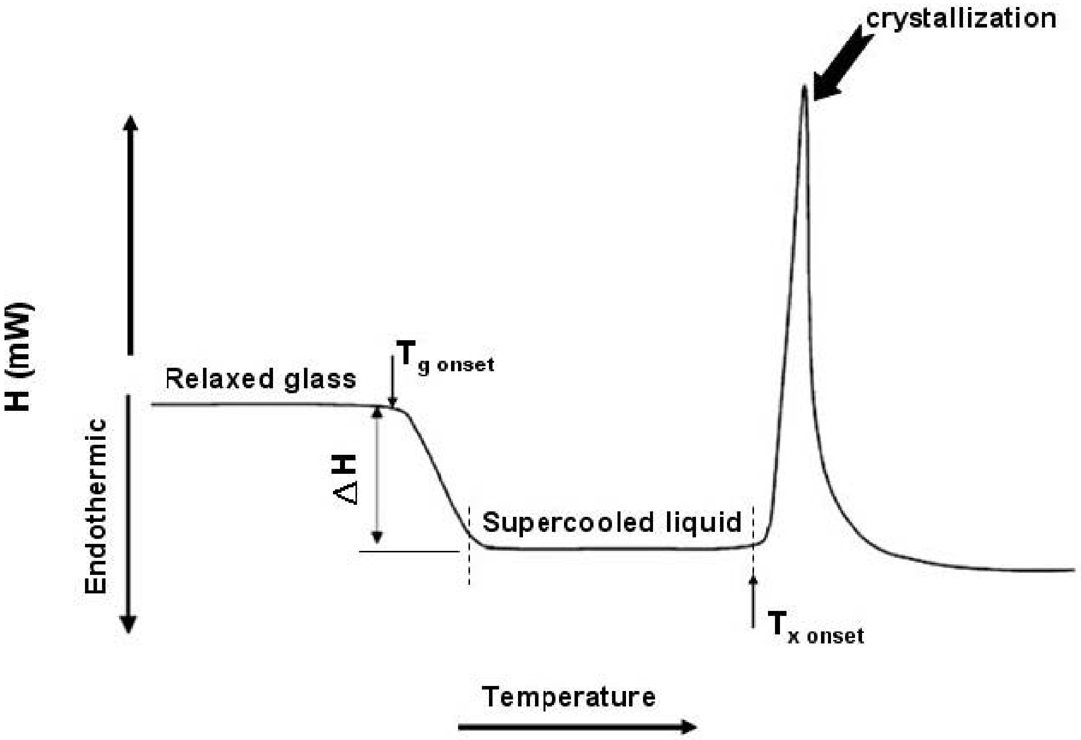

Figure 1.8 The DSC trace of an amorphous alloy [63].

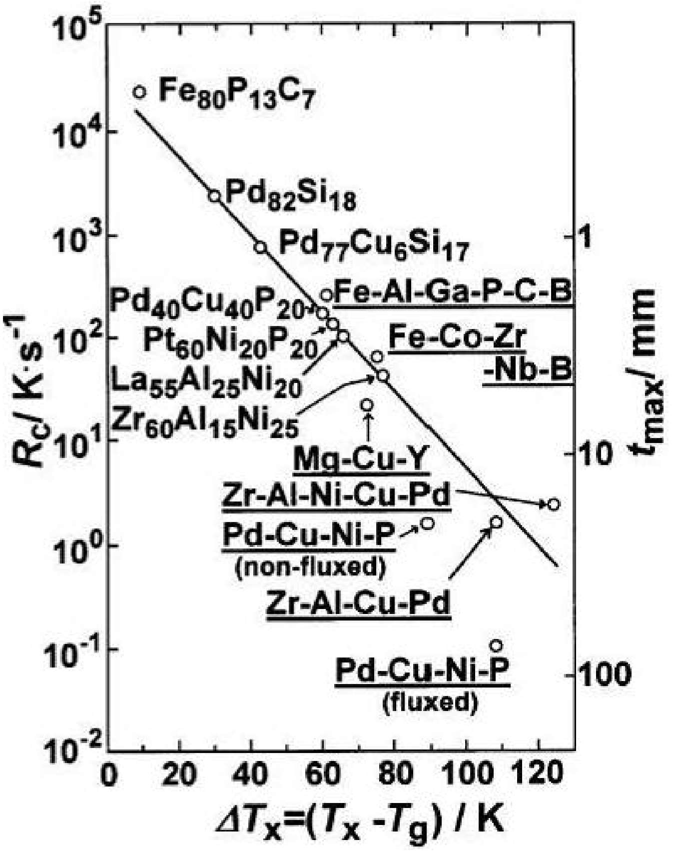

Figure 1.9 The relationship of R_c and ΔT_x [64].

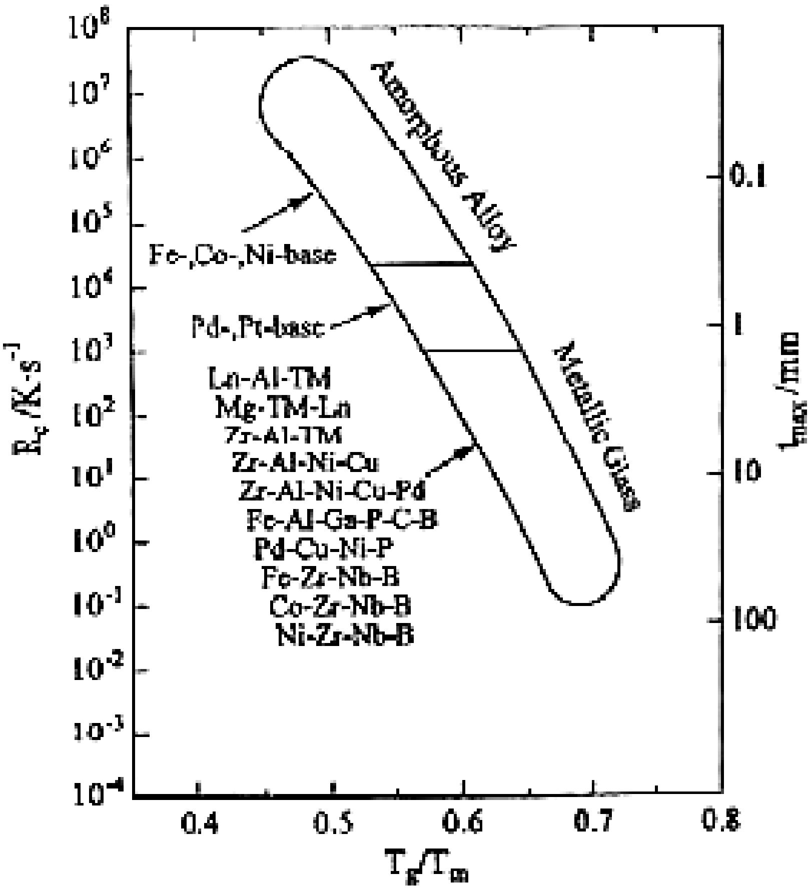

Figure 1.10 The relationship of R_c and T_{rg} [64].

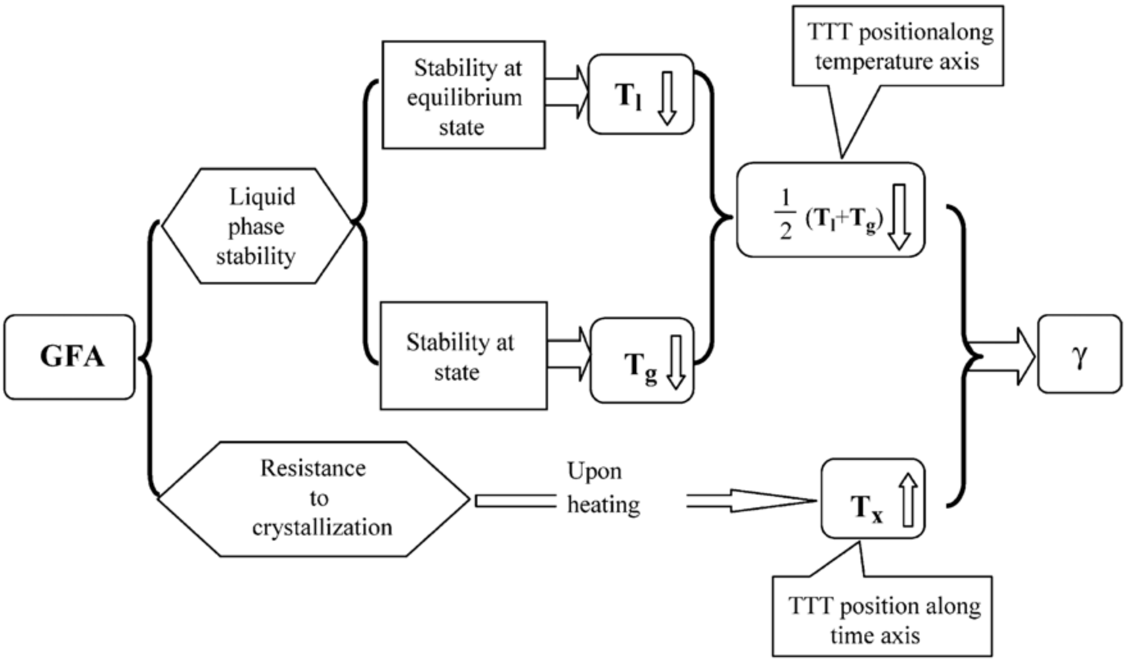

Figure 1.11 The definition of the γ value [72].

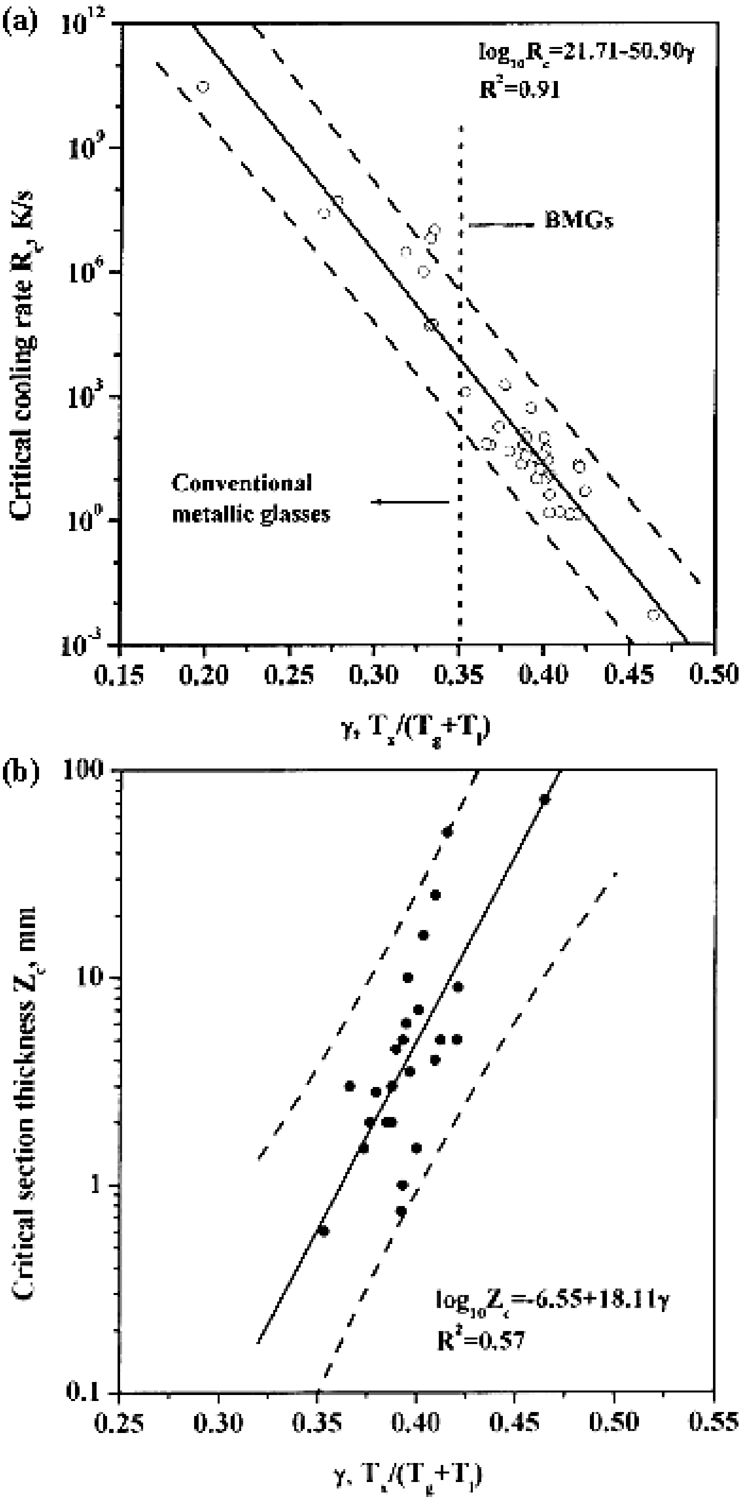

Figure 1.12 The relationship of (a) R_c and γ, and (b) Z_c and γ [71].

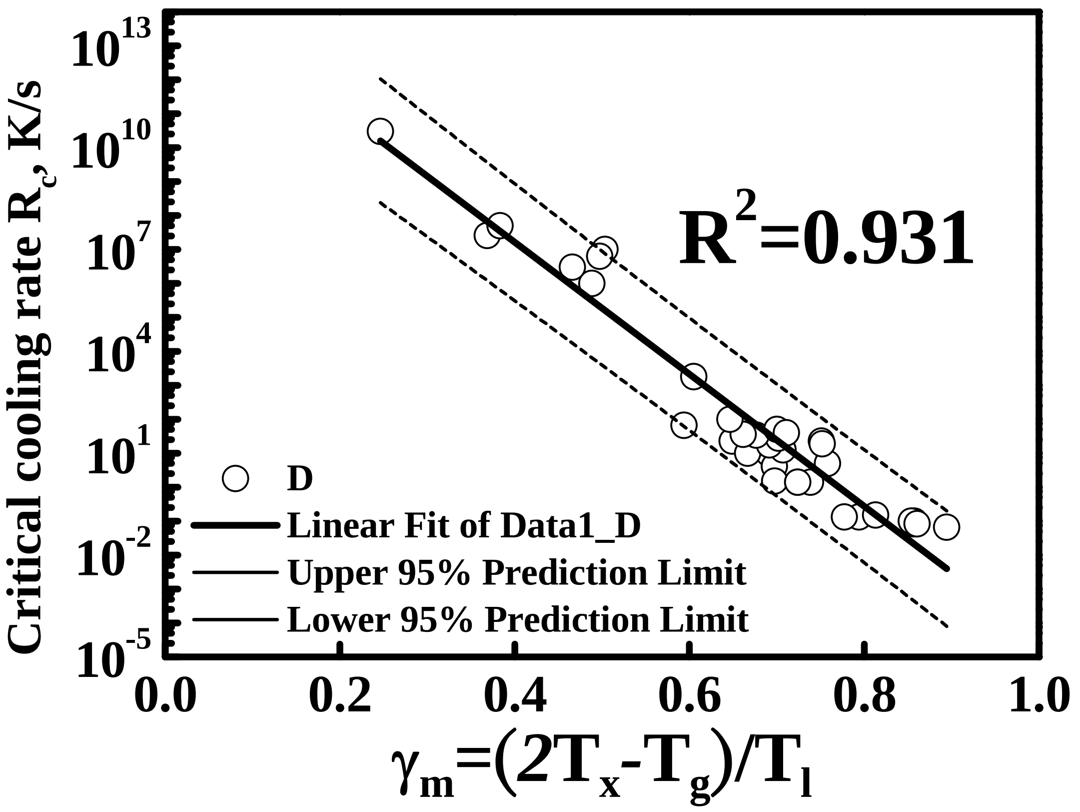

Figure 1.13 The relationship of R_c and γ_m [74].

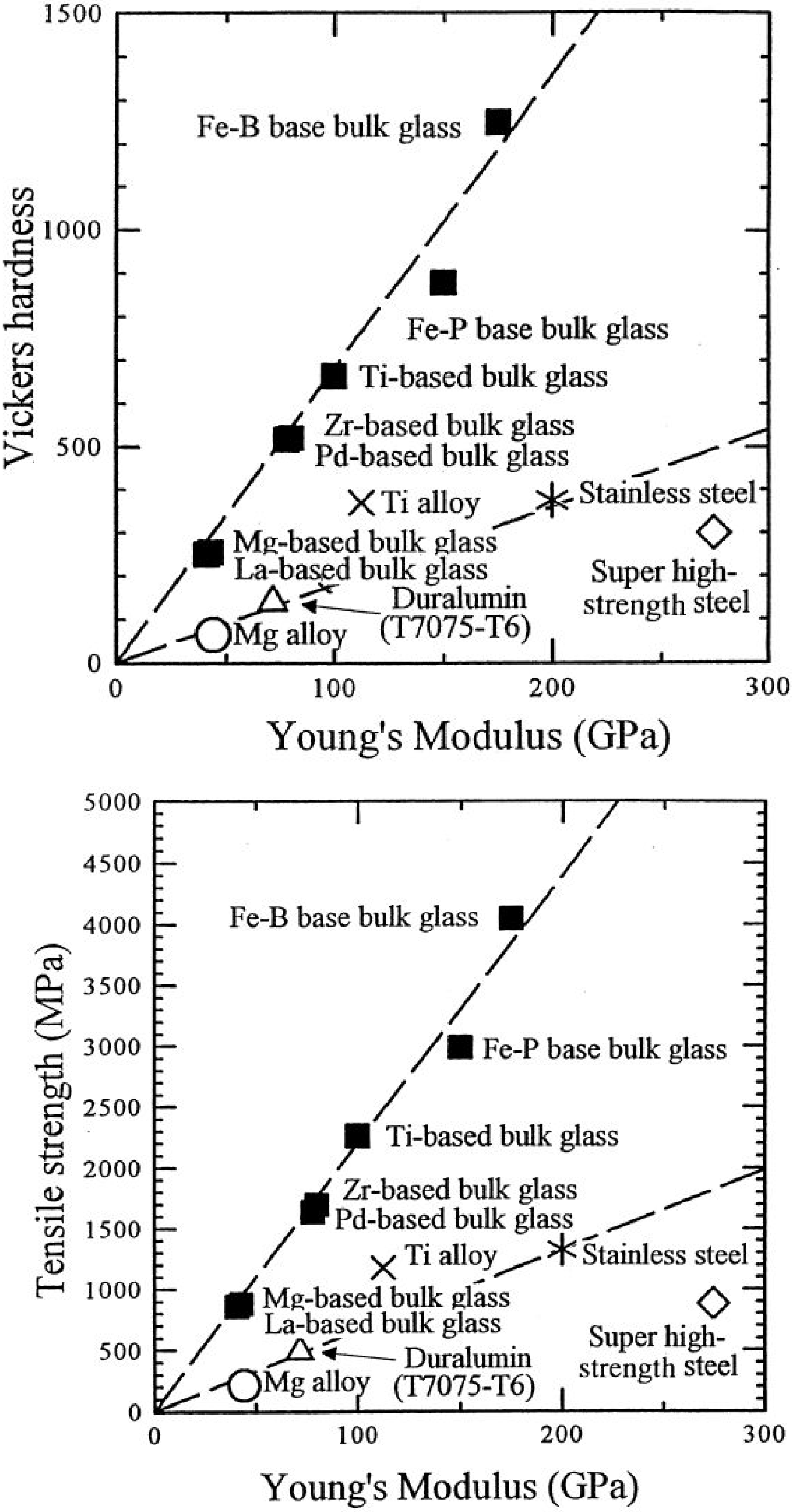

Figure 1.14 Relation between tensile fracture strength, Vickers hardness and Young's modulus for bulk amorphous alloys and conventional crystalline alloys [64].

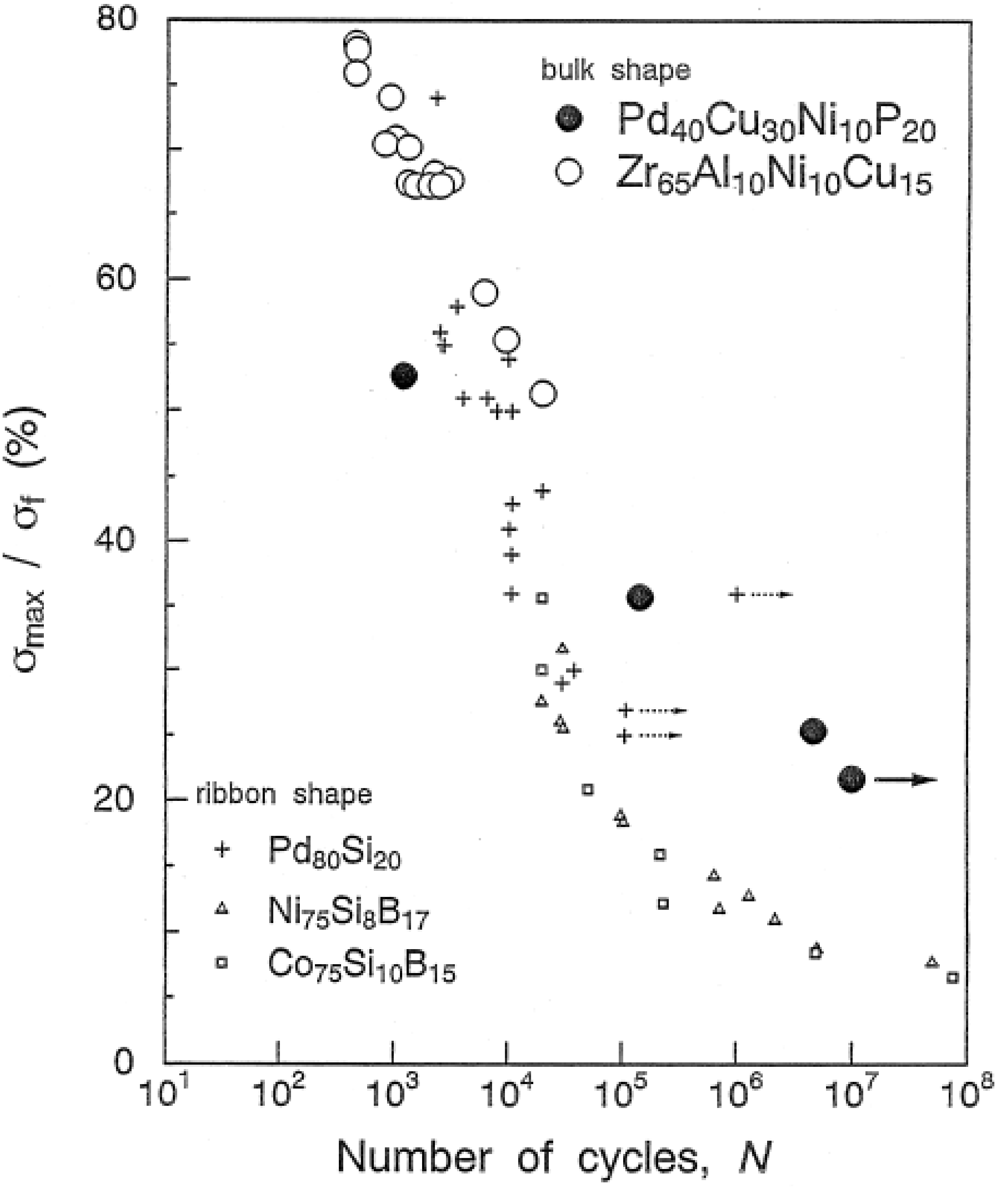

Figure 1.15 Maximum bending and rotating beam fatigue stress as a function of cyclic number up to failure for bulk amorphous $Zr_{65}Al_{10}Ni_{10}Cu_{15}$ and $Pd_{40}Cu_{30}Ni_{10}P_{20}$ alloys. The data for the melt-spun Pd-, Ni- and Co-based amorphous ribbons are also shown for comparison [78].

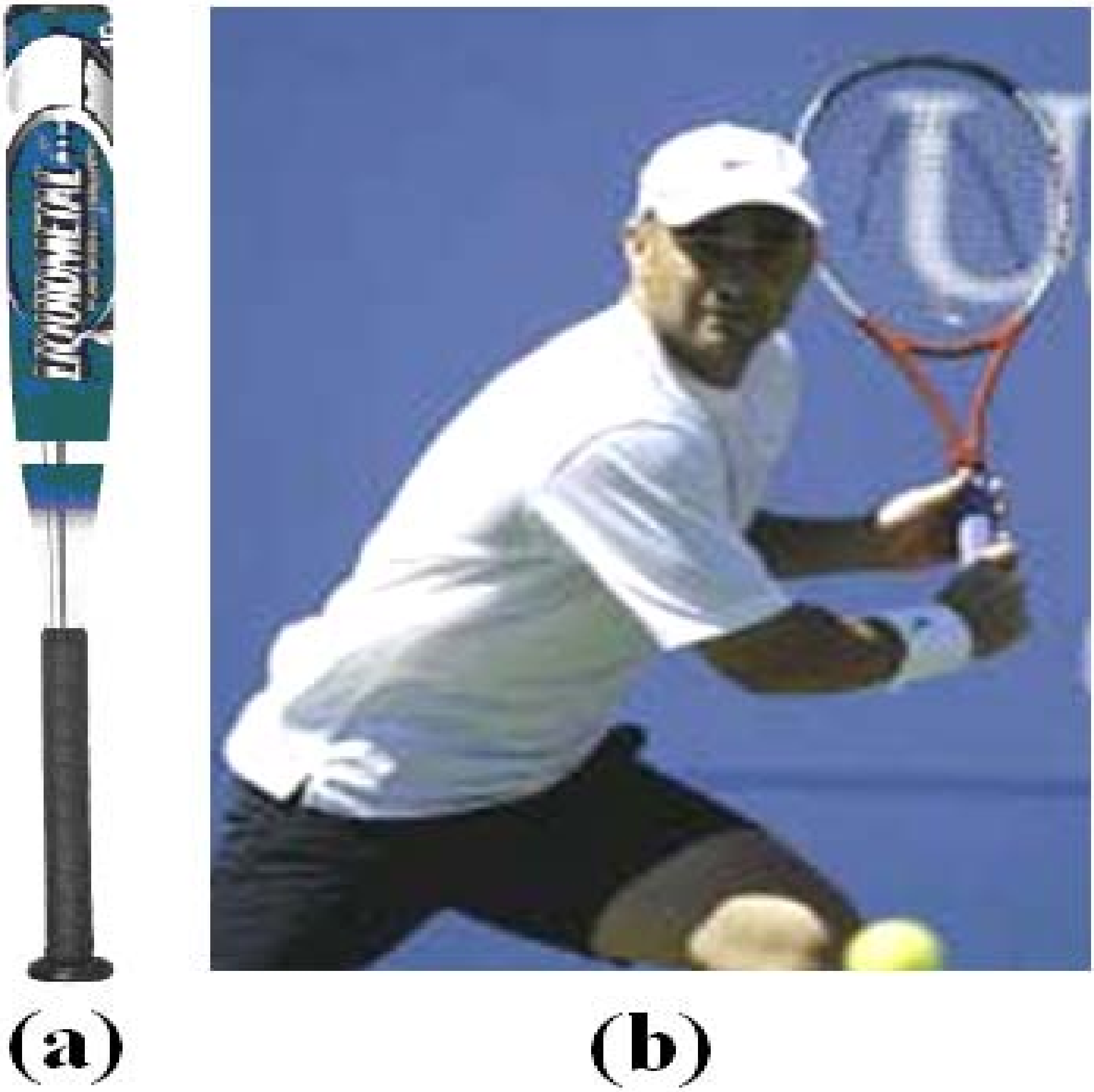

Figure 1.16 The pictures are the Baseball bat featuring based on Vitreloy (a), and tennis racket with BMGs casting in the frame (b) [7].

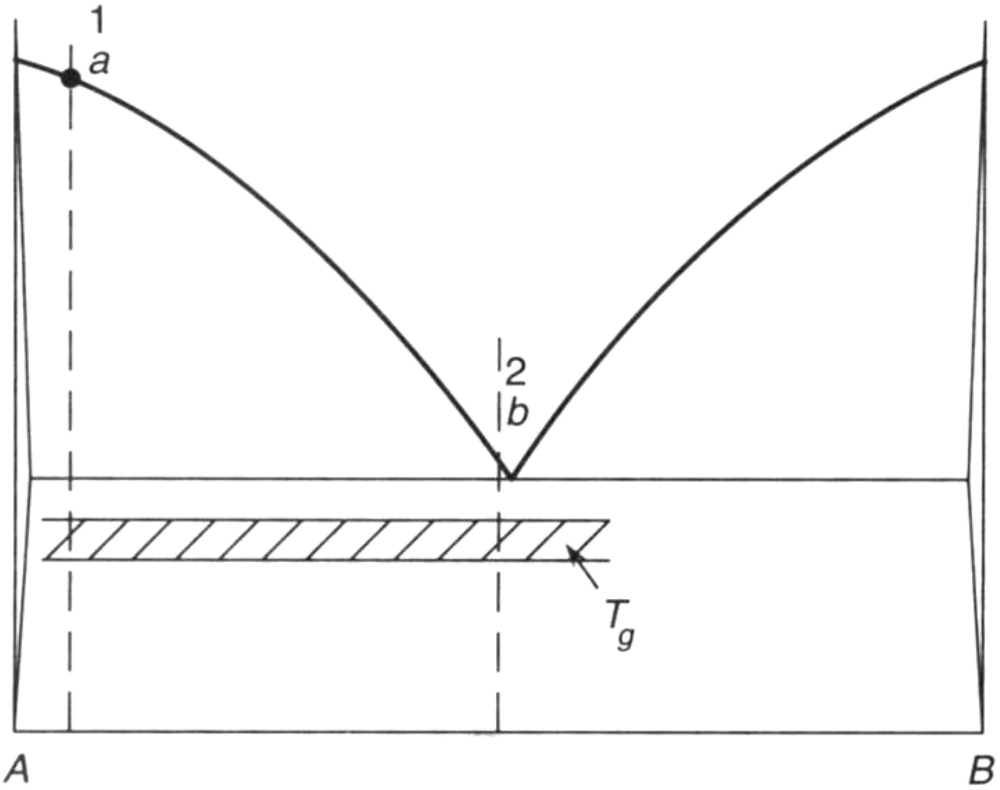

Figure 2.1 Schematic drawing of binary phase diagram [99].

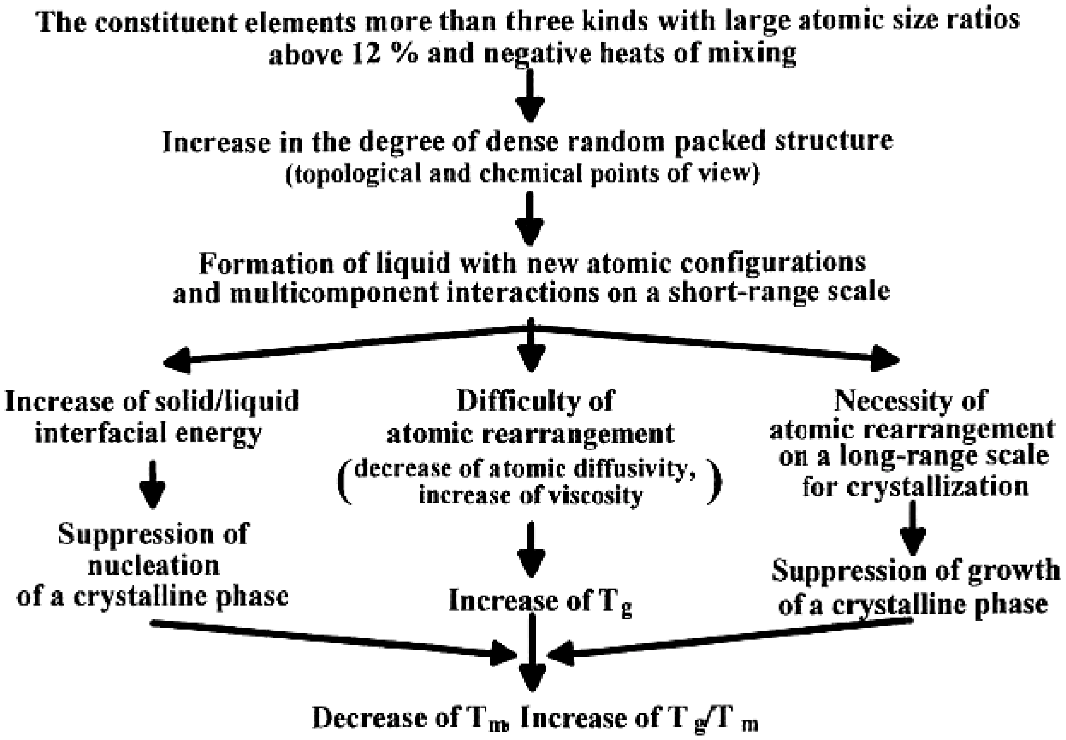

Figure 2.2 Mechanisms for the stabilization of supercooled liquid and the high glass-forming ability [64].

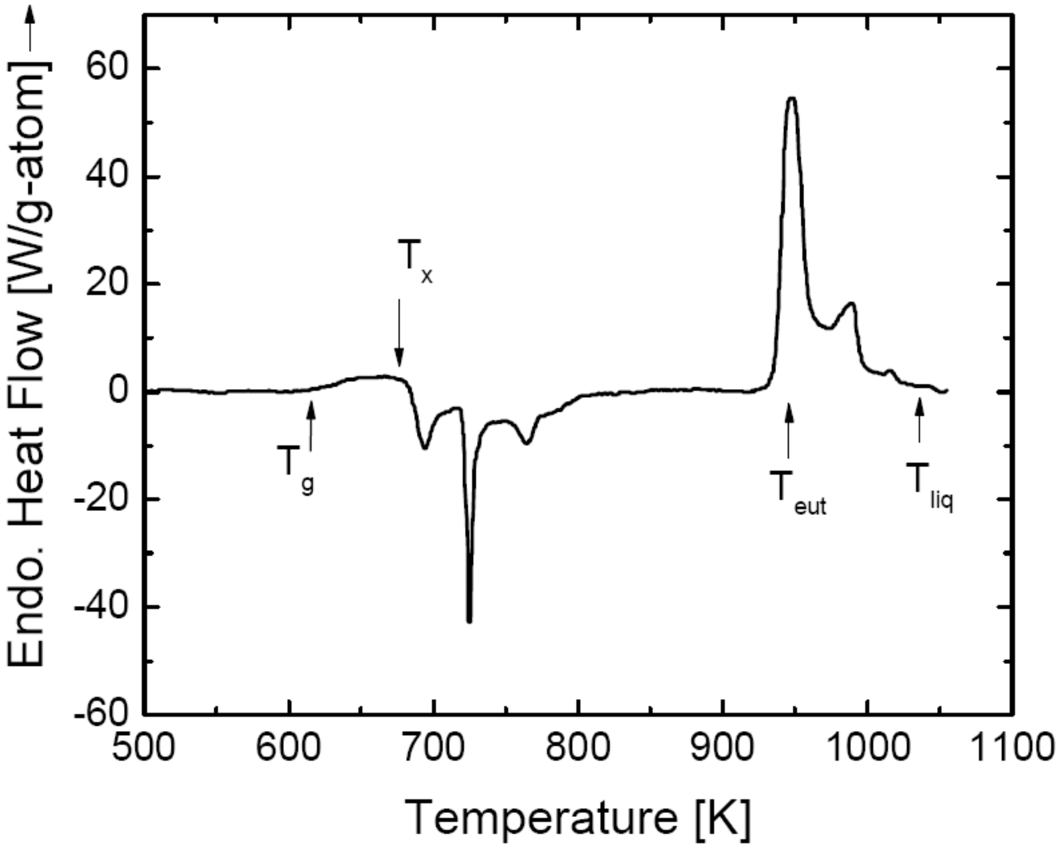

Figure 2.3 Differential Scanning Calorimeter (DSC) thermogram of $Zr_{41.2}Ti_{13.8}Cu_{12.5}Ni_{10}Be_{22.5}$ from 500 to 1150 K using the scan heating rate of 10 K/min [107]. The onset of the glass transition, crystallization temperature, eutectic melting point and liquidus temperatures are depicted by T_g ,T_x, T_{eut} and T_{liq} respectively.

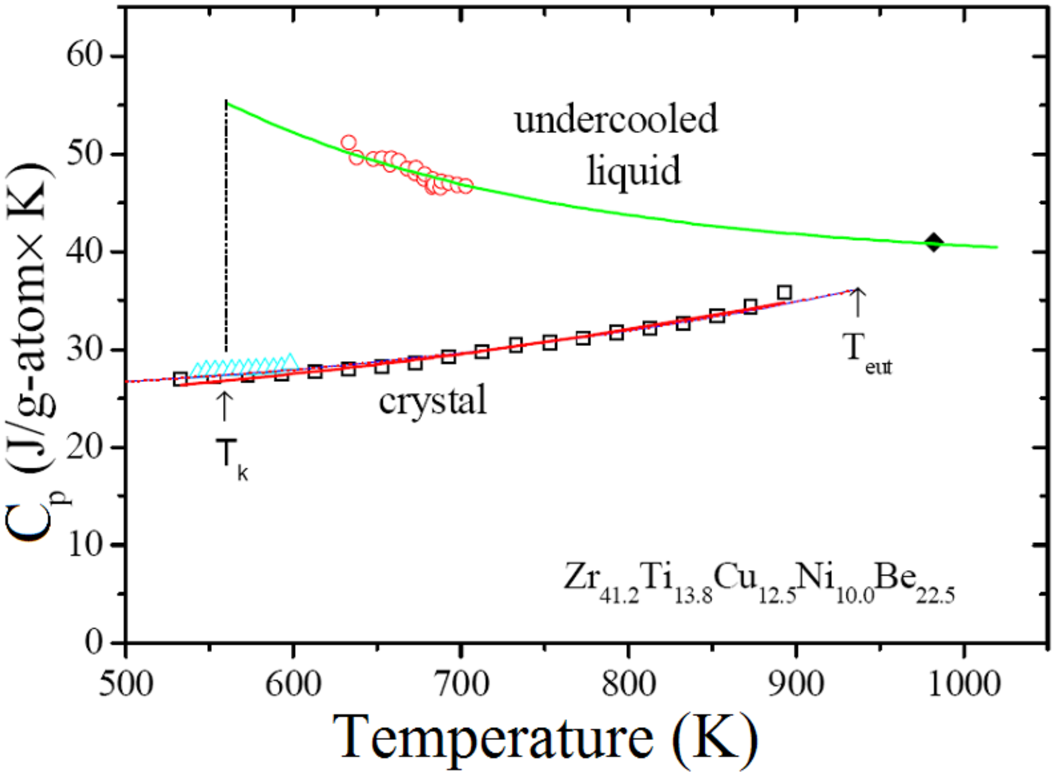

Figure 2.4 Heat capacity curves of the $Zr_{41.2}Ti_{13.8}Cu_{12.5}Ni_{10}Be_{22.5}$ glass, the corresponding liquid and crystalline solid as a function of temperature [107].

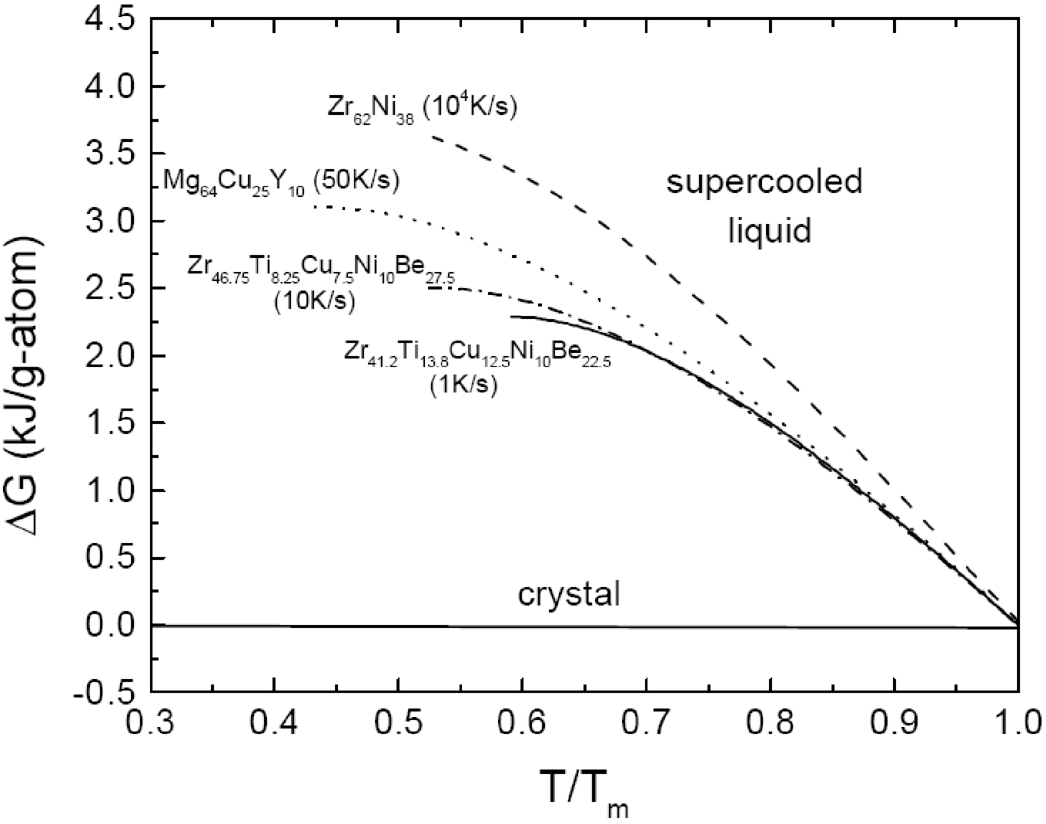

Figure 2.5 The Gibbs free energy difference between crystal and supercooled liquid for different various glass forming liquids. Vit1 with the smallest cooling rate shows the smallest free energy difference [112].

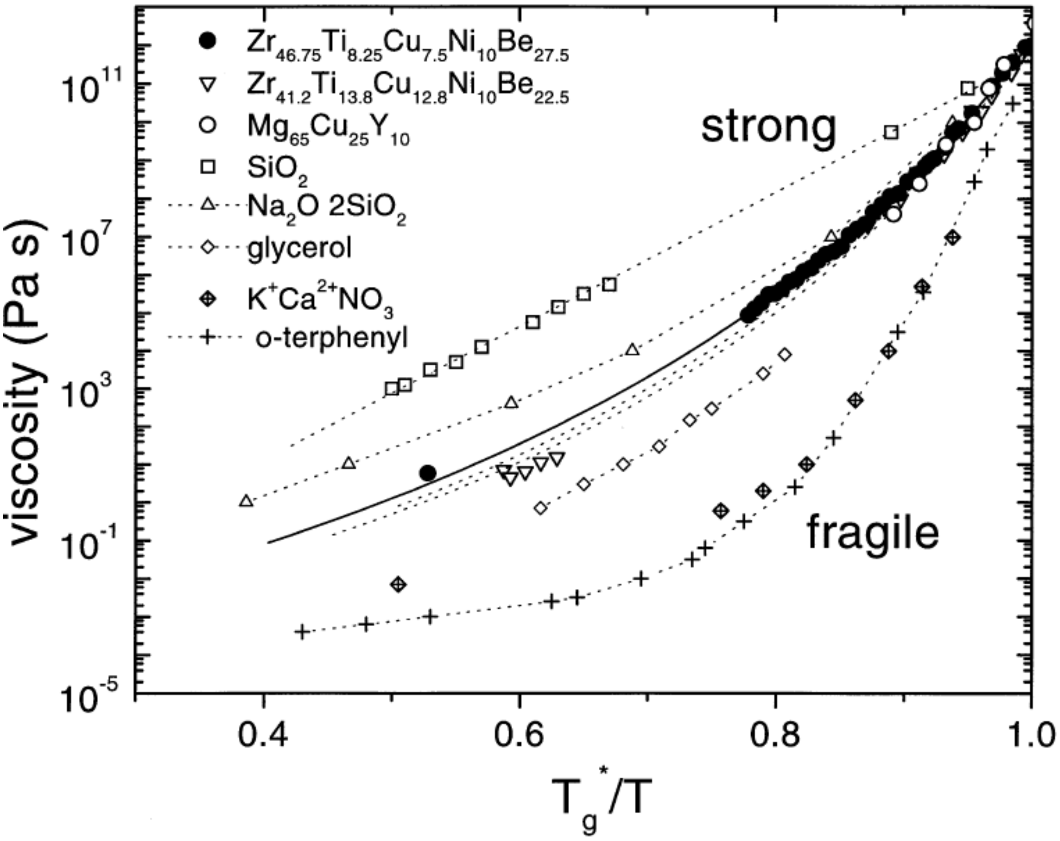

Figure 2.6 Fragility plot of the viscosities of the bulk metallic glasses [143, 106] and several non-metallic "strong" and "fragile" glasses. The data on non-metallic glasses were taken from Angell's literature [1].

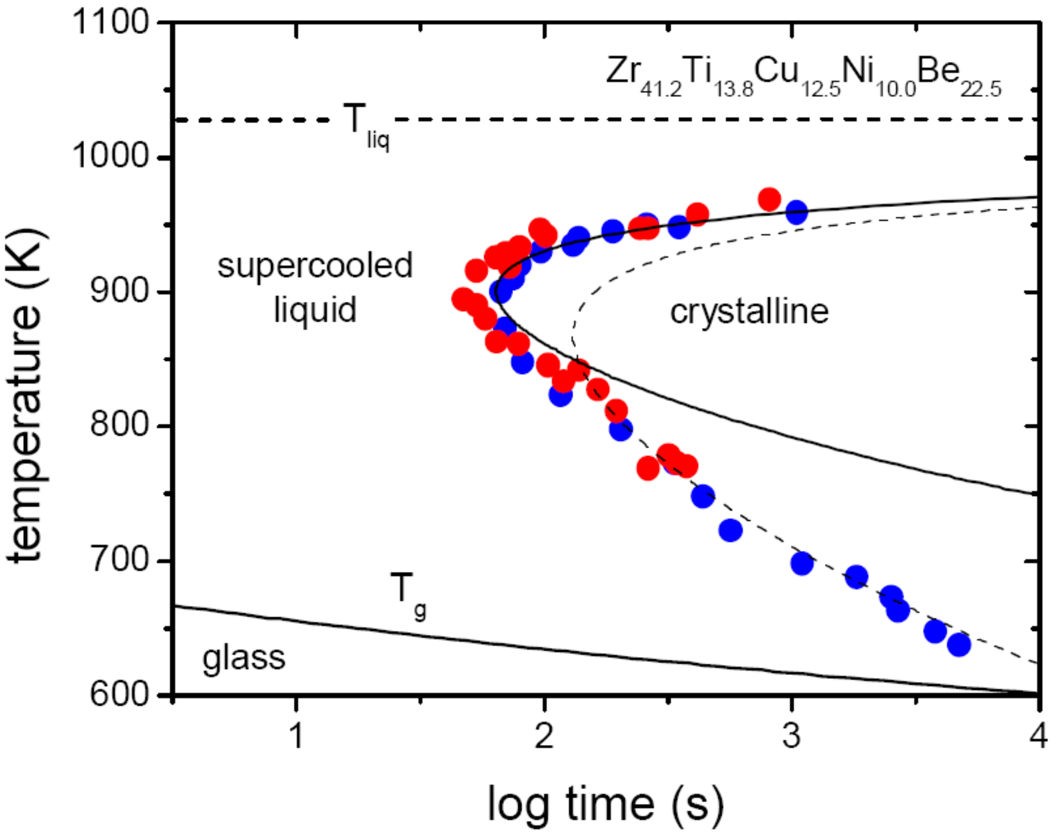

Figure 2.7 TTT Diagram for BMG showing the liquidus temperature, glass transition temperature, super cooled liquid region, and the crystalline nose. The samples have not been sheared during the experiment. The solid line and dashed line show the fits obtained by using $D_{eff} \propto 1/\eta$ and $D_{eff} \propto \exp(-Q_{eff}/k \cdot T)$ [60].

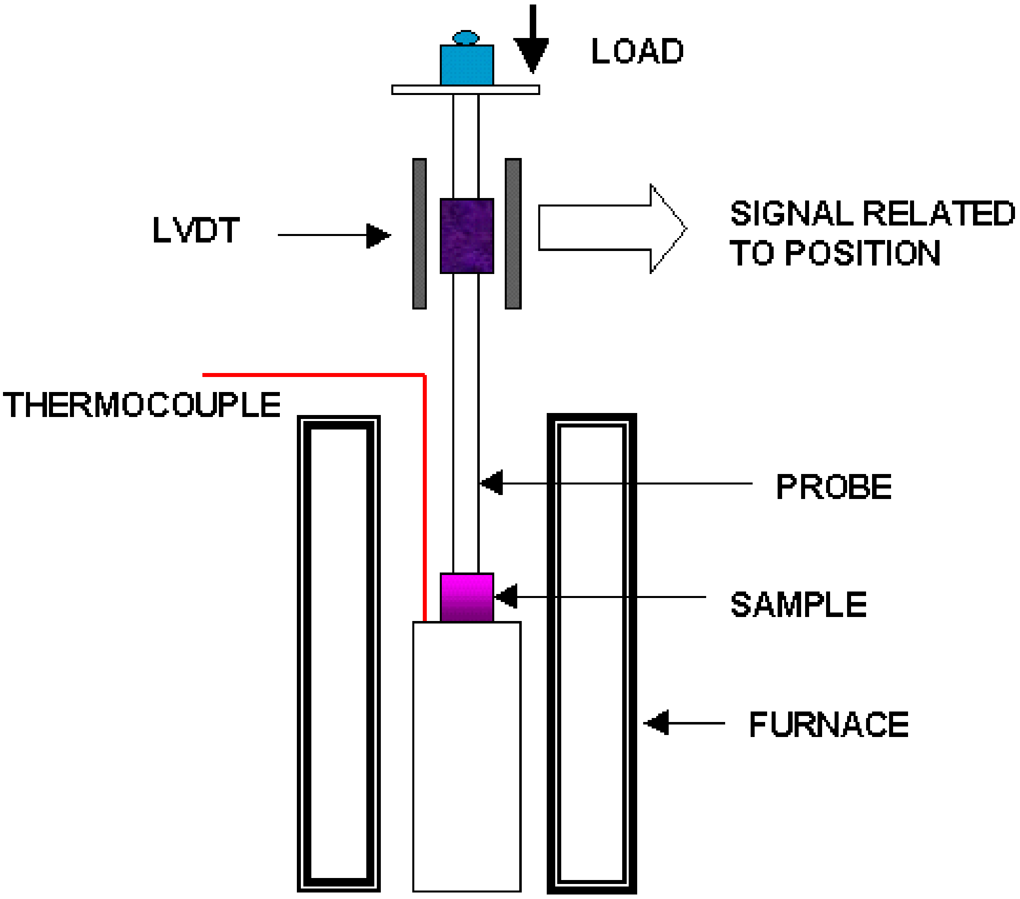

Figure 2.8 Schematic figure of a typical TMA instrument [128].

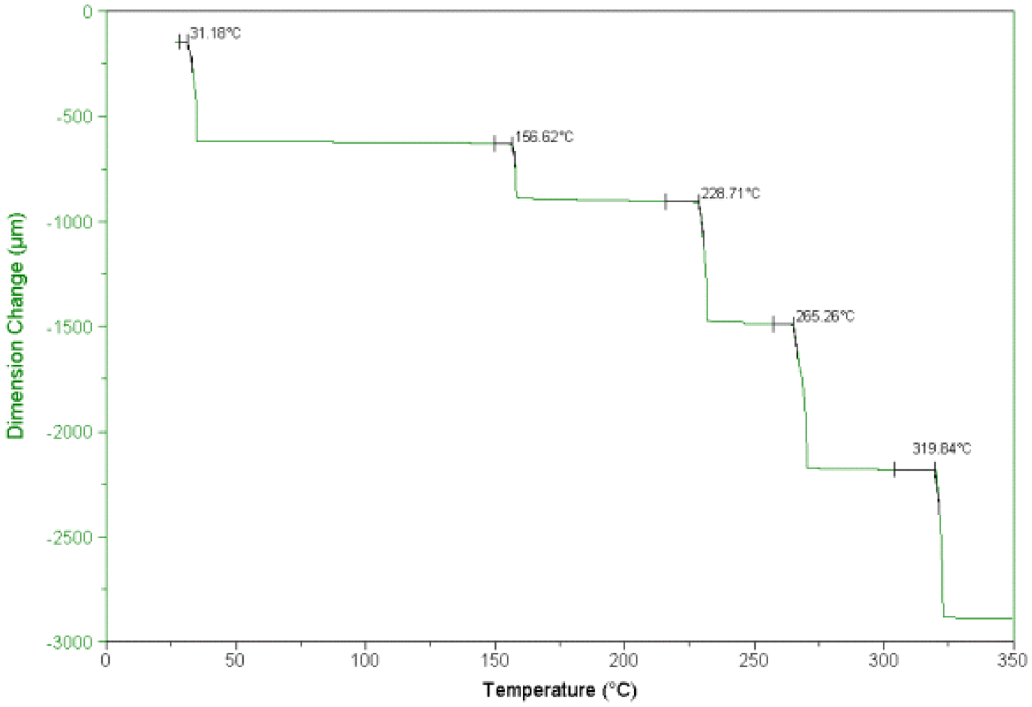

Figure 2.9 The TMA curve for such an experiment [128].

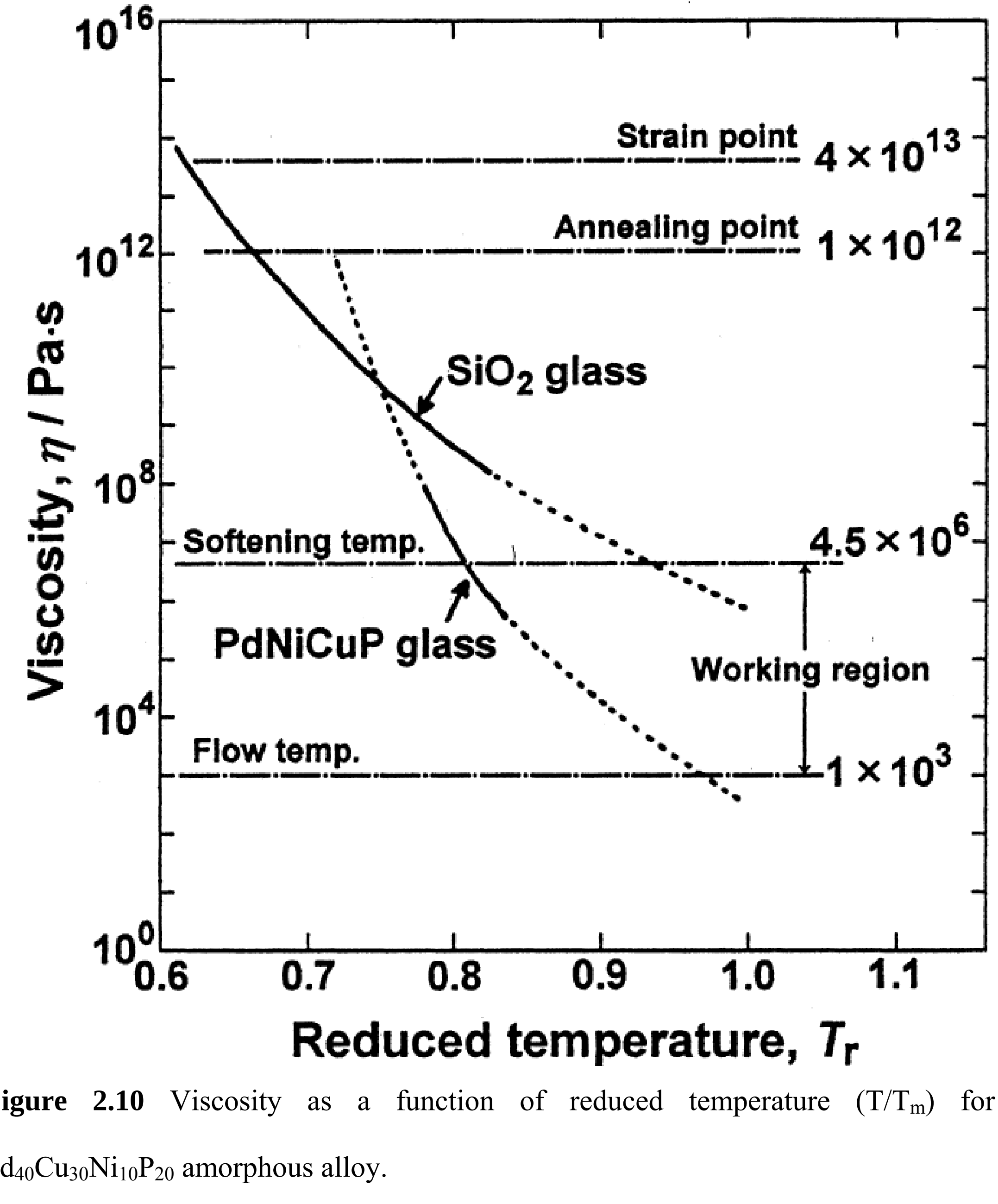

Figure 2.10 Viscosity as a function of reduced temperature (T/T_m) for a $Pd_{40}Cu_{30}Ni_{10}P_{20}$ amorphous alloy.

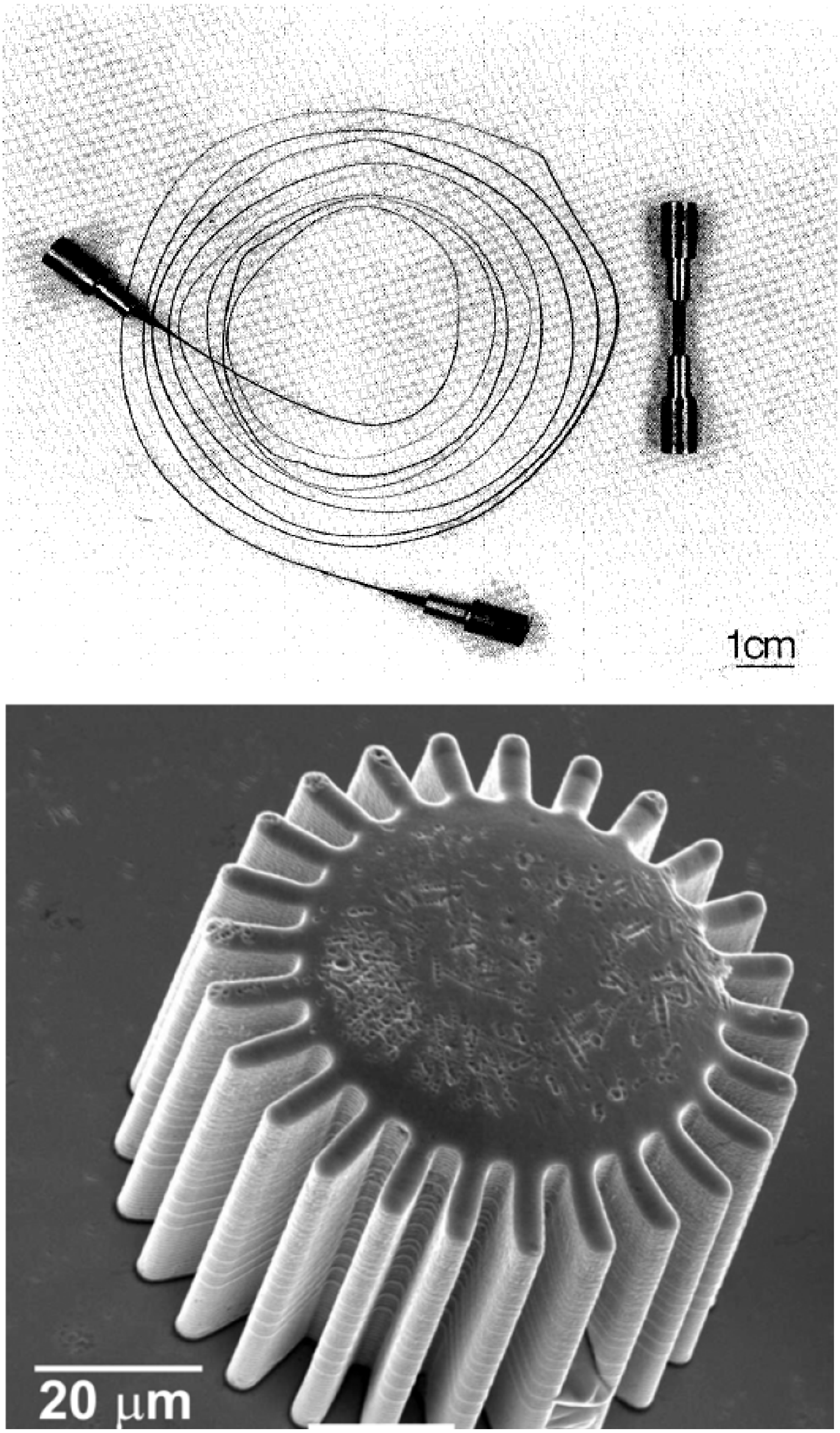

Figure 2.11 Photograph revealing the external appearance of an amorphous La-based cylinder and an amorphous alloy wire and gear-shaped produced by pulling the amorphous cylinder. [132, 144]

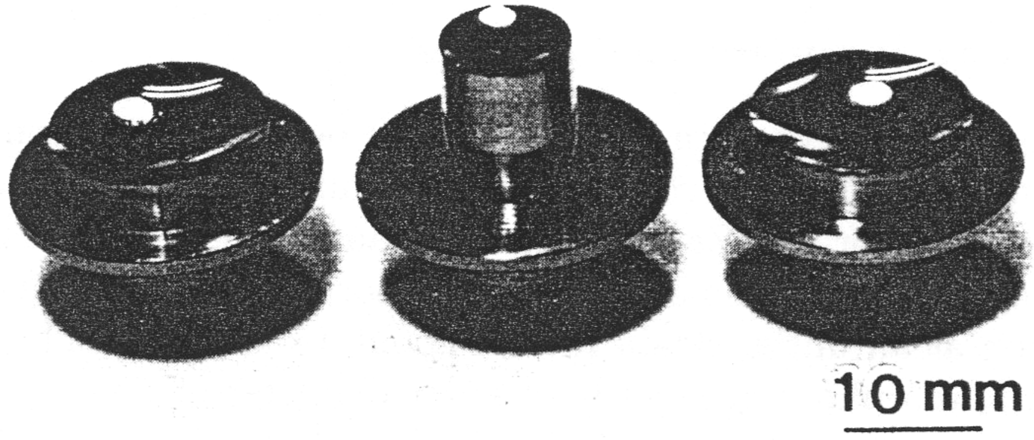

Figure 2.12 Fine precision amorphous alloy mirrors prepared by die forging an amorphous $Zr_{60}Al_{10}Ni_{10}Cu_{20}$ alloy in the supercooled liquid region.

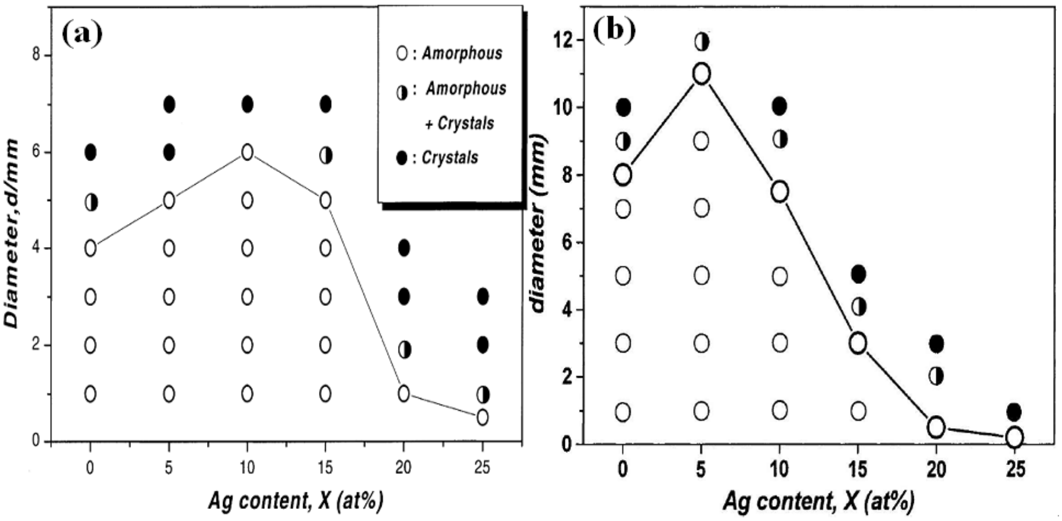

Figure 2.13 Map of the phases for bulk specimens with Ag content in Mg-Cu-Y (a) and Mg-Cu-Gd (b) alloys.

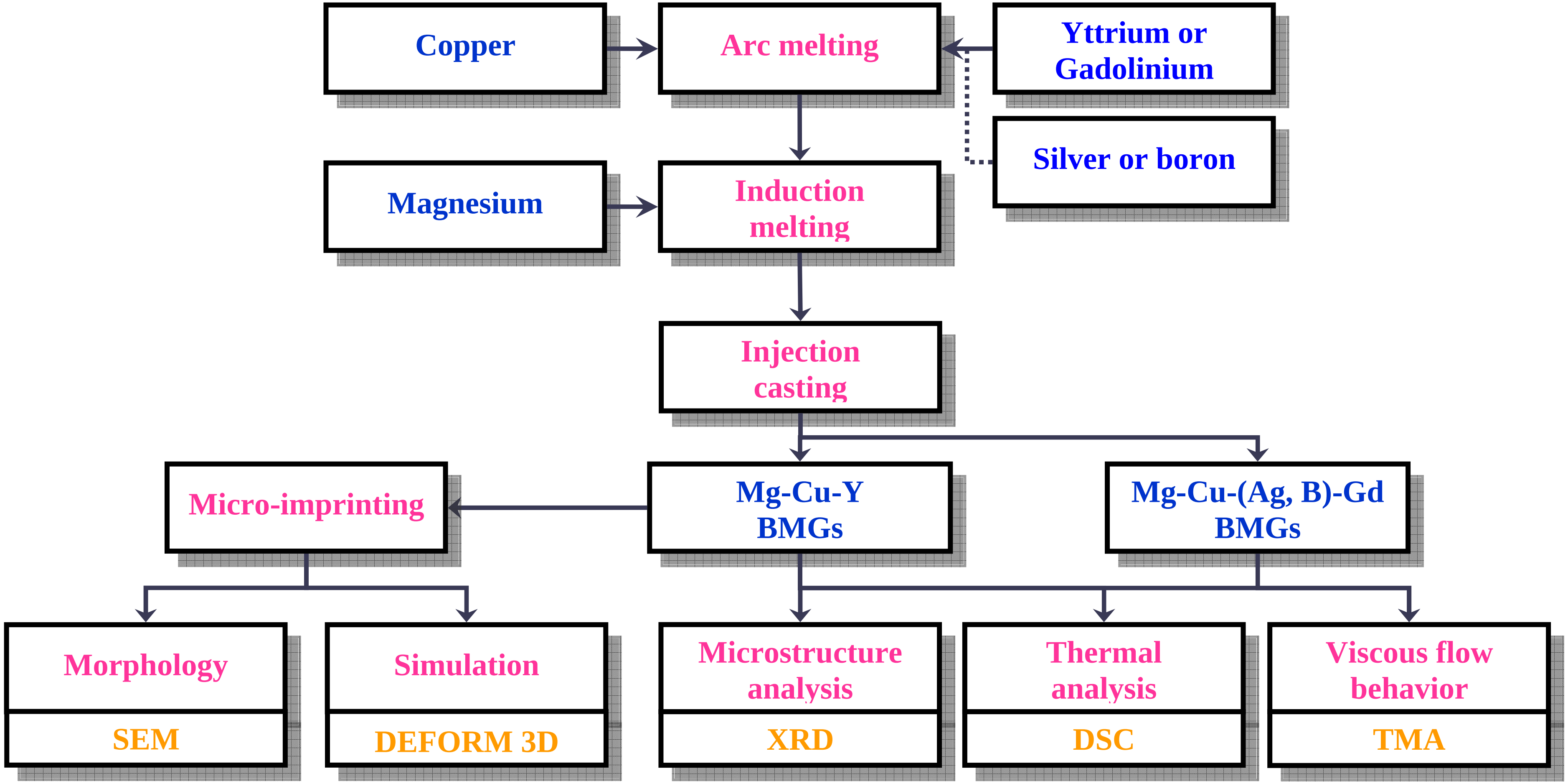

Figure 3.1 The experimental flow chart.

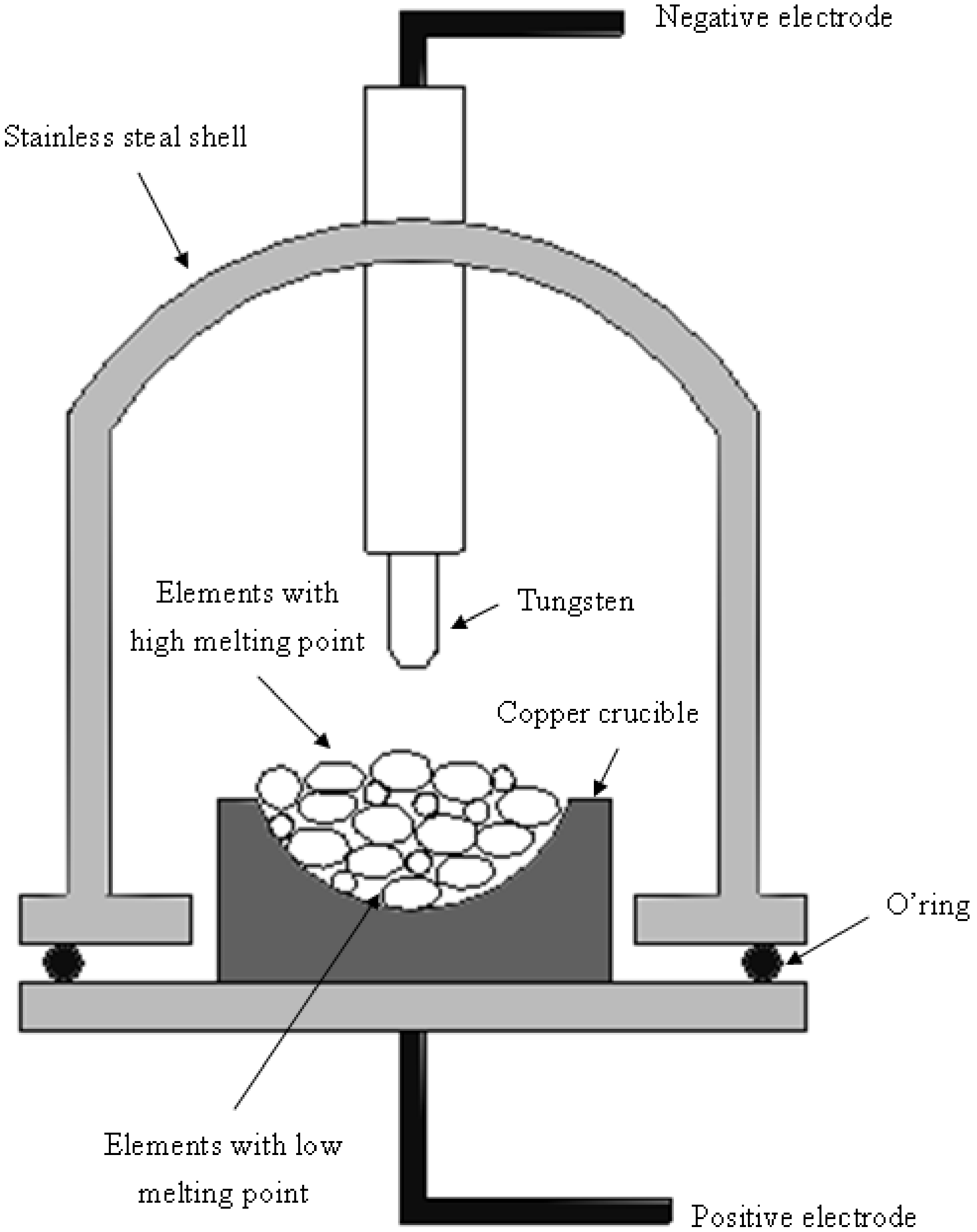

Figure 3.2 The illustration of arc melting furnace [145].

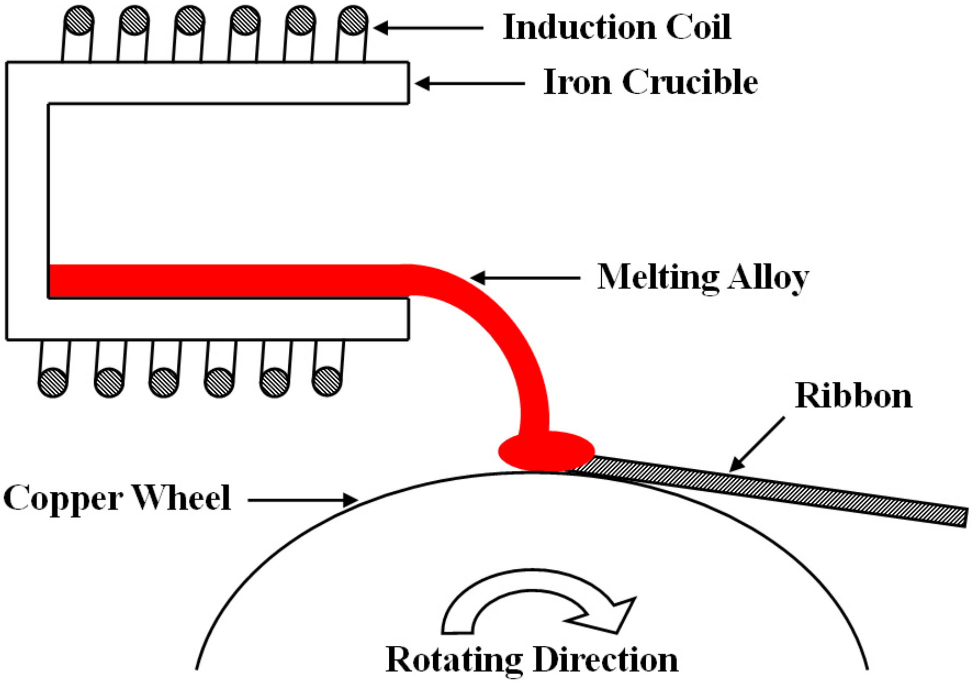

Figure 3.3 The illustration of a single-roller melts spinning process [145].

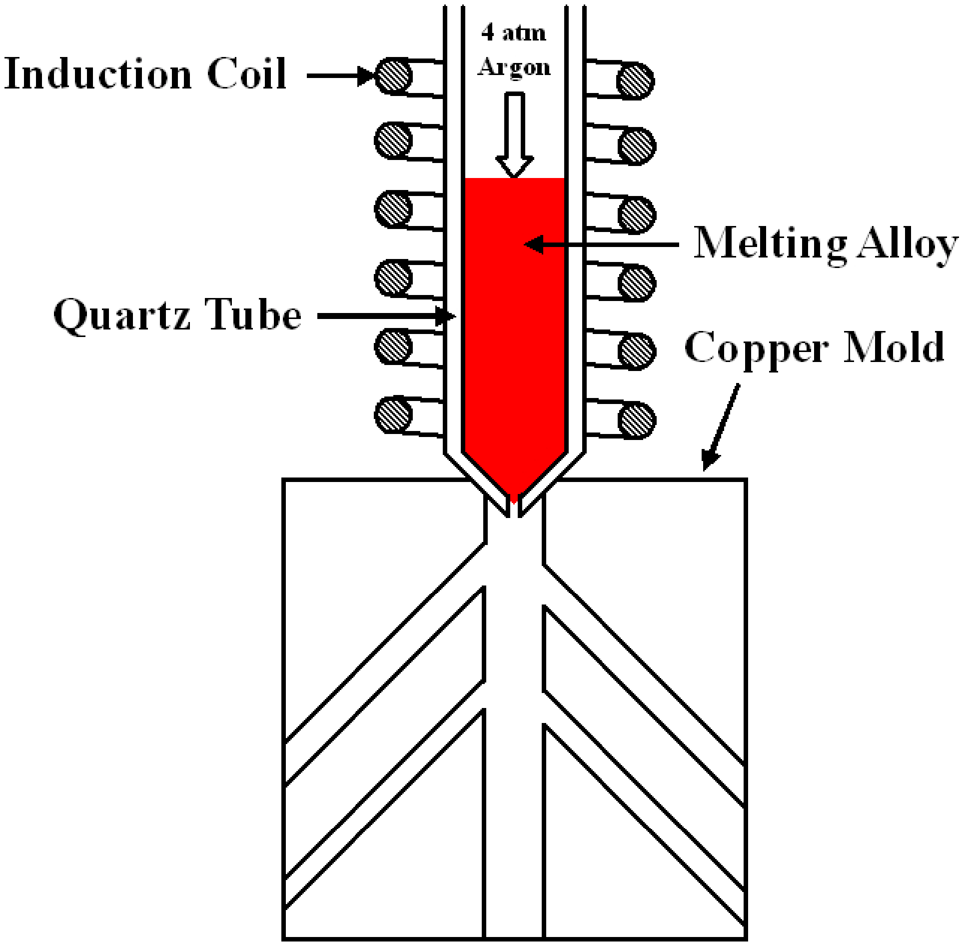

Figure 3.4 The chart of an injection casting process [145].

Figure 3.5 The picture of Perkin Elmer Diamond DSC.

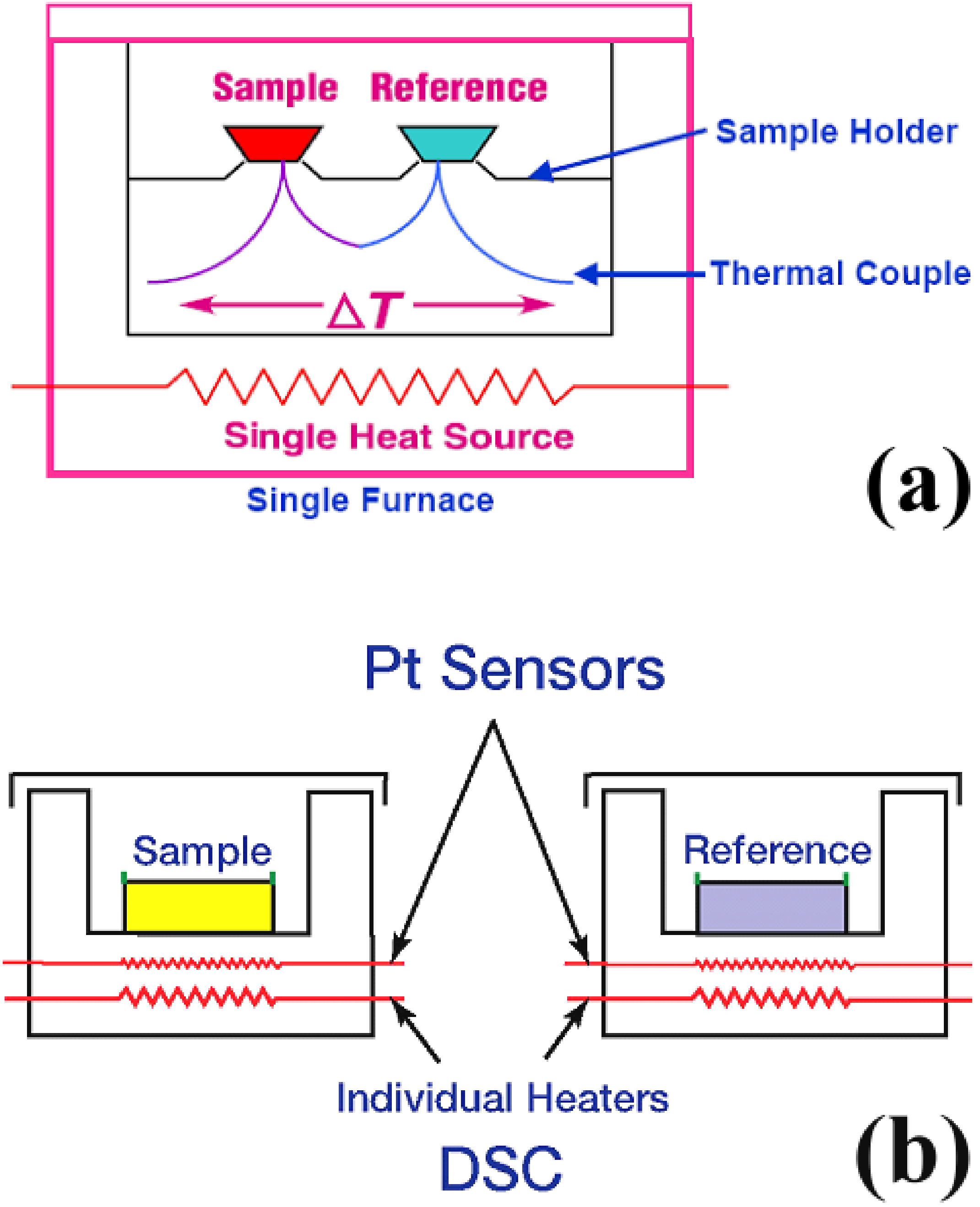

Figure 3.6 The scheme charts of the (a) heat flux (TA 2920 DSC) and (b) power compensation (Perkin Elmer Diamond DSC) differential scanning calorimeters (DSC).

Figure 3.7 The photo of a Shimadzu HMV-2000 Vicker's microhardness tester.

1. Nano Indenter ® XP
2. Vibration Isolation Table
3. Vibration Isolation Cabinet
4. Monitor
5. Computer
6. Continuous Stiffness Measurement
7. Data Acquisition/Control Unit
8. Printer

Figure 3.8 The standard Nano Indenter® XP is a complete, turnkey system consisting of the major components illustrated.

Figure 3.9 The photo of dynamic mechanical analyzer (DMA, Perkin Elmer Diamond DMA)

Figure 3.10 The picture of thermomechanical analyzer (TMA 7, Perkin Elmer Diamond)

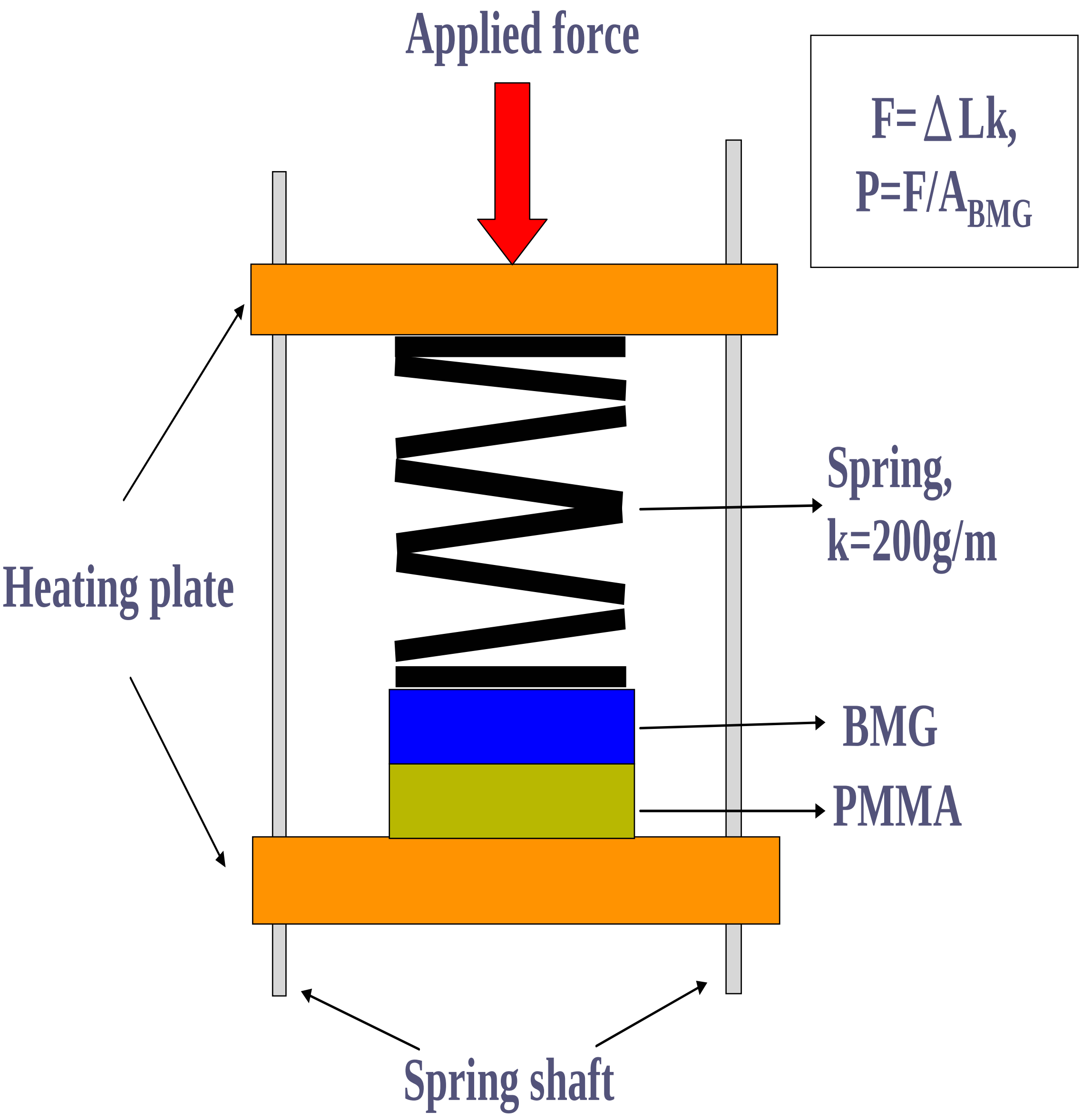

Figure 3.11 Hot embossing set-up spring plate system.

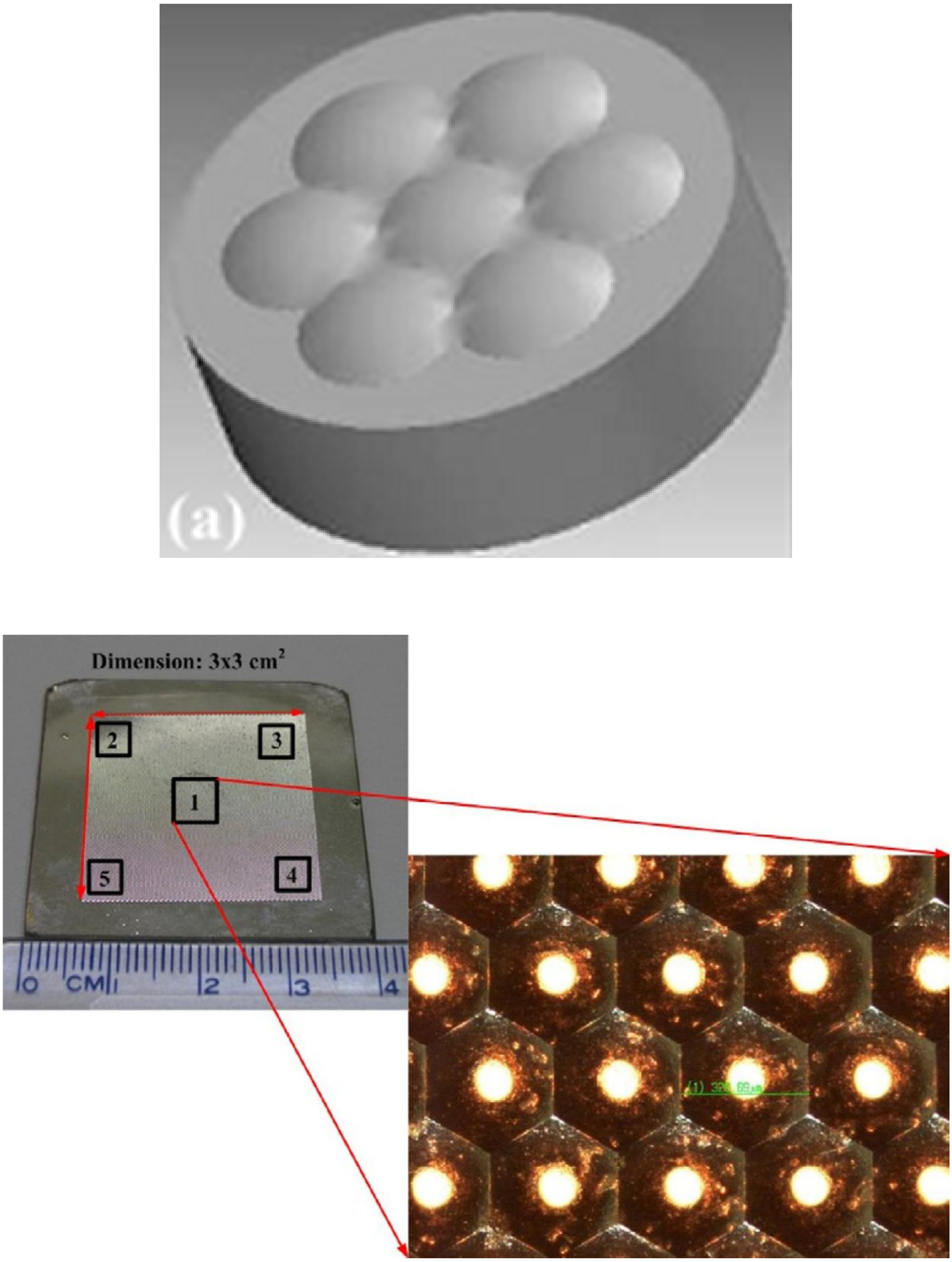

Figure 3.12 The mold used for (a) initial stage simulation and (b) real micro-imprinting experiment.

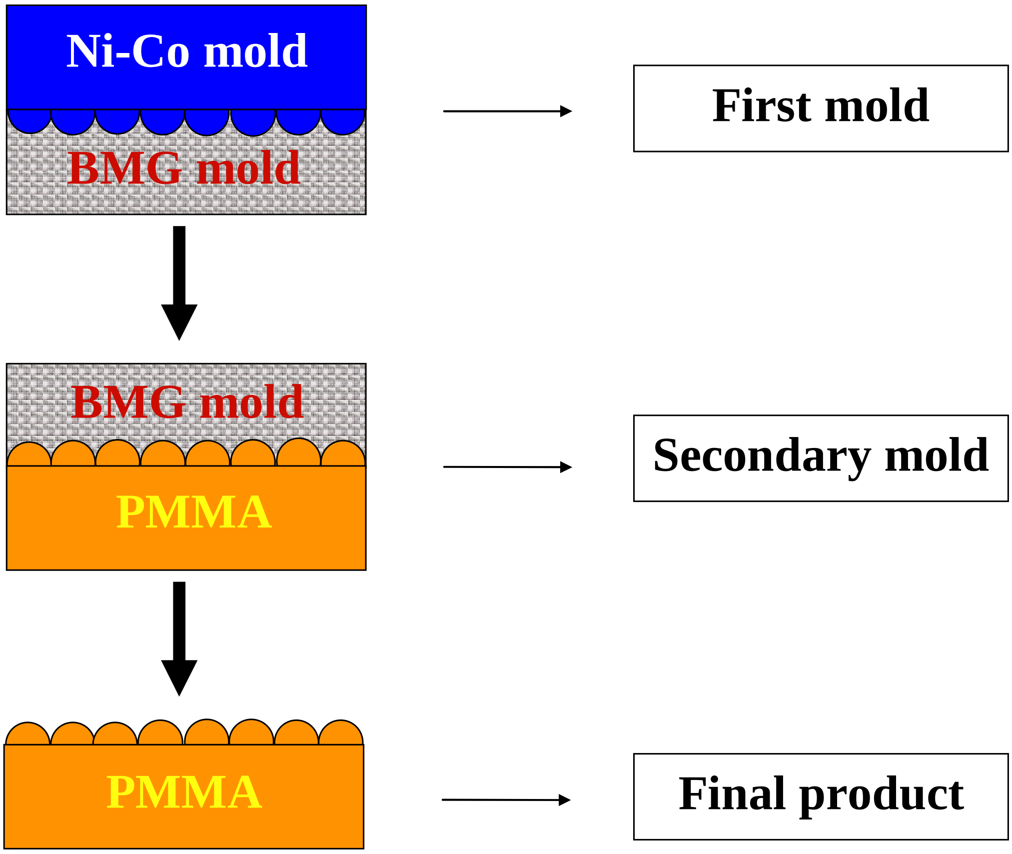

Figure 3.13 The schematic replication process on the PMMA [86, 87].

Figure 4.1 Photograph showing the surface appearance of melt spun $Mg_{58}Cu_{31}Y_{11}$ alloy ribbons.

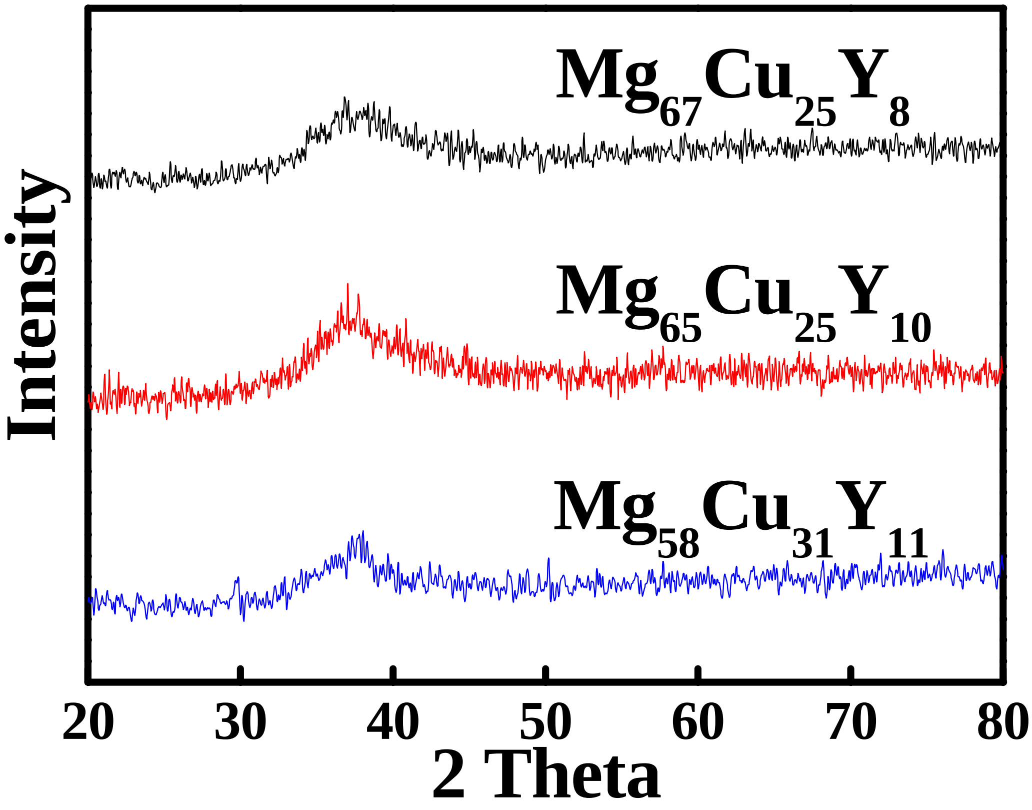

Figure 4.2 X-ray diffraction patterns of the Mg-Cu-Y system amorphous alloy ribbons.

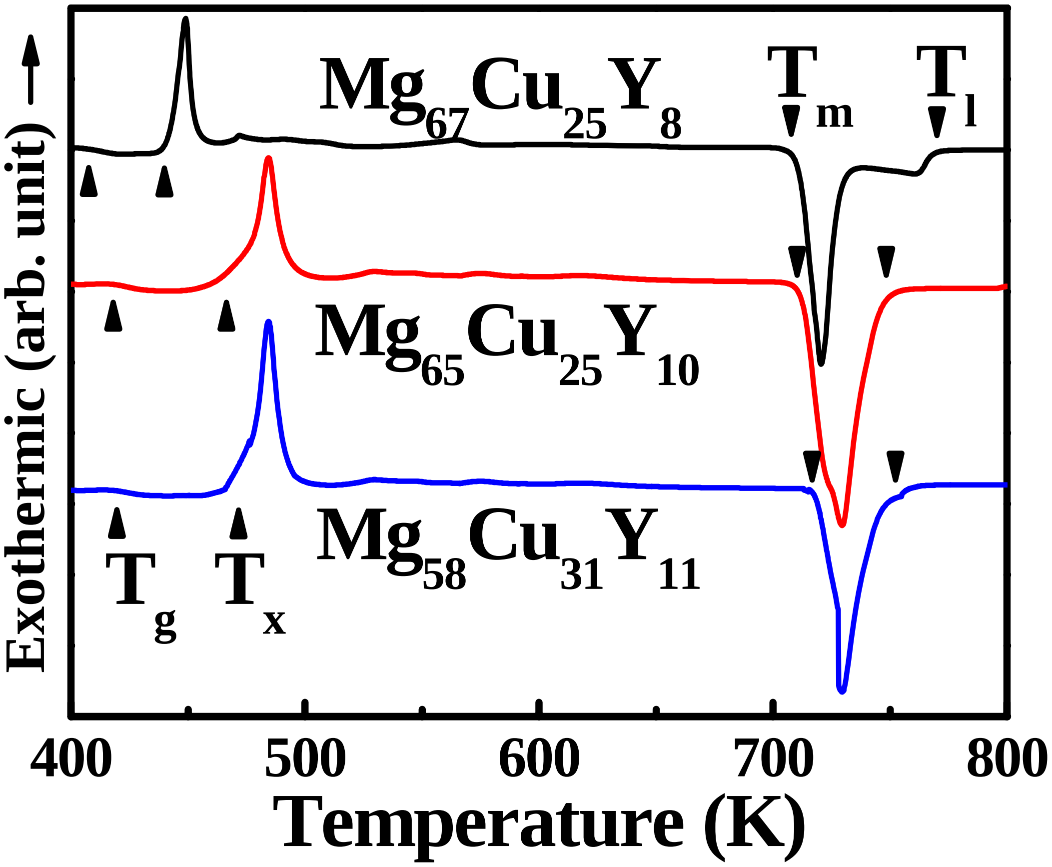

Figure 4.3 DSC scans of the Mg-Cu-Y system metallic glass ribbons

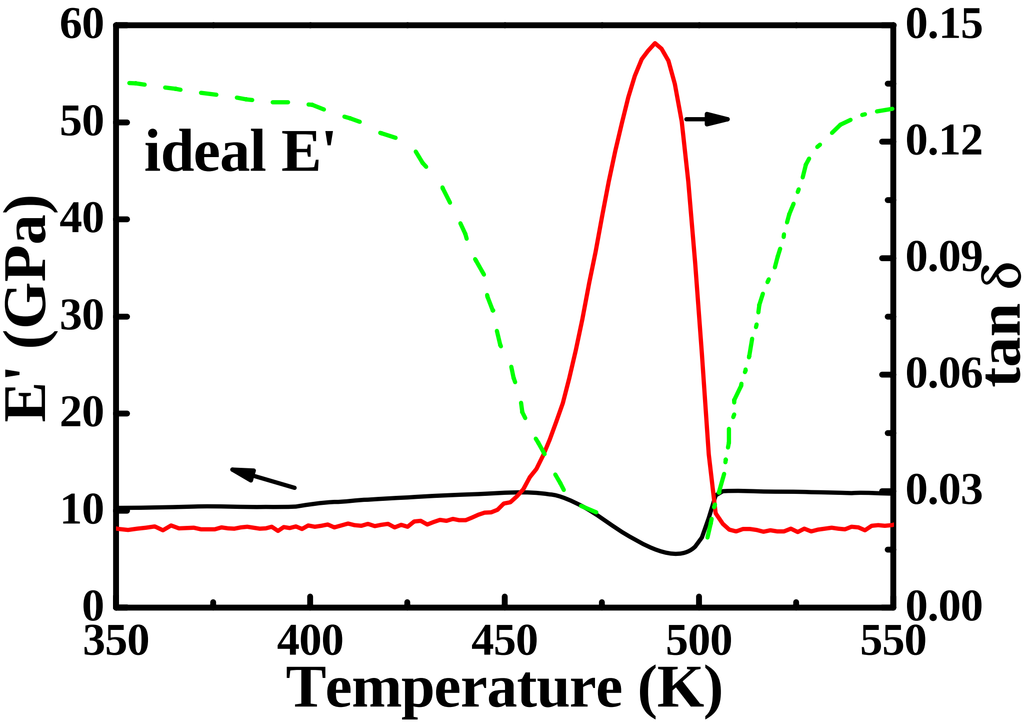

Figure 4.4 Temperature dependence of storage module and tanδ of the $Mg_{58}Cu_{31}Y_{11}$ metallic glass ribbons obtained by DMA operated in the tensile mode at a heating rate of 10 K/min.

Figure 4.5 The photo showing the surface appearance of injection cast $Mg_{58}Cu_{31}Y_{11}$ alloy samples with different diameters, from 3 and 4 mm.

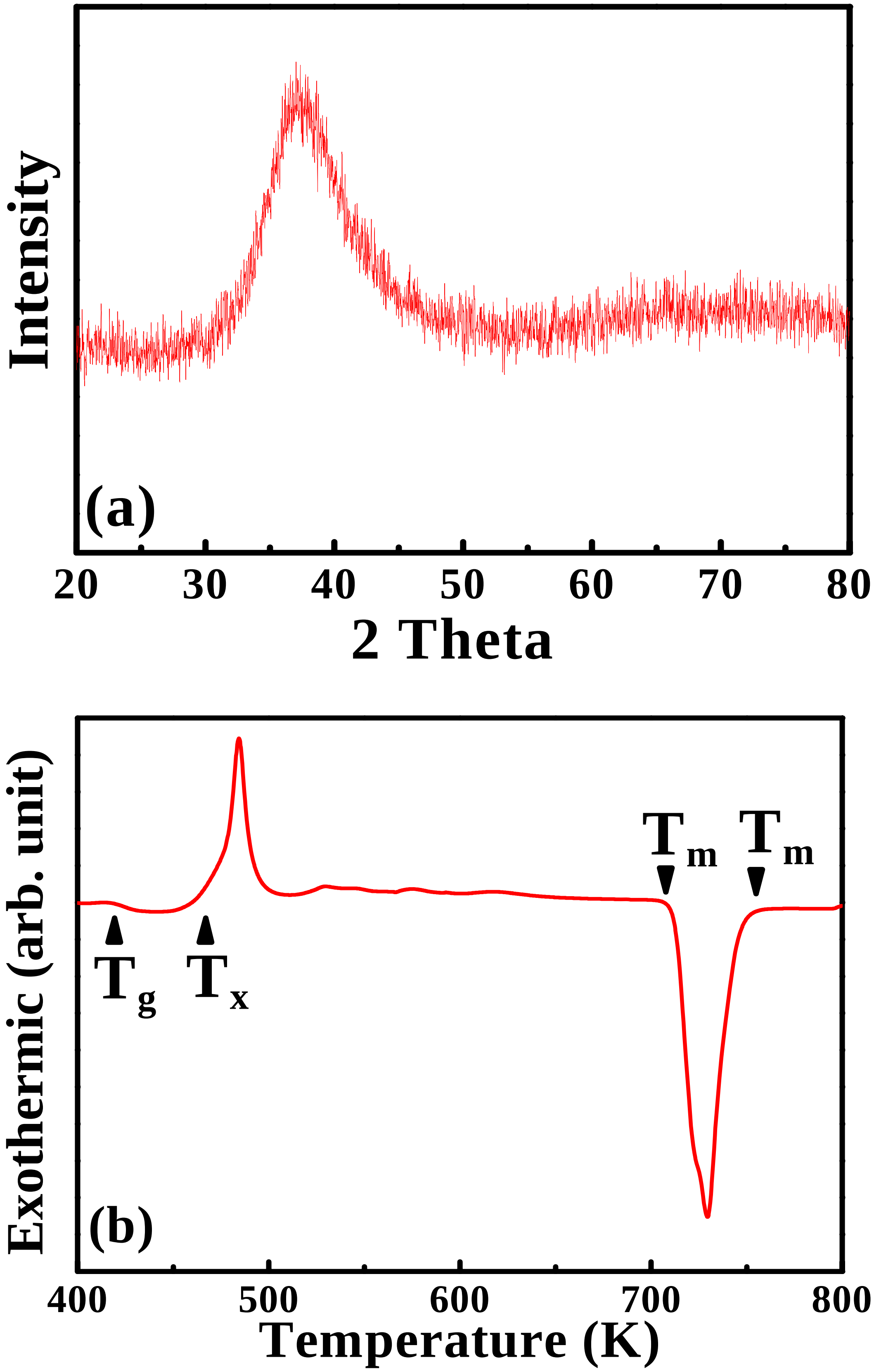

Figure 4.6 (a) X-ray diffraction patterns and (b) DSC thermogram of the $Mg_{58}Cu_{31}Y_{11}$ BMG obtained at a heating rate of 10 K/min.

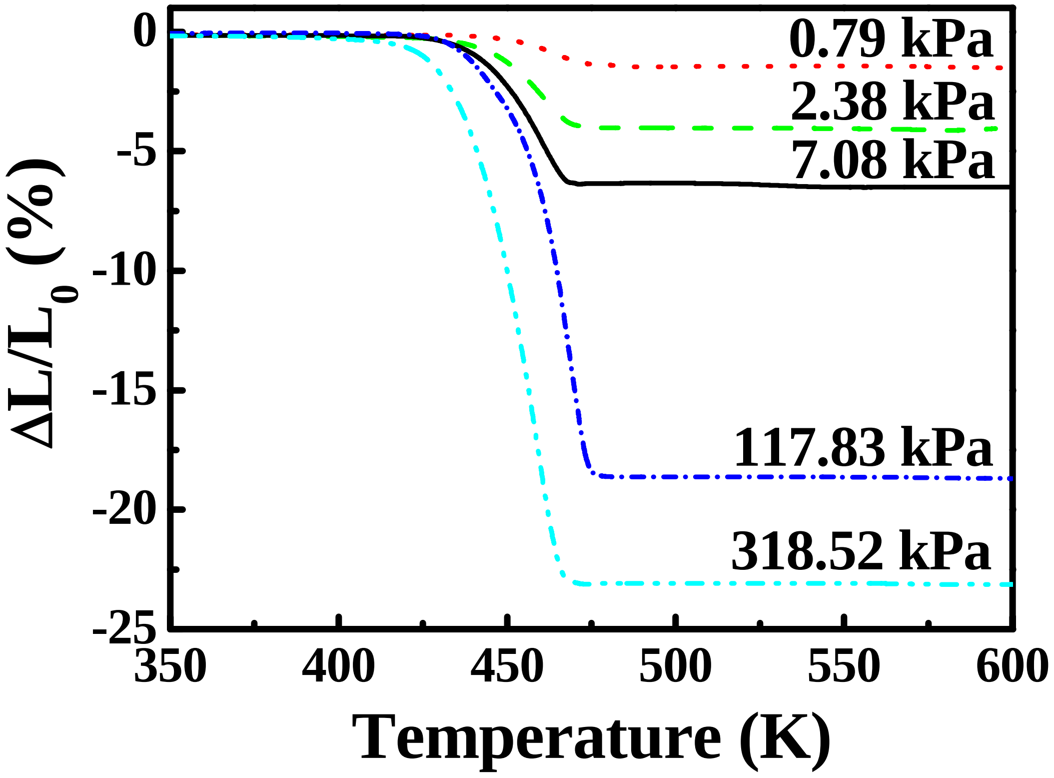

Figure 4.7 Temperature dependence of relative displacement of the as-cast 4 mm bulk amorphous $Mg_{58}Cu_{31}Y_{11}$ alloys obtained by TMA operated in the compression mode at various stress levels and a heating rate of 10 K/min.

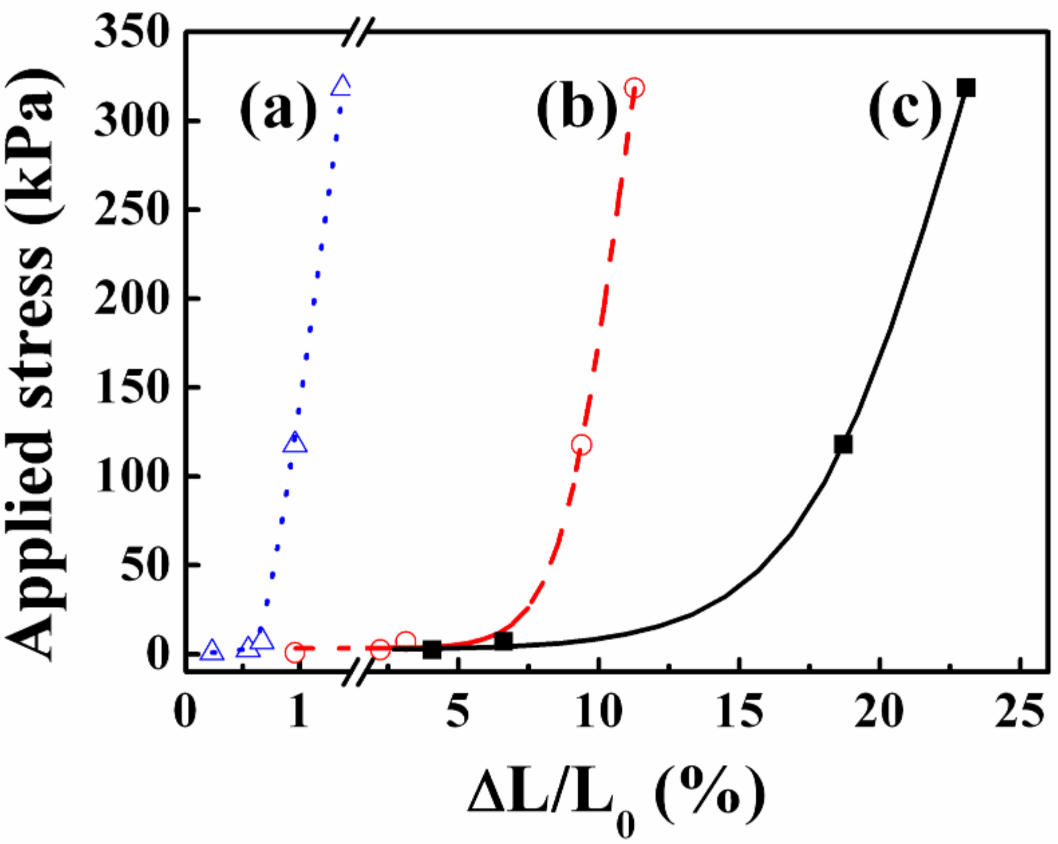

Figure 4.8 Relationship of the as-cast 4 mm bulk amorphous $Mg_{58}Cu_{31}Y_{11}$BMG between applied stress and $\Delta L/L_0$ at (a) T_{onset}, (b) T_{vs}, and (c) T_{finish}.

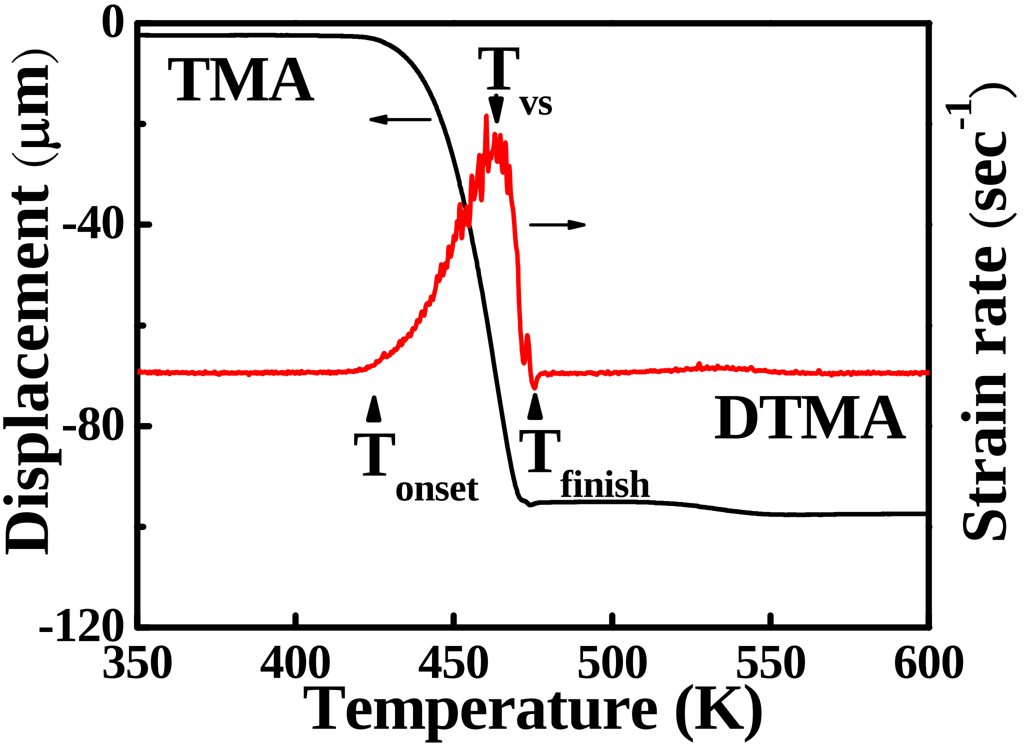

Figure 4.9 Typical TMA and DTMA curves measured at stress level of 7.08 kPa for as-cast bulk amorphous $Mg_{58}Cu_{31}Y_{11}$ alloys.

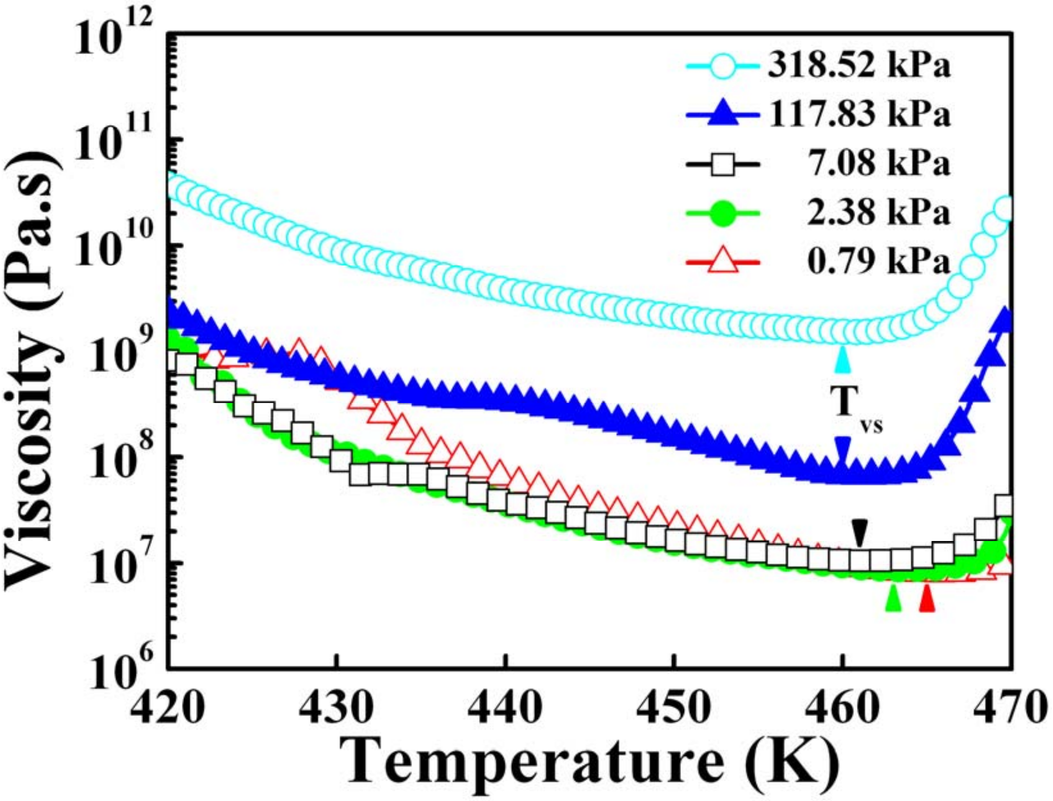

Figure 4.10 Temperature dependence of effective viscosity for the quoted applied stresses at a heating rate of 10 K/min in the $Mg_{58}Cu_{31}Y_{11}$ bulk metallic glass.

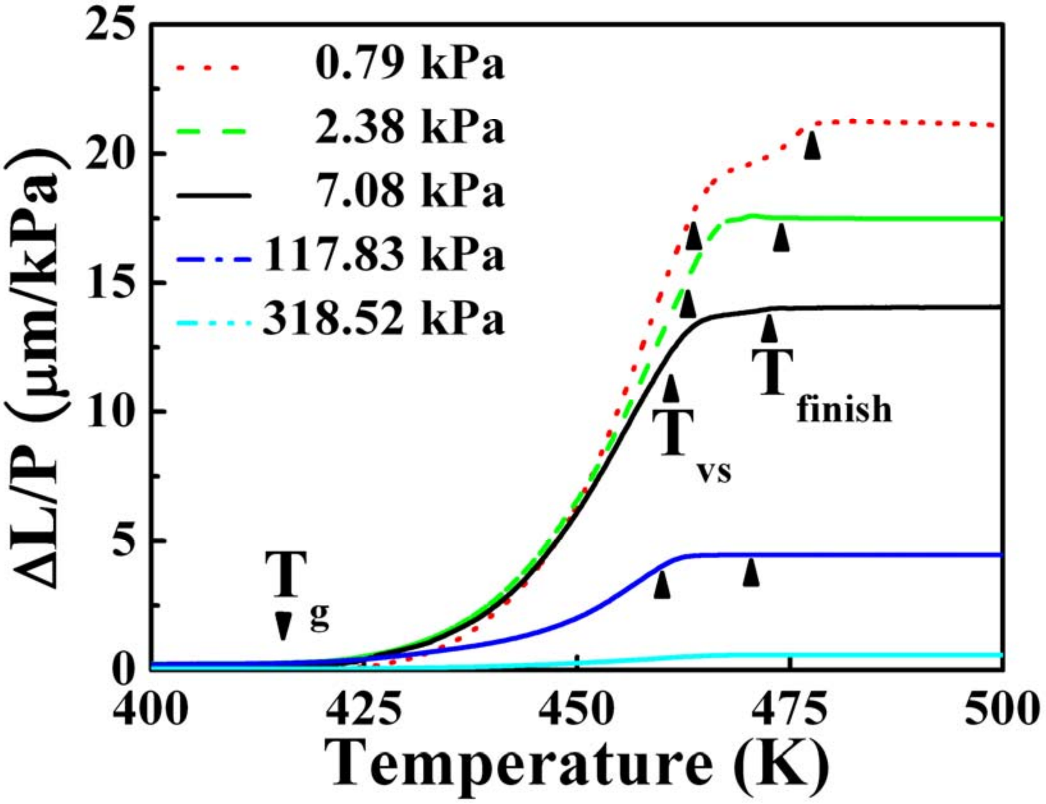

Figure 4.11 The temperature dependence of ΔL/P (displacement/applied stress) at various applied stresses for the as-cast $Mg_{58}Cu_{31}Y_{11}$ samples.

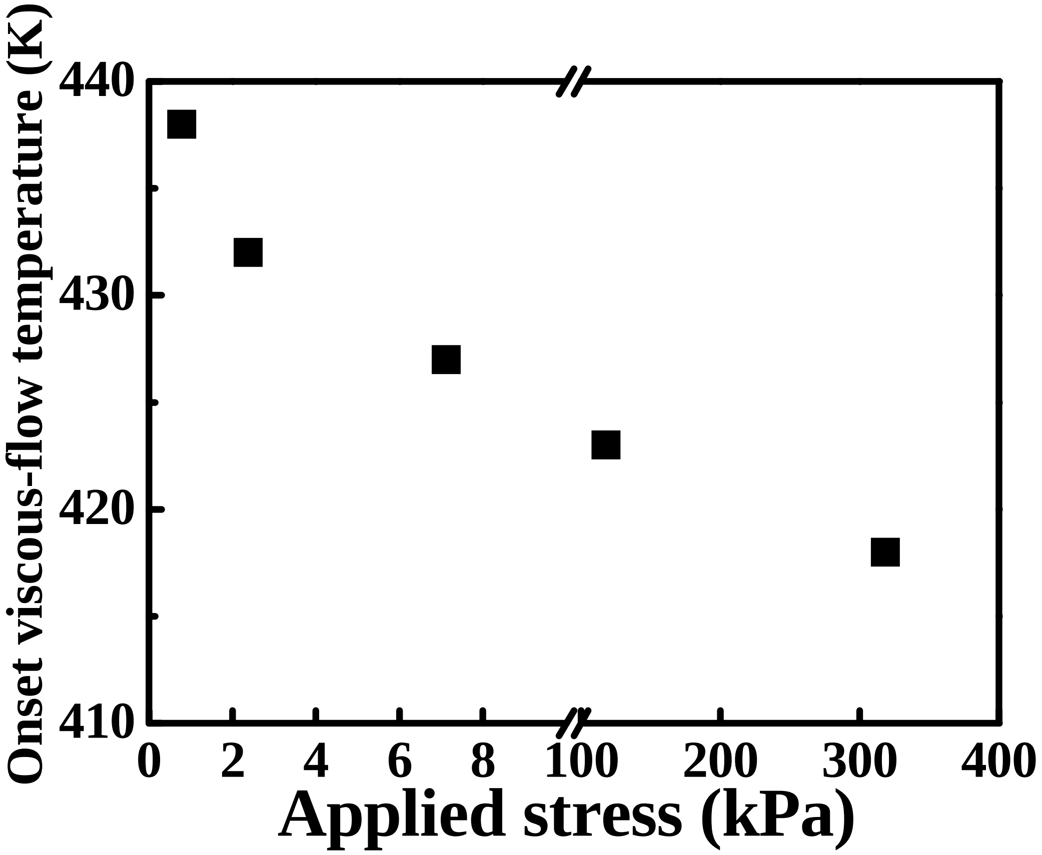

Figure 4.12 Variation of the onset temperature of viscous flow (T_{onset}) with applied stresses.

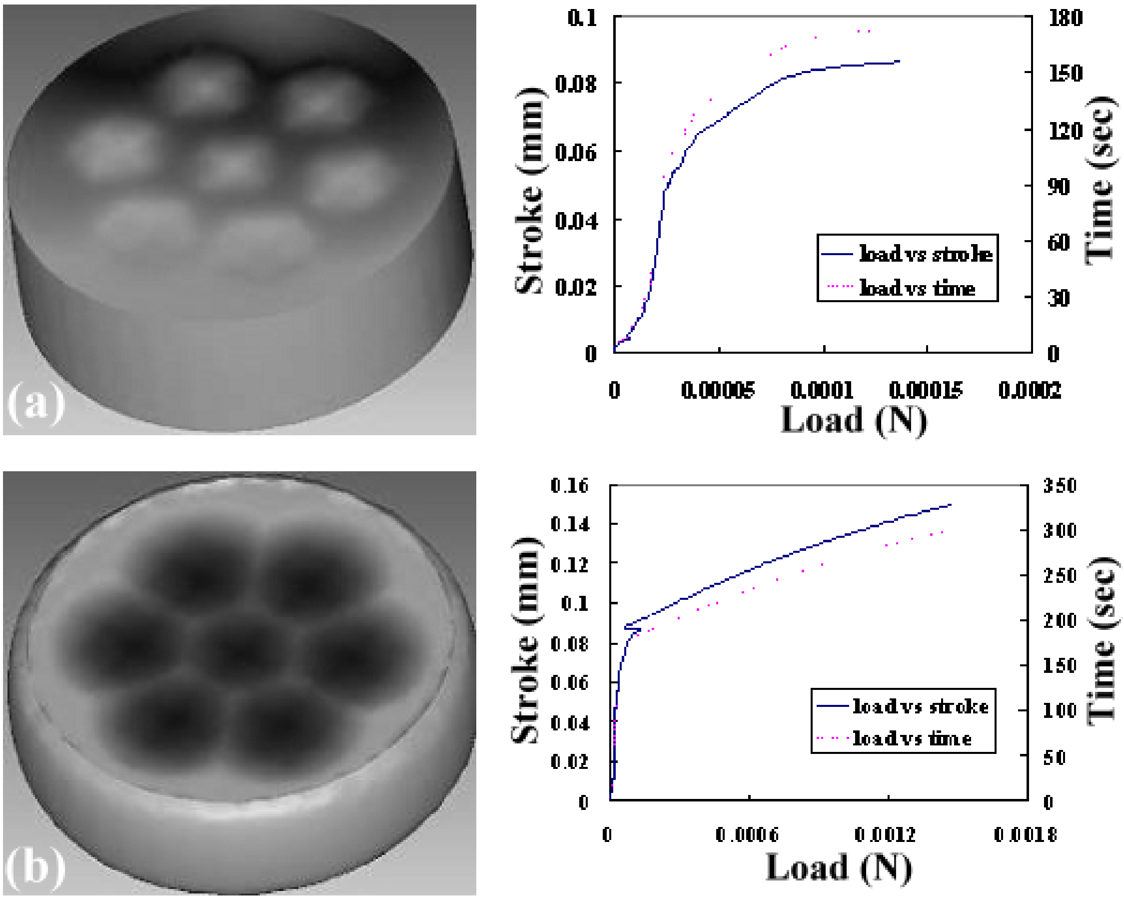

Figure 4.13 The simulated imprinting evolution and the corresponding load prediction: (a) 150°C, 60 s, pressure 31 Pa and (b) 150°C, 240 s, pressure 1176 Pa.

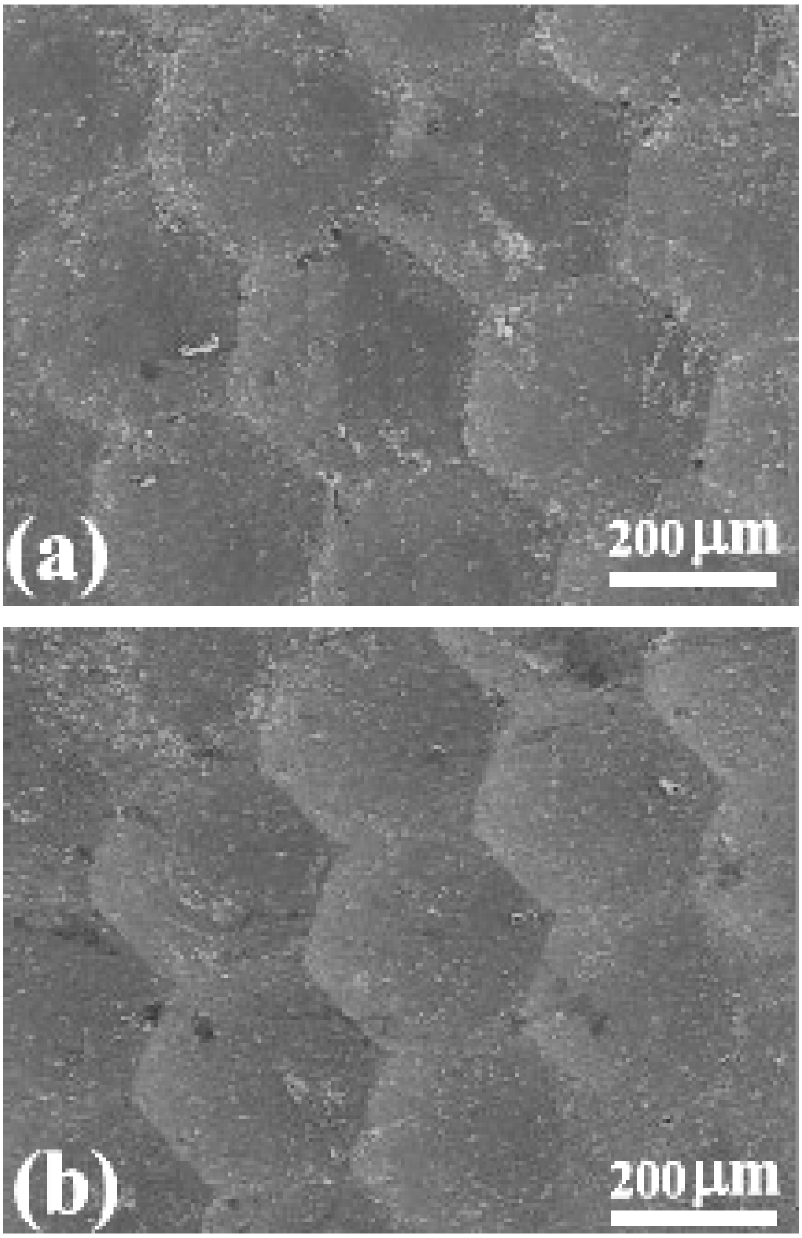

Figure 4.14 The forming extent of the BMG under an applied pressure of (a) 100 kPa and (b) 300 kPa for 4 min.

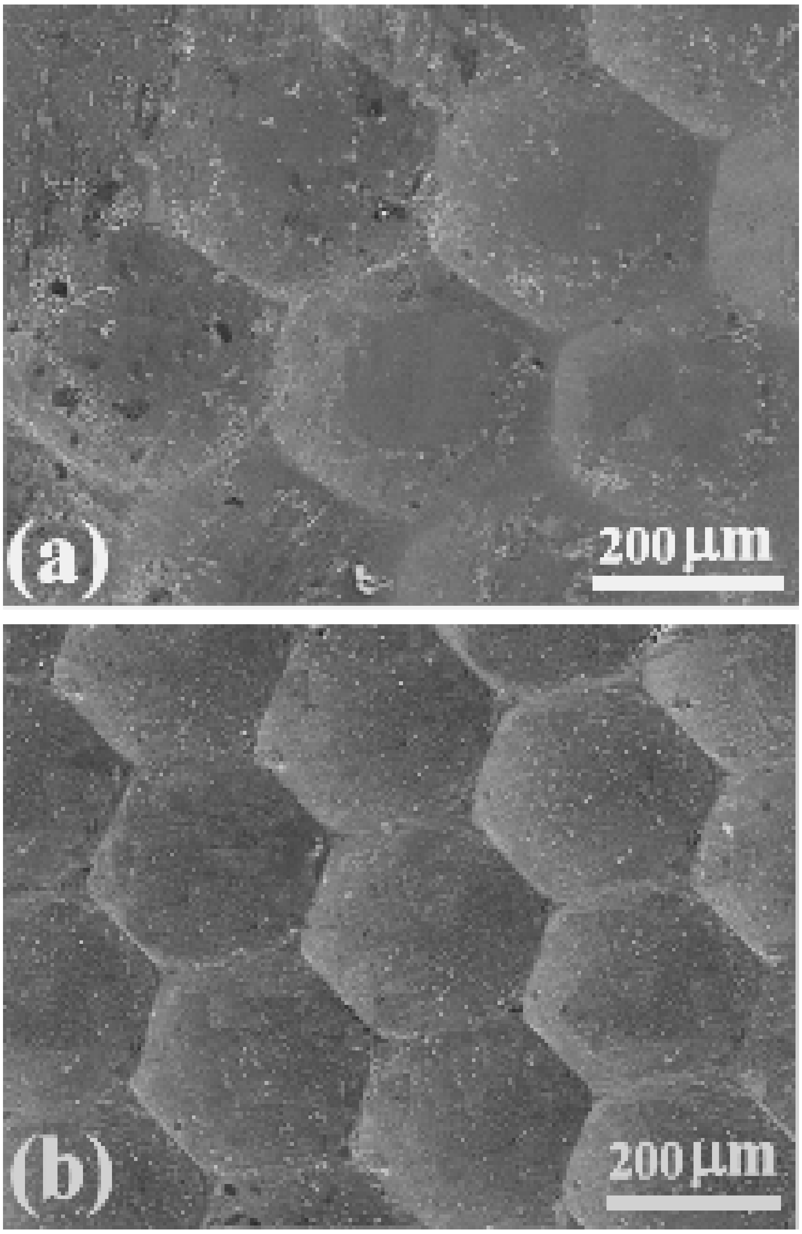

Figure 4.15 The forming extent of the BMG under an applied pressure of 400 kPa for (a) 1 min and (b) 3 min.

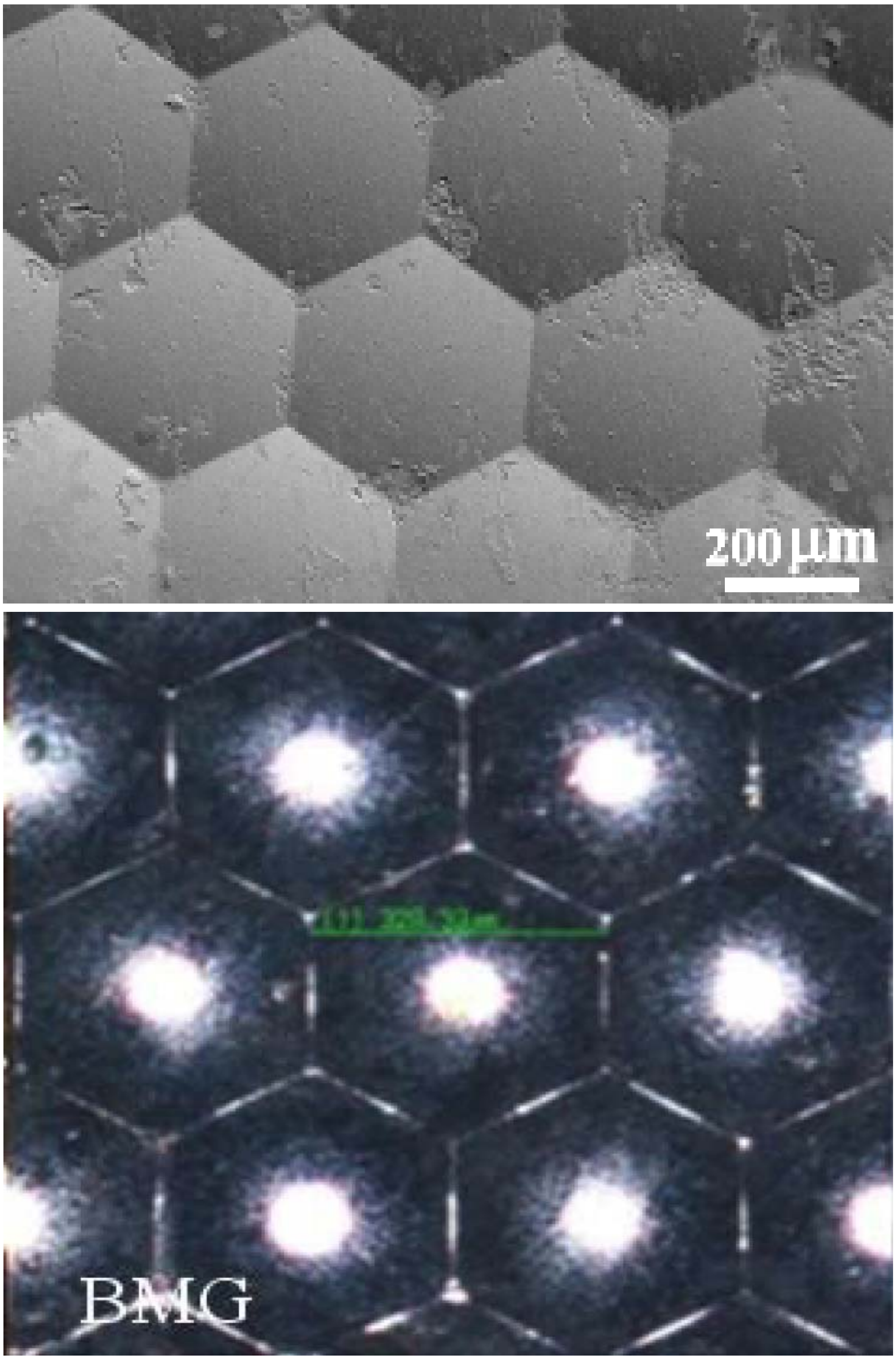

Figure 4.16 SEM micrograph of the formed BMG, operated at 150°C for 4 minutes under a pressure of 400 kPa.

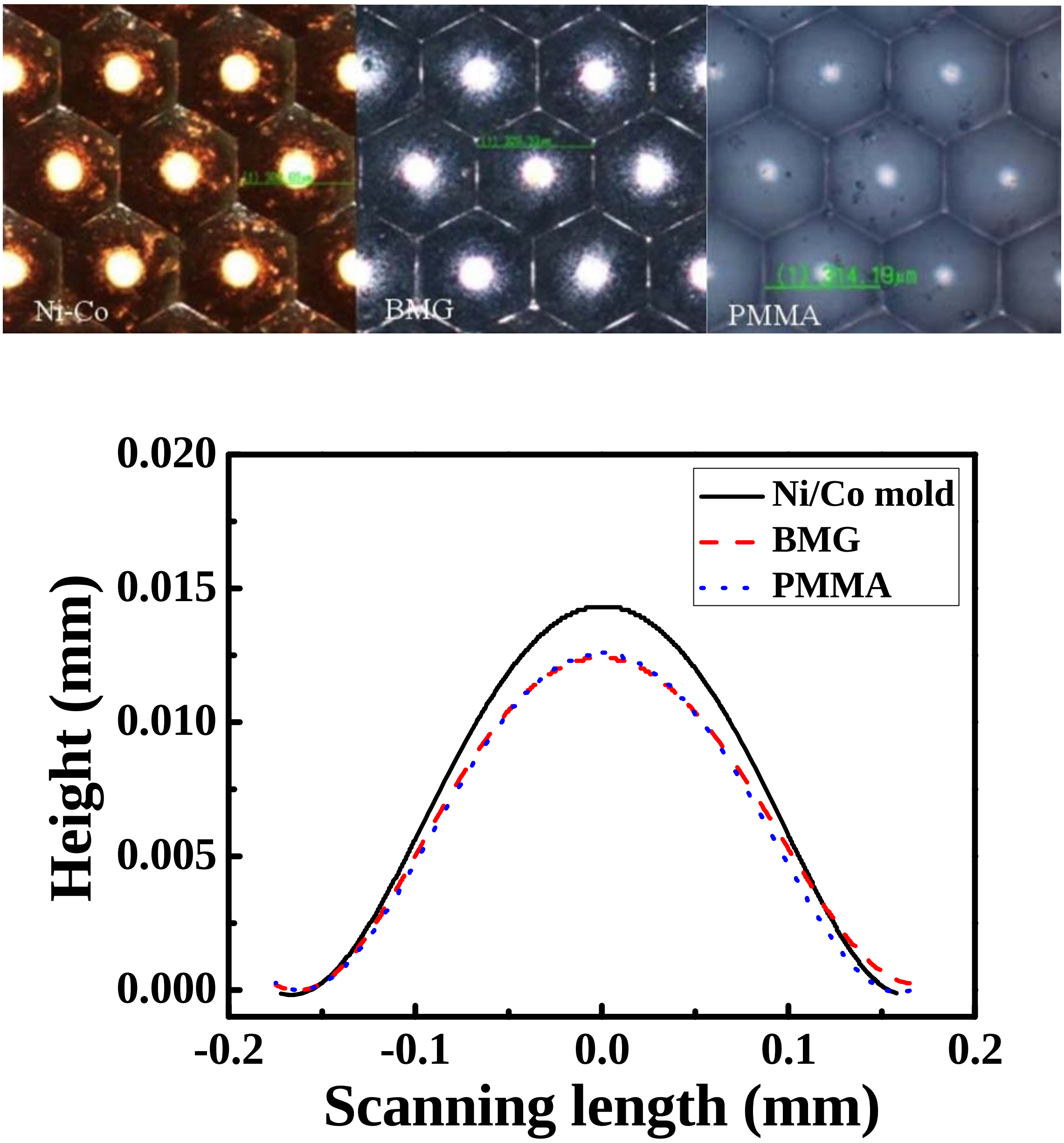

Figure 4.17 Comparison of the surface profiles of the original Ni-Co mold, $Mg_{58}Cu_{31}Y_{11}$ mold, and the PMMA.

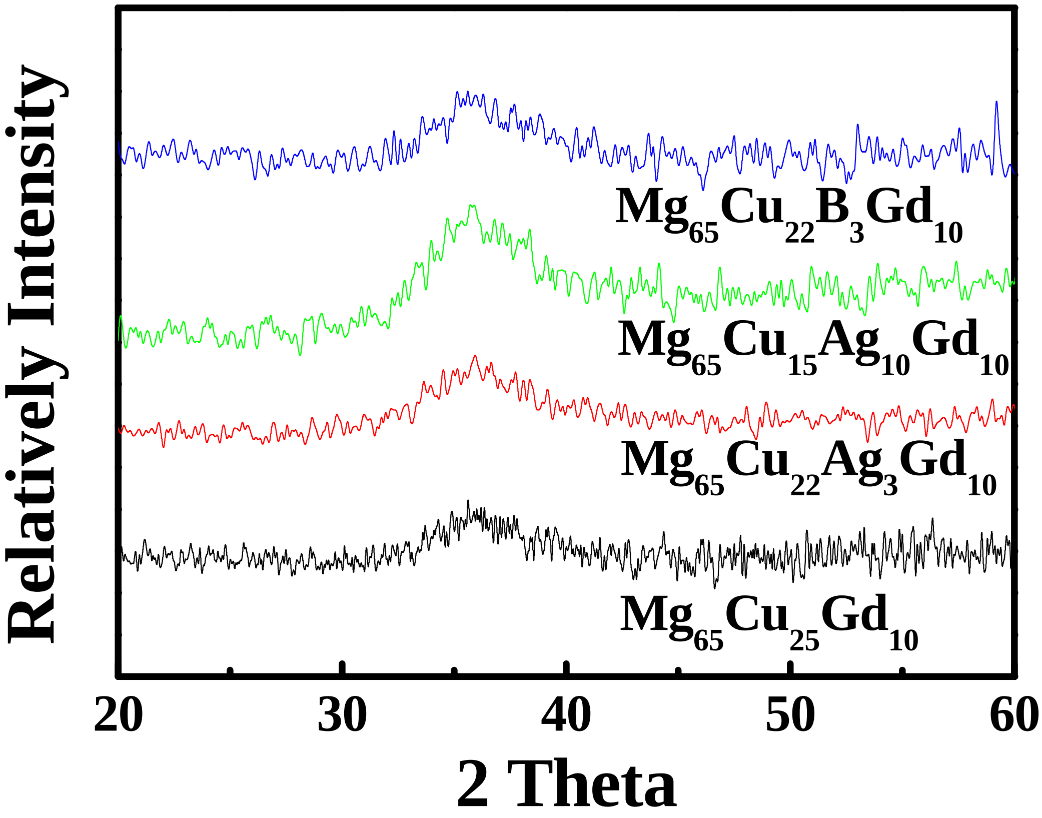

Figure 4.18 X-ray diffraction patterns of the as-quenched $Mg_{65}Cu_{25}Gd_{10}$, $Mg_{65}Cu_{15}Ag_{10}Gd_{10}$, $Mg_{65}Cu_{22}Ag_3Gd_{10}$, and $Mg_{65}Cu_{22}B_3Gd_{10}$ samples.

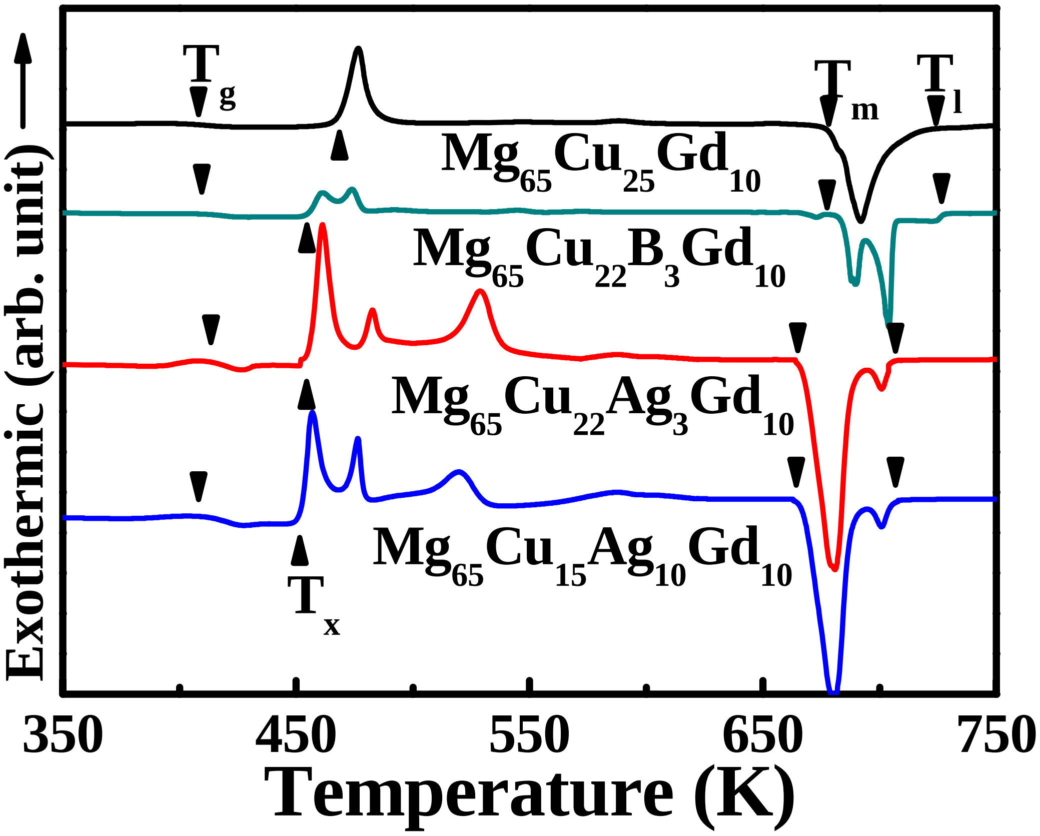

Figure 4.19 DSC thermograms of the $Mg_{65}Cu_{25}Gd_{10}$, $Mg_{65}Cu_{15}Ag_{10}Gd_{10}$, $Mg_{65}Cu_{22}Ag_3Gd_{10}$, and $Mg_{65}Cu_{22}B_3Gd_{10}$ bulk metallic glasses obtained at a heating rate of 10 K/min.

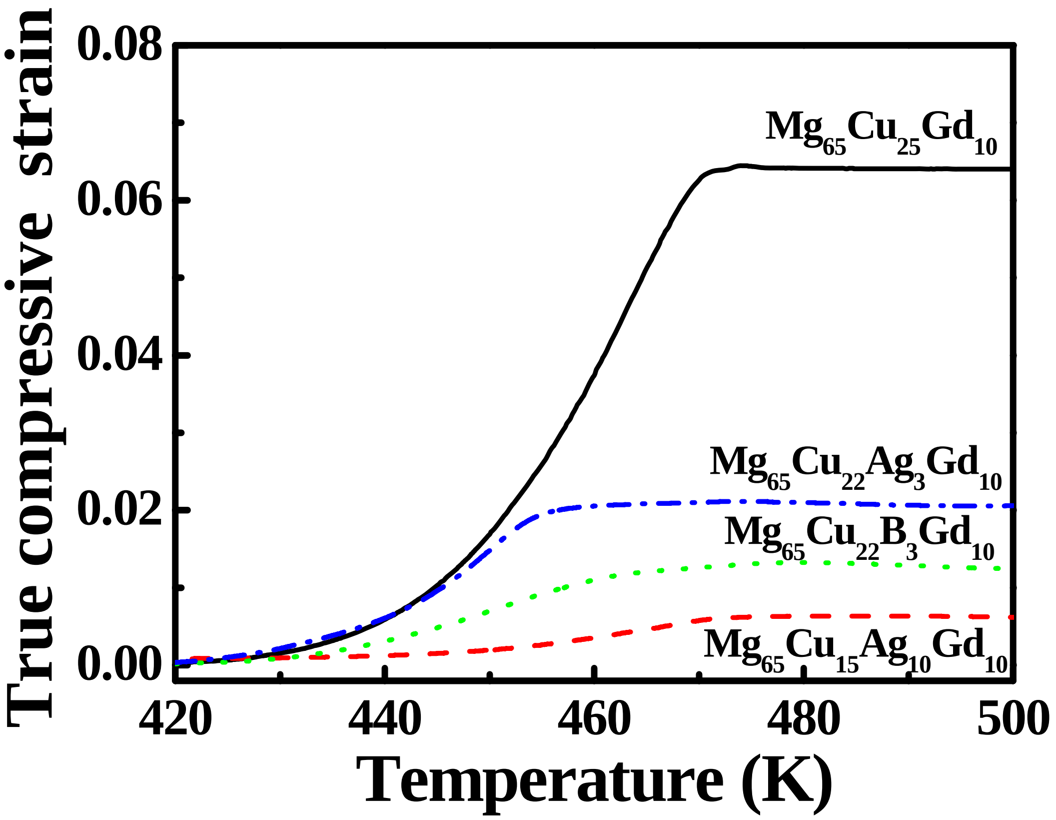

Figure 4.20 The temperature and compressive strain curves of $Mg_{65}Cu_{25}Gd_{10}$, $Mg_{65}Cu_{15}Ag_{10}Gd_{10}$, $Mg_{65}Cu_{22}Ag_3Gd_{10}$, and $Mg_{65}Cu_{22}B_3Gd_{10}$ bulk metallic glasses with a constant applied load of 7.08 kPa under isochronal heating scan at 10 K/min.

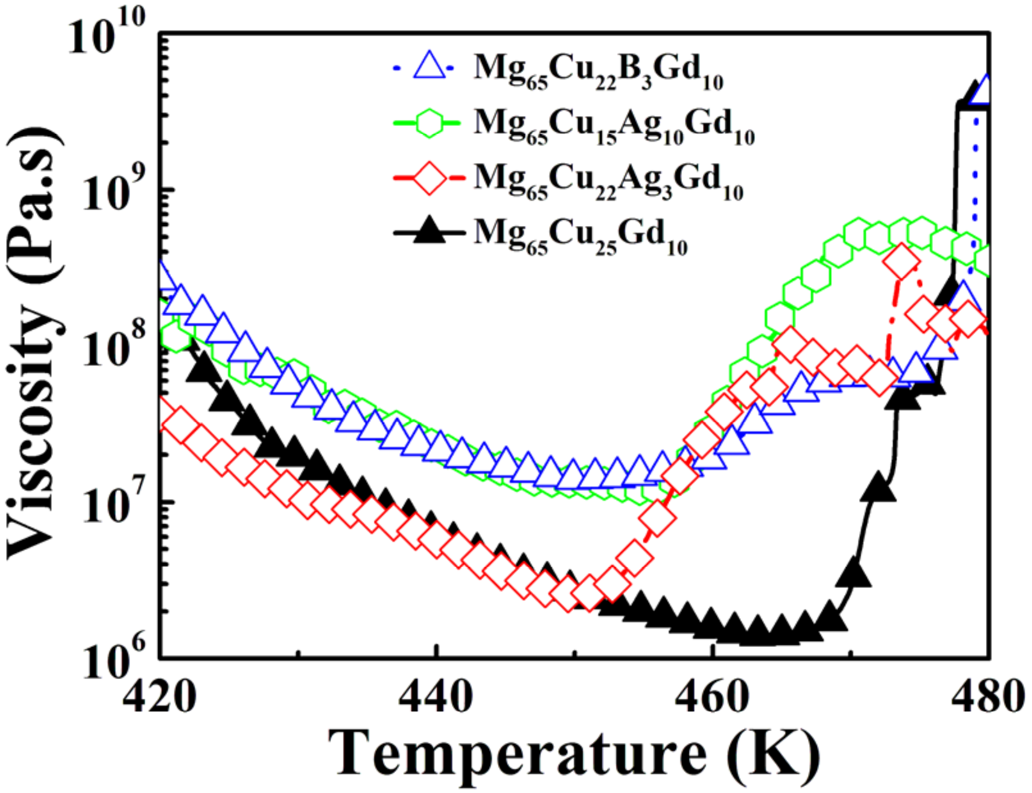

Figure 4.21 Measured viscosities in the supercooled liquid for a constant applied load of 7.08 kPa under isochronal heating scan at 10 K/min.

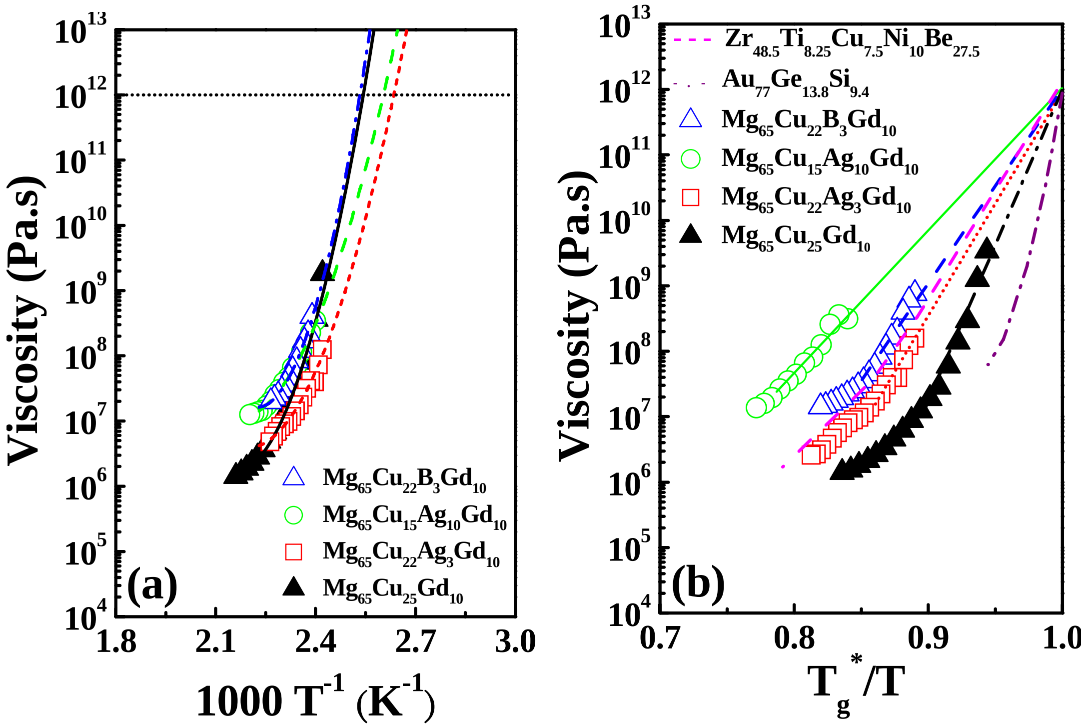

Figure 4.22 (a) Temperature dependence of the viscosity of $Mg_{65}Cu_{25}Gd_{10}$, $Mg_{65}Cu_{15}Ag_{10}Gd_{10}$, $Mg_{65}Cu_{22}Ag_3Gd_{10}$, and $Mg_{65}Cu_{22}Gd_{10}B_3$ bulk metallic glasses, (b) the Angell plots the current four alloys, as compared with $Zr_{46.5}Ti_{8.25}Cu_{7.5}Ni_{10}Be_{27.5}$ and $Au_{77}Ge_{13.8}Si_{9.4}$ alloys. All experimental results are fitted by the VFT equation.

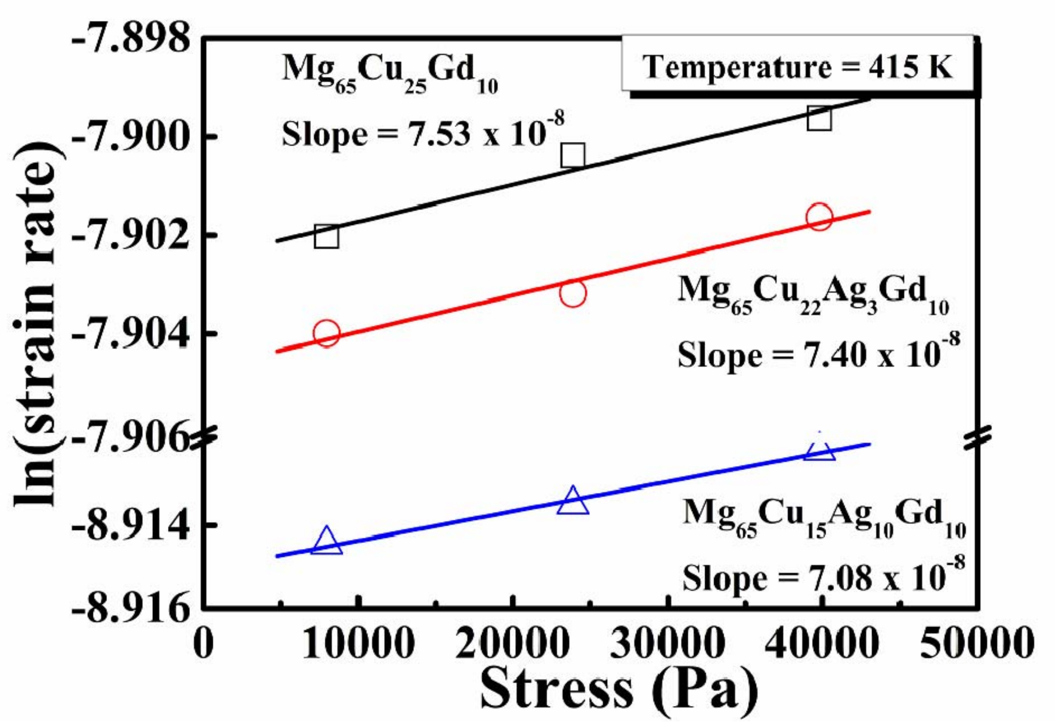

Figure 4.23 Determination of the STZ sizes of the Mg-Cu-(Ag)-Gd alloys based on the TMA data after the correction for coefficient of thermal expansion.

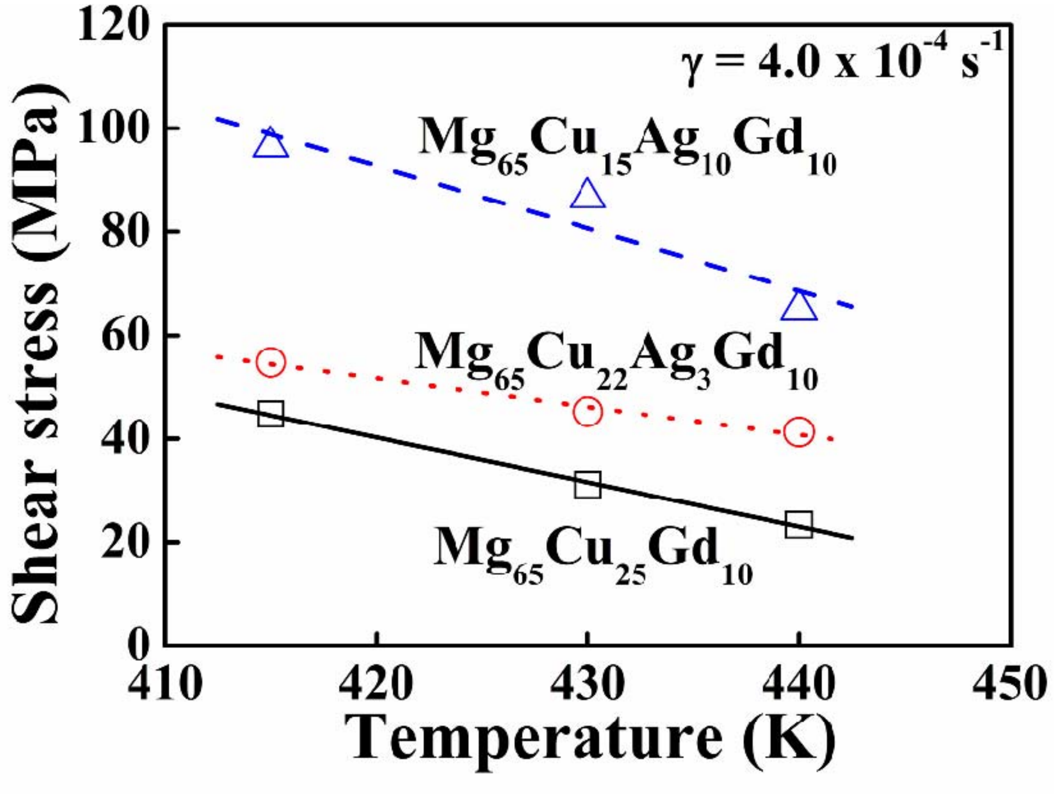

Figure 4.24 Extraction of the activation energy of the Mg-Cu-(Ag)-Gd alloys during shear deformation within the supercooled temperature region.

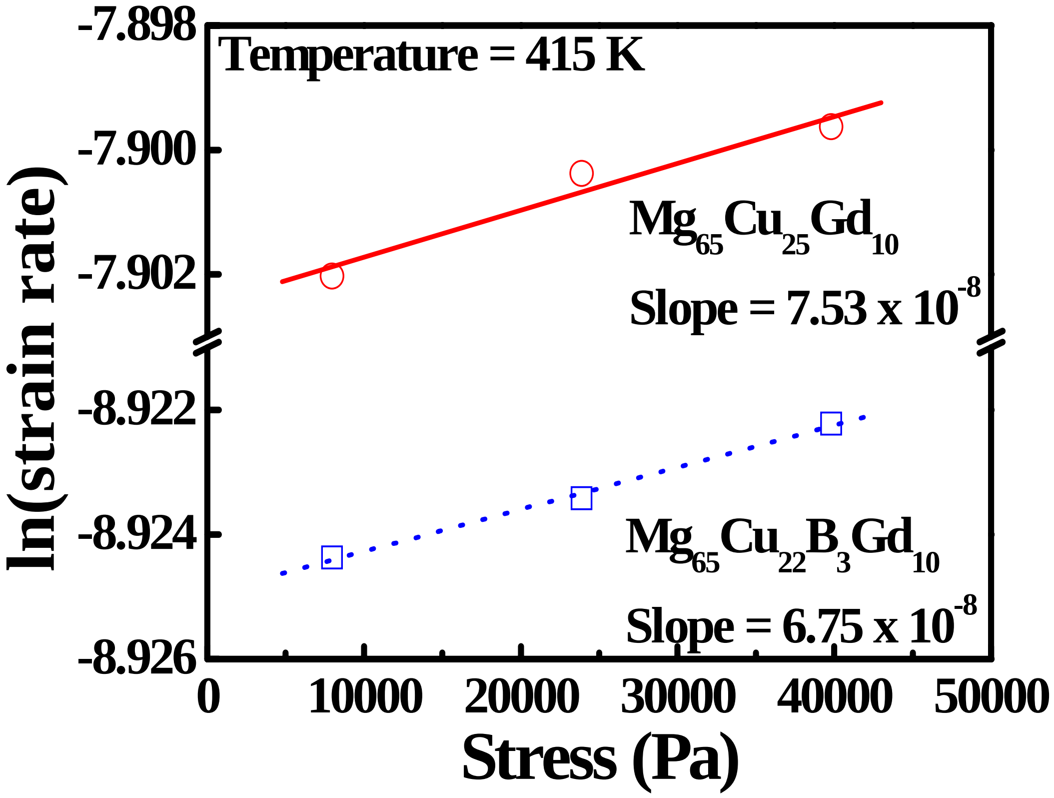

Figure 4.25 Determination of STZ sizes of the $Mg_{65}Cu_{25}Gd_{10}$ and $Mg_{65}Cu_{22}B_3Gd_{10}$ alloys based on the TMA data after the correction for coefficient of thermal expansion.

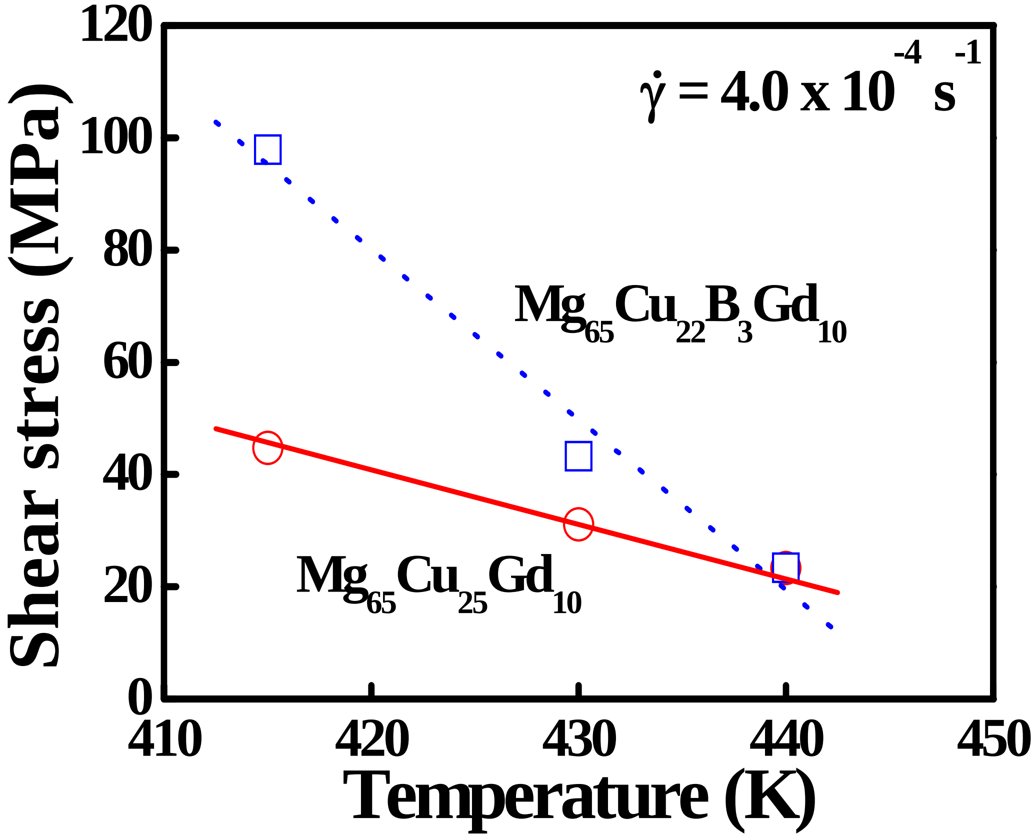

Figure 4.26 Extraction of the activation energy of $Mg_{65}Cu_{25}Gd_{10}$ and $Mg_{65}Cu_{22}B_3Gd_{10}$ during shear deformation within the supercooled temperature region.